Dissertation:

Lattice-Boltzmann Modeling of Bacterial Chemotaxis in the Subsurface

by

Zhifeng Yan

A dissertation submitted to The Johns Hopkins University in conformity with the requirements for the degree of Doctor of Philosophy.

Baltimore, Maryland

October, 2014

Abstract

The Lattice Boltzmann method (LBM) has been widely used because it is well-suited to model flow and transport in the complex geometries that are typical for subsurface porous media. Bacterial chemotaxis enables motile bacteria to move preferably toward chemoattractants that may be contaminants in the subsurface. This microbial phenomenon provides a valuable mechanism to enhance *in situ* bioremediation. Therefore, we developed Lattice Boltzmann (LB) models to study bacterial chemotaxis in the subsurface.

A multiple-relaxation-time (MRT) LB model was developed to study the formation and migration of traveling bacterial waves caused by chemotaxis (chemotactic waves) in the absence of bacterial growth and decay. This model was validated by comparing simulations with experiments in which the chemotactic bacteria entered a tube filled with substrate due to chemotaxis. Simulations were performed to evaluate the effects of substrate diffusion, initial bacterial concentration, and hydrodynamic dispersion on the formation, shape, and propagation of such chemotactic waves. Wave formation requires a sufficiently high initial number of bacteria and a small substrate diffusion coefficient. Uniform flow does not affect the waves while shear flow does. Bacterial waves move both upstream and downstream when the flow velocity is small. However, the waves disappear

once the velocity becomes large due to hydrodynamic dispersion. Generally waves can only be observed if the dimensionless ratio between a particularly defined coefficient, chemotactic sensitivity coefficient, and the effective diffusion coefficient of the bacteria exceeds a critical value, that is, when the biased movement due to chemotaxis overcomes the diffusion-like movement due to the random motility and hydrodynamic dispersion.

Another two-relaxation-time (TRT) LB model was also introduced to simulate bacterial chemotaxis and other reactive transport. The TRT LB model can eliminate numerical diffusion by including a velocity correction term. One-dimensional solute transport with initial Gaussian and top hat distributions were investigated to evaluate the accuracy and stability of the TRT models with and without the velocity correction. The TRT model with the correction demonstrated better numerical accuracy and stability than that without the correction. When the velocity is small, the numerical diffusion can be neglected, and the TRT model without the correction attained very similar simulation results as the TRT model with the correction. However, it is necessary for the TRT model to include the velocity correction when the velocity is large.

Since bacterial survival is a significant factor for contaminant remediation at contaminated sites, we studied the coupled effects of chemotaxis and growth on bacterial migration and contaminant remediation. The impacts of initial electron acceptor concentration on different bacteria and substrate systems were examined. The simulations showed that bacteria could form a growth/decay/motility wave due to a dynamic equilibrium between bacterial growth, decay and random motility, even though the bacteria perform no chemotaxis.

We derived an analytical solution to estimate this growth/decay/motility wave speed. The initial electron acceptor concentration was shown to significantly affect the bacterial movement and substrate removal. The impact of chemotaxis on bacterial migration is determined by comparison of the chemotactic wave speed with the growth/decay/motility wave speed. When chemotaxis is too weak to allow for the formation of a chemotactic wave or its wave speed is less than half of the growth/decay/motility wave speed, it hardly enhances the bacterial propagation. However, chemotaxis significantly improves bacterial propagation once its wave speed exceeds the growth/decay/motility wave speed. The bacterial survival plays a crucial role in determining the efficiency of contaminant removal. If there is no growth, the traveling wave will move with a decreasing speed and finally terminates.

Although chemotaxis has been widely observed to be able to improve contaminant degradation in laboratories, it is rarely reported to enhance bioremediation at field sites. We discuss this discrepancy based on our simulation findings and suggest operable measures to take advantage of chemotaxis in *in situ* bioremediation.

Acknowledgments

I would like to express my deepest gratitude to my academic advisor, Professor Markus Hilpert, for his incredible patience, kindness, encouragement, financial and technical support. He always trusts me and gives me freedom to explore my own research interests. Meanwhile, he always provides me valuable advice and helps me to move forward whenever I face an academic challenge. Without him, I would not have been able to finish this work.

I would like to express my special gratitude to Professor Alan Stone. He is not only a respected scientist but also a trusted friend. He has taught me so much about doing research and enjoying life. Our afternoon tea time on weekends has become one of my best memories at Johns Hopkins University. I am also very grateful to Professor Edward Bouwer for providing generous support in my research all the time. Specifically, he always encourages me to improve my English, and keeps saying "Zhifeng, the more you speak, the better your English is".

I would like to thank Professors William Ball and Kailoon Chen from the Department of Geography and Environmental Engineering (DoGEE) for serving on my Department Qualifying Exam committee. I also thank Professors Andrea Prosperetti, Charles Meneveau from the Department of Mechanical Engineering, and Peter Devreotes from the

Department of Cell Biology for serving on my Graduate Board Examination committee. Their queries and comments have helped me to accomplish better research. I benefited especially from discussion with Prof. William Ball, who always raised interesting questions and gave insightful feedback during my presentations.

I would like to acknowledge former Hilpert group members Drs. Roland Glantz, Shao-Yiu Hsu, and Yaqi You. They have been so generous to provide all kinds of assistance in my research and life. Also I want to thank all members in Ball-Bouwer group and other colleagues in DoGEE. DoGEE is an amazing family and I feel so lucky to pursue my PhD here.

Finally I would like to thank my family for their unconditional support and love. I would also like to extend my appreciation to my friends in Baltimore. They make my life much more enjoyable and memorable.

Advisor: Dr. Markus Hilpert

Contents

List of Tables

List of Figures

Chapter 1. Introduction

1.1 Motivation

Groundwater pollution is a critical concern to public health. In 2004, the US EPA reported that approximately 294,000 contaminated field sites were in need of remediation [2]. A major challenge is to clean up the large number of aquifers contaminated by organic pollutants. Conventional cleanup technologies such as pump-and-treat are time-consuming and expensive [52]. Bioremediation, the reduction of contaminant mass through microbial activity without pumping the contaminated water or excavating contaminated soil, has increased in popularity as an alternative treatment due to its effectiveness and cost efficiency [34]. Among all remediation projects, about one in four makes use of *in situ* bioremediation methods (Figure 1.1a).

The rate and extent of bioremediation are difficult to predict because many biotic factors (inoculum density and size, preinduction, cell immobilization, adaptation of degradative microorganisms towards environmental stresses) and abiotic factors (pH, temperature, concentration of target pollutants and cross-contamination of other non-targeted pollutants, moisture content, nutrient availability, volatilization, sorption and desorption) are usually not quantifiable [65]. Many studies have shown that microorganism survival is one of the most important biotic factors determining the applicability and sustainability of *in*

situ bioremediation [41, 42, 33]. Among all the abiotic factors, bioavailability has been identified as a major limitation to bioremediation efficiency because microorganisms tend to be present in zones with high hydraulic conductivity and leave contaminant sources in regions with fairly low conductivity not biodegraded [5].

Random motility and chemotaxis are two common cell motion mechanisms [53]. The former allows bacteria to move independent of chemicals, while the latter enables motile bacteria to sense chemical gradients in their surrounding environment and move toward regions with high chemical concentration [6] (Figure 1.1b). Therefore, studying the effects of bacterial growth and decay, random motility, and chemotaxis on bacterial movement as well as on contaminant bioremediation has practical value to designing groundwater remediation strategies.

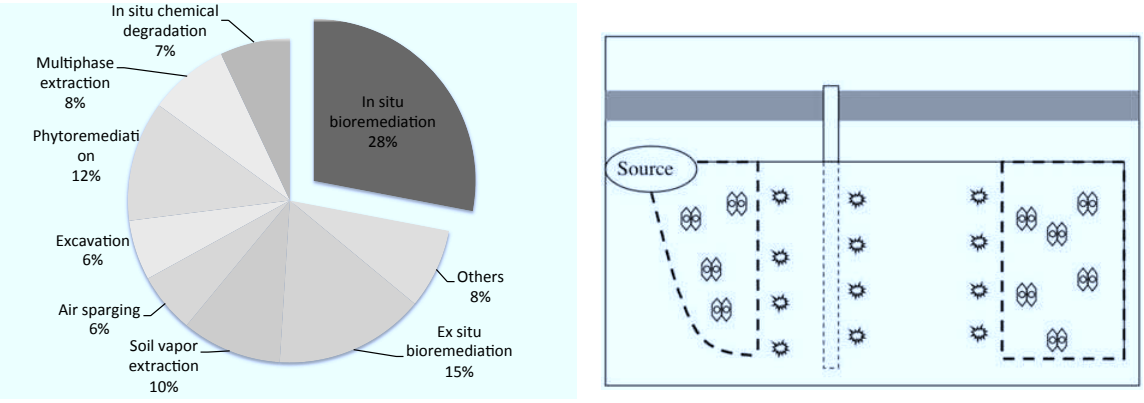

(a) (b)

Figure 1.1: (a) A pie chart representing the percentage distribution of common remediation technologies used in decontamination of polluted soil and groundwater [65]. (b) Usage of chemotactic bacteria in bioremediation of groundwater, where bacteria move from injection well to pollutant source [50].

1.2 Bacterial chemotaxis

Bacterial chemotaxis is a microbial phenomenon in which bacteria move preferably toward or away from regions with a high concentration of chemicals (called chemoattractants or chemorepellents) [1]. This dissertation focuses on bacterial chemotaxis toward chemoattractants, a process that can potentially enhance contaminant remediation. As an evolutionary benefit, many bacteria can move in surroundings by swinging or rotating their flagella. Brown and Berg [11] experimentally observed the trajectory of *E. coli* and established a tumble-and-run model to illustrate the mechanism of bacterial movement. When bacteria do not exhibit chemotaxis, they move in a direction by rotating their flagella in counter-clockwise direction (run) and change their swimming direction by rotating their flagella in clockwise direction (tumble). This alternating series of runs and tumbles result in a 3D random walk that is analogous to molecular diffusion. However, when the bacteria exhibit chemotaxis, the time for bacteria running toward regions with a higher concentration of chemoattractants is prolonged, while the time toward regions with a lower concentration is shortened. As a result, the bacteria move preferably toward regions with a higher concentration of chemoattractants [8].

Chemotaxis has been reported to improve contaminant remediation by increasing pollutant bioavailability in aqueous and subsurface environments [26, 73, 27, 54]. A large number of harmful chemicals (e.g., toluene, benzene, naphthalene, polycyclic aromatic hydrocarbons, and trichloroethylene) have been found to be chemoattractants for various bacterial strains [55, 66, 64, 61, 78]. Pandey and Jain [64] reviewed the chemotactic

response of bacteria toward environmental pollutants.

The chemotaxis of *Pseudomonas* (*P.*) *putida* G7 toward naphthalene has been studied extensively. For example, Marx and Aitken [54] examined the influence of bacterial chemotaxis on naphthalene degradation in a heterogeneous aqueous system. They found that a wild-type chemotactic *P. putida* G7 took only 6 hours to reduce 90% of the naphthalene while the nonchemotactic mutant strain took 30 hours. Law and Aitken [48] also investigated the effects of chemotaxis of *P. putida* G7 on naphthalene desorption and degradation in a system where the naphthalene was dissolved in a Non-Aqueous Phase Liquid. The results showed that chemotaxis could substantially increase the rate of naphthalene desorption and degradation. The extent to which chemotaxis enhanced naphthalene transfer and degradation depended on the initial bacteria and naphthalene concentrations.

Other bacterial strains and pollutants have also been studied. For example, Samanta et al. [73] examined the chemotactic response of a Ralstonia sp. SJ98 toward different nitroaromatic compounds (NACs). They found that chemotaxis was useful in reducing these NACs. Parales et al. [66] tested the ability of five different motile bacterial strains that used five different ways to degrade toluene. The results showed that the introduction of chemotactic bacteria into selected contaminated sites might accelerate bioremediation processes.

Although capillary tubes and swarm plates have been widely used in studying bacterial chemotaxis [1, 55, 67, 72], microfluidic devices are becoming increasingly popular with the

development of their manufacturing and controlling techniques [76, 3, 40]. Microfluidic devices can generate various concentration gradients of chemicals by injecting, mixing and splitting fluid flows that contain the chemicals. Ahmed et al. [3] reviewed the application of microfluidics to study chemotaxis. Various geometries were fabricated to attain suitable gradients of chemoattractants. The size and transparency of microchannels make them convenient to measure the concentration gradients of chemoattractants and the bacterial movement.

Kim and Kim [40] fabricated a long-range concentration gradient generator for bacterial chemotaxis in a microfluidic device. This device could simultaneously produce concentration gradients for several chemicals. By using this device, the authors examined the threshold chemical concentration for chemotactic activation and the maximum chemical concentration for chemotactic response, between which two concentrations the bacteria performed chemotactic behavior. Wang and Long [78] experimentally studied the chemotaxis of *P. putida* F1 toward organic-phase toluene and *E. coli* toward organic-phase phenol in a pore-scale microfluidic chamber for different flow velocities. With small velocity, more bacteria gathered near the organic/aqueous interface. The accumulation of chemotactic bacteria near the chemoattractant source decreased as the flow velocity increased. These experiments demonstrate that microfluidic devices are a promising tool for studying chemotaxis.

Although chemotaxis has been demonstrated to accelerate contaminant removal in laboratory experiments, to my knowledge, no obvious evidence has been reported in con-

taminated field sites showing that chemotaxis improves bioremediation. The effects of chemotaxis are difficult to elucidate in *in situ* bioremediation due to the environmental complexity of field sites [19]. Instead, bacterial chemotaxis in porous media were examined in laboratories to evaluate the effects of chemotaxis in contaminated sites. For example, Roush et al. [72] studied the influence of porous media heterogeneity on chemotaxis of *P. stutzeri* strain KC toward acetate and nitrate. They found that chemotactic response was enhanced in the porous media compared to in the aqueous phase. Therefore, the chemotaxis might produce a larger effect on *in situ* bioremediation than that anticipated from laboratory measurements in bulk solution.

Most laboratory studies involving chemotaxis were conducted over a short time period, from minutes to hours, such that bacterial growth and decay could be neglected and the analysis could be focused on chemotaxis. However, the practical field clean-up usually takes several months or even years [68]. Bacterial survival plays a crucial role in determining the success of biodegradation [41, 42, 33]. Therefore, it is necessary to study the coupled effects of chemotaxis and growth in a long-term period. Wang et al. [77] studied the interaction between chemotaxis and growth on bacterial migration over two days. They conducted experiments in both laboratory and observation wells, and found that the combination of chemotaxis and growth significantly accelerated the bacterial propagation toward regions with a higher substrate concentration. However, O'Lenick et al. [60] observed a similar biodegradation rate of serine by bacterial strains with and without chemotaxis after 21 hours, and chemotaxis did not improve the bacterial migration.

These inconsistent observations illustrate that more studies are required to understand the effects of chemtoaxis on *in situ* bioremediation.

Another significant factor influencing bacterial survival and contaminant bioremediation is electron acceptor concentration. However, most chemotaxis-related research assumed that electron acceptors were in excess and not a rate-limiting compound [55, 67]. One exception is the study by Law [46], who found that low oxygen concentration could decrease naphthalene removal by reducing the naphthalene degradation rate and hence inhibiting chemotaxis toward the naphthalene source. The electron acceptor may inhibit contaminant degradation in the subsurface, where its availability is typically limited.

When chemotactic bacteria are injected into contaminated regions, they probably generate a traveling wave, including band and wave front, due to chemotaxis. The bacterial band moves as a population of bacteria with a maximum mass density while the front migrates with a bacterial plateau. This wave can significantly improve the removal of contaminants [50]. Adler [1] first experimentally observed such a bacterial wave in a capillary tube. Waves of *E. coli* formed due to metabolism-generated gradients in the concentration of oxygen and organic nutrients, and moved at a speed of about 1 cm/h, which is comparable with typical groundwater flow velocity. The substrate was consumed after the bacterial wave moved through, and the removal rate of the substrate is proportional to the moving speed of the bacterial wave. Saragosti et al. [74] also observed a traveling wave of *E. coli* in a channel filled with nutrients. The propagation speed was constant, and the shape of the wave was well conserved at the beginning of wave formation. How-

ever, Kim and Kim [40] found that the moving bacterial wave formed in assays slowed down gradually and stopped after about 4 hours, because a portion of the bacteria inside the wave remained behind during the process of wave migration and the diffusion of the chemical weakened the chemotactic strength. Therefore, further research is required to understand the formation and migration of traveling bacterial waves.

1.3 Mathematical model

The generalized Keller-Segel (K-S) model has been developed and widely used to simulate the movement of chemotactic bacteria [36, 37], and can be expressed by

$$\frac{\partial b}{\partial t} = \nabla \cdot (\mu(s)\nabla b) - \nabla \cdot (\chi(s) b \nabla s) + g(b,s) - h(b,s) \tag{1.1}$$

$$\frac{\partial s}{\partial t} = D\nabla^2 s - f(b,s) \tag{1.2}$$

where b is the density of bacterial population, s is the concentration of chemoattractant, $\mu(s)$ is the bacterial random motility coefficient, $\chi(s)$ is a function describing chemotaxis sensitivity, D is the chemoattractant diffusion coefficient, $g(b,s)$ and $h(b,s)$ are functions representing bacterial growth and death, respectively, and $f(b,s)$ is a function describing degradation of the chemoattractant. Various forms of the K-S model have been developed to simulate a wide range of biological systems [32, 75]. Hillen and Painter [30] reviewed the variations of the original Keller-Segel model and analyzed the existence of global

solutions.

Since Adler [1] experimentally observed bacterial waves moving toward chemoattractants in a capillary, many studies have been devoted to modeling this biological phenomenon. Keller and Segel [38] first used the K-S model to reproduce the wave formation observed in [1]. The authors assumed that neither bacterial growth nor death occurred during the timescale of interest and that the diffusion of the substrate could be ignored. They proposed a chemotactic coefficient:

$$\chi(s) = \frac{\chi_0}{s} \tag{1.3}$$

where χ_0 is a chemotactic sensitivity coefficient. This equation has a singularity at $s = 0$ and allows the K-S model to predict the formation of traveling bacterial waves when $\chi_0/\mu > 1$.

In order to advance mathematical analysis and improve precise dynamics of bacterial chemotaxis, Dahlquist et al. [15] designed an apparatus that could obtain detailed quantitative data on chemotaxis. Various initial bacteria and chemoattractant distributions were used to study the chemotactic response. Lapidus and Schiller [43] found that the K-S model with $\chi(s)$ in Eq. (1.3) could not successfully reproduce all of the experiments observed in [15]. Brown and Berg [11] used the tracking microscope to study the chemotactic response of *E. coli* toward temporal gradients of L-glutamate due to the sudden change of its concentration. They found that the drift velocity of bacteria up gradient of

chemoattractants was dependent on the chemoattractant concentration and a receptor-ligand binding dissociation constant K_d. Based on the experimental work of Brown and Berg [11], Lapidus and Schiller [44] proposed a revised form of the chemotactic coefficient

$$\chi(s) = \frac{\chi_0 K_d}{(K_d + s)^2} \tag{1.4}$$

By calculating the number of the bacteria migrating into an assay, Lapidus and Schiller [44] estimated the values of χ_0 and K_d. Model comparisons with experiments showed good agreement.

Rivero et al. [71] developed a transport model for chemotactic cell populations from a probabilistic model. This model allows for an estimation of the random motility coefficient μ and the chemotactic sensitivity coefficient χ_0 in terms of individual cell properties, such as swimming speed and temporal receptor occupation. Chen et al. [12] derived a similar expression by using extensive perturbation analysis and extended it to three spatial dimensions. The chemotactic strength in this model is represented by a chemotactic velocity $\mathbf{v}_c$ (equal to $\chi(s)\nabla s$)

$$\mathbf{v}_c = \frac{2v_s}{3} \tanh\left(\frac{\chi_0}{2v_s}\frac{K_d}{(K_d + s)^2}|\nabla s|\right)\frac{\nabla s}{|\nabla s|} \tag{1.5}$$

where v_s is bacterial swimming speed. Long and Hilpert [50] applied this model together with the K-S model to generalize the analytical solution for traveling waves in the presence of porous media. They also derived an analytical solution to predict the speed of the

traveling waves.

In this dissertation, we studied the reactive transport of chemotactic bacteria and dissolved chemicals by combining the K-S model with Rivero et al. [71]'s model. This model takes into account electron acceptor concentration and bacterial growth and decay that are described by a double-Monod kinetics model [70]. The resulting governing equations, referred to as reactive advection diffusion equations (ADEs), are given by

$$\frac{\partial b}{\partial t} + \nabla \cdot [b(\mathbf{v} + \mathbf{v}_c) - \mu \nabla b] = Y q_s \frac{s}{s + k_s} \frac{e}{e + k_e} b - kb \tag{1.6}$$

$$\frac{\partial s}{\partial t} + \nabla \cdot (s\mathbf{v} - D_s \nabla s) = -q_s \frac{s}{s + k_s} \frac{e}{e + k_e} b \tag{1.7}$$

$$\frac{\partial e}{\partial t} + \nabla \cdot (e\mathbf{v} - D_e \nabla e) = -q_e \frac{e}{e + k_e} \frac{s}{s + k_s} b \tag{1.8}$$

where e is the electron acceptor concentration, $\mathbf{v}$ is the advective velocity, D_s is the diffusion coefficient of the substrate, D_e is the diffusion coefficient of the electron acceptor, Y is the yield coefficient, k is the decay rate, q_s is the maximum reaction rate of the substrate, q_e is the maximum reaction rate of the electron acceptor, k_s is the half-saturation coefficient of the substrate, and k_e is the half-saturation coefficient of the electron acceptor. If the electron acceptor is not a rate-limiting chemical, the reactive ADEs can be simplified to

$$\frac{\partial b}{\partial t} + \nabla \cdot [b(\mathbf{v} + \mathbf{v}_c) - \mu \nabla b] = Y q_s \frac{s}{s + k_s} b - kb \tag{1.9}$$

$$\frac{\partial s}{\partial t} + \nabla \cdot (s\mathbf{v} - D_s \nabla s) = -q_s \frac{s}{s + k_s} b \tag{1.10}$$

These equations are usually normalized first to apply numerical methods to approximate their solutions [50].

The estimation of the bacterial random motility and the chemotactic sensitivity coefficients is pivotal for predicting the propagation of chemotactic bacteria. The estimated parameter values span several orders of magnitude due to the effects of growth medium, experimental types and conditions [49]. For example, the best-fit value of chemotactic sensitivity coefficient for a *P. putida* G7 and naphthalene system in Pedit et al. [67]'s experiment is about four times lower than the value for the same bacteria and substrate in Marx and Aitken [55]'s experiment. In order to reduce the effects of bacterial growth on chemotaxis analysis, chemicals are usually added to inhibit the growth of bacteria in laboratories such that one can focus on chemotaxis [67].

Marx and Aitken [55] modeled the response of *P. putida* to naphthalene for different bacterial and chemoattractant concentrations. Particularly, they considered the effect of chemoattractant diffusion on bacterial aggregation in a capillary and determined the chemotactic sensitivity coefficient. Marx and Aitken [54] further explored the effect of chemoattractant consumption on the chemotactic response. They found that the depletation of the chemoattractant reduced the bacterial migration when the chemoattractant concentration was low. Furthermore, Law and Aitken [47] designed a continuous-flow capillary assay to measure the bacterial chemotaxis and estimated the chemotactic coefficients. They used a small concentration of chemoattractant to minimize the metabolism of the chemoattractant. The modeling results agreed well with the experiment. Lewus

and Ford [49] quantified the bacterial motility and chemotaxis by fitting different mathematical models to experimental data. They found that accurate bacterial transport coefficients could be achieved if the experiment was performed carefully and the mathematical model was selected appropriately. Ford and Harvey [19] also estimated the motility and chemotaxis coefficients of bacterial populations by using swimming properties of individual bacteria, such as swimming speed, tumbling frequency, and turn angle distribution. They found that the motility could improve effective bacterial transport in porous media, which was dependent on hydrodynamic dispersion and pore diameter. Different formulas were used to estimate the effective values of motility and chemotaxis in porous media in terms of the average pore diameter.

Kennedy and Aris [39] investigated different functional forms of bacterial growth and death in a K-S model. They found that certain growth functions generated traveling wave solutions even though there was no chemotaxis. The wave speed increased with the additional mechanism of chemotaxis. Lauffenburger et al. [45] further studied the formation of traveling waves caused by bacterial growth, death, and random motility. They revealed that the governing equations generated a traveling wave solution, which was called growth/death/motility wave. The speed of this wave and the size of the bacterial population were proportional to the square-root of the random motility coefficient. When chemotaxis occurred, it accelerated the migration of traveling waves, and the extent of this acceleration depended on the functional form of the chemotactic coefficient.

1.4 Lattice Boltzmann method

Both large-scale and pore-scale models have been developed to study fluid flow and solute transport in the subsurface [14, 50]. In large-scale simulations, physical properties (such as flow velocity, pressure, and solute concentration) are averaged over a representative elementary volume. The characteristics of pore geometry are represented by macroscopic parameters such as porosity and permeability. The simulations can predict flow field and concentration distribution at large scales, but it is not always clear whether pore-scale processes are accounted for appropriately. By contrast, pore-scale simulations examine fluid flow and solute transport in pore areas, where biogeochemical reactions and interactions between the aqueous solution and solid surfaces are directly calculated [56]. Therefore, studies of pore-scale reactive transport can deepen our understanding of large-scale natural processes [7]. With the rapidly growing availability of high performance computational resources, pore-scale simulations have become a powerful tool for investigating a broad range of porous medium transport phenomena [58, 69].

Since its introduction [29], LBM has been widely used for simulating a broad range of flow and transport phenomena. This method has become particularly popular when analyzing porous medium processes at the pore scale, because voxel images of porous media can be used directly as an input to the simulations [59, 51, 79, 57, 10]. Different from conventional numerical schemes that discretize macroscopic continuum equations (e.g., finite-difference and finite-element schemes), LBM is based on microscopic models and mesoscopic kinetic equations. In the LBM, fluids, solutes, or microorganisms are

represented by particles that move on a typically regular lattice. Evolution of the particles in time is achieved by repeatedly performing a travel and a collision step. During the travel step, particles move from one lattice node to another. Then particles that are present at a node and that have different velocities collide with each other. During this collision step, the particle velocity distribution approaches an equilibrium distribution, and the rate of approach is controlled by one or more relaxation times. By incorporating the essential physics of microscopic processes of the particles to kinetic models, LBM enables the macroscopic averaged quantities to obey macroscopic equations, such as Navier-Stokes (NS) equations [13] or reactive ADEs [31].

The simplest LBM is the lattice Bhatnagar-Gross-Krook (BGK) method, which is based on a single relaxation time (SRT) approximation and referred to as SRT-LBM [9]. The SRT-LBM has been most widely used due to its simplicity, and presents the following evolution equation:

$$f_i(\mathbf{r} + \mathbf{c_i}, t+1) - f_i(\mathbf{r}, t) = -\frac{1}{\tau}(f_i(\mathbf{r}, t) - f_i^{eq}(\mathbf{r}, t)) + R \tag{1.11}$$

where $\mathbf{c_i}$ is the ith direction of discrete velocities in a prescribed lattice, f_i is the particle distribution function along $\mathbf{c_i}$ at each lattice node $\mathbf{r}$ and for each discrete time t, f_i^{eq} is the equilibrium particle distribution that only depends on macroscopic properties, R is the source term that represents the reactive transport of the particles, and τ is the single relaxation time that depends on kinematic viscosity in flow simulations and diffusion

coefficient in transport simulations. The lattices with 15, 19 or 27 discrete velocity directions are mostly used in 3D lattice Boltzmann (LB) modelings, and they are referred to as D3Q15, D3Q19, or D3Q27 models, respectively [4].

Although the SRT-LBM is easy to implement, it suffers from some well-known deficiencies. For example, it is prone to numerical instability, and the kinetic viscosity is dependent on the presence of pore boundaries [28]. A multiple-relaxation-time (MRT) LBM (also referred to as generalized LBM) can improve numerical stability and reduce the dependence of viscosity on pore boundary by tuning multiple relaxation times to achieve optimal solutions [17, 63]. This method is expressed by

$$\mathbf{f}(\mathbf{r}+\mathbf{c_i},t+1)-\mathbf{f}(\mathbf{r},t)=-\mathbf{S}(\mathbf{f}(\mathbf{r},t)-\mathbf{f}^{eq}(\mathbf{r},t))+R \tag{1.12}$$

where $\mathbf{S}$ is a collision matrix. When $\mathbf{S}=\mathbf{I}/\tau$ where $\mathbf{I}$ is the identity matrix, the MRT-LBM is reduced to a SRT-LBM. When implementing the MRT-LBM, one usually introduces a transformation matrix $\mathbf{M}$ to transform the particle distribution function vector $\mathbf{f}$ into a moment vector $\mathbf{m}$ through a linear mapping $\mathbf{m}=\mathbf{M}\mathbf{f}$ [18, 63]. d'Humières et al. [18] derived appropriate forms of $\mathbf{M}$ and equilibrium moment vector $\mathbf{m}$ and used the MRT LB model to simulate a driven cavity flow. Although the MRT-LBM can enhance numerical stability and accuracy, its selection of optimal relaxation times is a challenge, and it is complicated to implement compared to the SRT-LBM [18].

Another promising LBM is two-relaxation-time (TRT) LBM [21, 22, 25], which de-

composed the particle distribution into symmetric and antisymmetric components, $f_i = f_i^+ + f_i^-$, where $f_i^+ = (f_i + f_{\bar{i}})/2$, $f_i^- = (f_i - f_{\bar{i}})/2$, and the index $\bar{i}$ denotes the opposite direction of the ith discrete velocity $\mathbf{c_i}$. The evolution of the particle distribution function is described by

$$f_i(\mathbf{r} + \mathbf{c}_i, t+1) = f_i(\mathbf{r}, t) - s^+(f_i^+ - f_i^{eq^+}) - s^-(f_i^- - f_i^{eq^-}) + R \tag{1.13}$$

where s^+ and s^- are eigenvalues of this expression, e_q^+ and e_q^- are the symmetric and antisymmetric components of equilibrium particle distribution e_q, respectively, $e_q^+ + e_q^- = e_q$. The TRT model has one free eigenvalue to select between 0 and 2 to guarantee numerical stability, such as s^- is free for flow simulations and s^+ is free for transport simulations. The other one is determined by kinematic viscosity or chemical diffusion [23]. This model is reduced to a SRT-LBM if $s^+ = s^- = 1/\tau$. The TRT-LBM is computationally efficient and can eliminate numerical diffusion by including a velocity correction term [24].

When simulating fluid flow, the fluid mass is conserved and therefore the reaction term $R = 0$. The dimensionless fluid density ρ and momentum $\rho\mathbf{V}$ ($\mathbf{V}$ is the dimensionless form of the advective velocity $\mathbf{v}$) can be obtained from the particle distribution as follows:

$$\rho = \sum_i f_i, \quad \rho\mathbf{V} = \sum_i f_i \mathbf{e}_i \tag{1.14}$$

Since the LBMs are compressible, the pressure in the fluid field can be estimated by

an equation of state [13]. Via the Chapman-Enskog expansion [20], the LB equations Eq. (1.11), Eq. (1.12), and Eq. (1.13) can be recovered to NS equations in the limit of a small Mach number, which means that the dimensionless advective velocity is small. The elaborate derivation can be found in [13, 18, 22].

For reactive transport simulations, the dimensionless solute concentration C and the mass flux are described by

$$C = \sum_i f_i, \quad C\mathbf{V} = \sum_i f_i \mathbf{e}_i \tag{1.15}$$

If there exists bacterial chemotaxis, $\mathbf{V} = \mathbf{V} + \mathbf{V}_c$ where $\mathbf{V}_c$ is dimensionless chemotactic velocity. The LB equations Eq. (1.11), Eq. (1.12), and Eq. (1.13) can obtain the solutions to reactive ADEs under small Mach number [31]. Dawson et al. [16] developed a LB model for simulating reactive diffusive transport. They simulated pure diffusion and homogeneous chemical reactions. The simulation results agreed well with theoretical prediction and captured the fundamental physics of macroscopic reaction-diffusion equations. Kang et al. [35] applied LBMs to simulate solute reactive transport in both pore spaces and at fluid/solid interfaces. They used different methods to update solid phase when mass transfer took place between solid and solute due to chemical dissolution and/or precipitation.

Hilpert [31] developed a 2D LB model to simulate bacterial chemotaxis. This model reproduced traveling waves of bacteria along metabolism-generated gradients in substrate

concentrations as considered by Keller and Segel [38]. The author simulated the chemotactic response of *P. putida* to naphthalene in bulk liquids, and found that only a portion of a bacterial slug formed a traveling wave as the slug length exceeded a critical value. Long and Hilpert [50] further extended the 2D model to a 3D model. They modeled the bacterial movement and contaminant biodegradation in both bulk liquids and subsurface environments. The results showed that the bacteria could form waves moving both upstream and downstream under typical groundwater flow velocity.

LBMs are generally well-suited to model fluid flow and reactive transport in complex geometries due to their kinetic properties and easily-applied standard bounce-back (SBB) boundary condition [13, 16]. Moreover, LBMs are easy to implement on parallel computational platforms because of their explicit time stepping and computational locality [62]. With the continuous increases in the capability of computing resources, LBMs have become a popular method for simulating complex flows, such as turbulence, multiphase flow, microfluidics, and particle suspensions [4]. Therefore we use LBMs in this study.

1.5 Outline of the dissertation

Chapter 2 to 4 represent papers that are: Chapter 2, "A Multiple-relaxation-time Lattice-Boltzmann Model for Bacterial Chemotaxis: Effects of Initial Concentration, Diffusion, and Hydrodynamic Dispersion on Traveling Bacterial Bands" has been published in *Bulletin of Mathematical Biology*. This paper developed a MRT-LBM to model chemotaxis and investigated the effects of substrate diffusion, initial bacterial concentration, and

hydrodynamic dispersion on the formation, shape, and propagation of bacterial bands. Chapter 3, "Coupled Effects of Chemotaxis and Growth on Traveling Bacterial Waves" has been published in *Journal of Contaminant Hydrology*. This paper studied the coupled effects of chemotaxis and growth on bacterial migration, and examined their effects on contaminant remediation. Chapter 4, "A Pedestrian's Guide to a Numerical-Diffusion-Free Two-relaxation-time Lattice Boltzmann Model for Reactive Diffusive Transport" will be submitted to *Water Resources Research*. This paper introduced the TRT-LBM and applied this model to study isotropic advective diffusion and reactive transport. In Chapter 5, the research findings are concluded, the engineering applications of bacterial chemotaxis are described, and the future research possibilities are discussed.

Bibliography

[1] J.P. Adler. Chemotaxis in bacteria. *Science*, 153:708–716, 1966.

[2] US Environment Protection Agency. Cleaning up the nation's waste sites: markets and technology trends. 2004.

[3] T. Ahmed, T.S. Shimizu, and R. Stocker. Bacterial chemotaxis in linear and nonlinear steady microfluidic gradients. *Nano Letters*, 10(9):3379–3385, September 2010.

[4] C.K. Aidun and J.R. Clausen. Lattice-Boltzmann method for complex flows. *Annual Review of Fluid Mechanics*, 42:439–472, September 2010.

[5] M. Alexander. *Biodegradation and bioremediation*. Academic Press, 1999.

[6] G. Alexandre, S. Greer-Phillips, and I. Zhulin. Ecological role of energy taxis in microorganisms. *FEMS Microbiology Reviews*, 28(1):113–126, feb 2004.

[7] I. Battiato, D.M. Tartakovsky, A.M. Tartakovsky, and T.D. Scheibe. Hybrid models of reactive transport in porous and fractured media. *Advances in Water Resources*, 34:1140–1150, 2011.

[8] H.C. Berg and L. Turner. Chemotaxis of bacteria in glass capillary arrays.Escherichia

coli, motility, microchannel plate, and light scattering. *Biophysical Journal*, 58(4): 919–930, October 1990.

[9] P. Bhatnagar, E. Gross, and M. Krook. A Model for Collision Processes in Gases.I.Small Amplitude Processes in Charged and Neutral One-Component Systems. *Physical Review*, 94(3):511–525, May 1954.

[10] M.J. Blunt, B. Bijeljic, H. Dong, O. Gharbi, S. Iglauer, P. Mostaghimi, A. Paluszny, and C. Pentland. Pore-scale imaging and modelling. *Advances in Water Resources*, 51:197–216, January 2013.

[11] D.A. Brown and H.C. Berg. Temporal stimulation of chemotaxis in Escherichia coli. *Proceedings of the National Academy of Sciences of the United States of America*, 71(4):1388–1392, April 1974.

[12] K.C. Chen, P.T. Cummings, and R.M. Ford. Perturbation Expansion of Alt's Cell Balance Equations Reduces to Segel's One-Dimensional Equations for Shallow Chemoattractant Gradients. *SIAM Journal on Applied Mathematics*, 1998.

[13] S. Chen and G. Doolen. Lattice Boltzmann method for fluid flows. *Annual Review of Fluid Mechanics*, 30:329–364, 1998.

[14] T.P. Clement, Y. Sun, B.S. Hooker, and J.N. Petersen. Modeling Multispecies Reactive Transport in Ground Water. *Ground Water Monitoring and Remediation*, 18(2):79–92, May 1998.

[15] F.W. Dahlquist, P. Lovely, and D.E. Koshland. Quantitative analysis of bacterial migration in chemotaxis. *Nature: New Biology*, 236(65):120–123, March 1972.

[16] S. Dawson, S. Chen, and G.D. Doolen. Lattice Boltzmann computations for reaction-diffusion equations. *The Journal of Chemical Physics*, 98(2):1514, 1993.

[17] D. d'Humières. Generalized lattice-Boltzmann equations. *Rarefied Gas Dynamics-Theory and Simulations; Proceedings of the 18th International Symposium on Rarefied Gas Dynamics, Univ.of British Columbia, Vancouver, Canada; United States*, pages 26–30, 1992.

[18] D. d'Humières, I. Ginzburg, M. Krafczyk, P. Lallemand, and L.S. Luo. Multiple-relaxation-time lattice Boltzmann models in three dimensions. *Philosophical Transactions of The Royal Society of London Series A*, 360(1792):437–451, 2002.

[19] R.M. Ford and R.W. Harvey. Role of chemotaxis in the transport of bacteria through saturated porous media. *Advances in Water Resources*, 30(6-7):1608–1617, June 2007.

[20] U. Frisch, D. d'Humieres, and B. Hasslacher. Lattice gas hydrodynamics in two and three dimensions. *Complex Systems 1*, 1, January 1987.

[21] I. Ginzburg. Generic boundary conditions for lattice Boltzmann models and their application to advection and anisotropic dispersion equations. *Advances in Water Resources*, 28(11):1196–1216, November 2005.

[22] I. Ginzburg. Equilibrium-type and link-type lattice Boltzmann models for generic advection and anisotropic-dispersion equation. *Advances in Water Resources*, 28 (11):1171–1195, 2005.

[23] I. Ginzburg. Truncation Errors, Exact and Heuristic Stability Analysis of Two-Relaxation-Times Lattice Boltzmann Schemes for Anisotropic Advection-Diffusion Equation. *Communications in Computational Physics*, 11:1439–1502, December 2012.

[24] I. Ginzburg. Multiple anisotropic collisions for advection-diffusion Lattice Boltzmann schemes. *Advances in Water Resources*, 51:381–404, January 2013.

[25] I. Ginzburg and F. Verhaeghe. Two-relaxation-time lattice Boltzmann scheme: About parametrization, velocity, pressure and mixed boundary conditions. *Communications in Computational Physics*, 3(2):427–478, February 2008.

[26] A.C. Grimm and C.S. Harwood. Chemotaxis of $Pseudomonas$ spp.to the polyaromatic hydrocarbon naphthalene. *Applied and Environmental Microbiology*, 63(10): 4111–4115, 1997.

[27] A.C. Hawkins and C.S. Harwood. Chemotaxis of Ralstonia eutropha JMP134 (pJP4) to the herbicide 2, 4-dichlorophenoxyacetate. *Applied and Environmental Microbiology*, 68(2):968–972, February 2002.

[28] X. He, Q. Zou, L Luo, and M. Dembo. Analytic solutions of simple flows and analysis

of nonslip boundary conditions for the lattice Boltzmann BGK model. *Journal of Statistical Physics*, 1997.

[29] F.J. Higuera and J. Jimenez. Boltzmann approach to lattice gas simulations. *EPL (Europhysics Letters)*, 1989.

[30] T. Hillen and K.J. Painter. A user's guide to PDE models for chemotaxis. *Journal of Mathematical Biology*, 58:183–217, 2009.

[31] M. Hilpert. Lattice-Boltzmann model for bacterial chemotaxis. *Journal of Mathematical Biology*, 51(3):302–332, May 2005.

[32] D. Horstmann. From 1970 until present: the Keller-Segel model in chemotaxis and its consequences I. *Jahresbericht DMV*, 105(3):103–165, 2003.

[33] R. Jittawattanarat and K. Kostarelos. Immobilized cell augmented activated sludge process for enhanced nitrogen removal from wastewater. *Water Environment Research*, 79(11):2325–2335, May 2007.

[34] K.S. Jorgensen. In situ bioremediation. *Advances in Applied Microbiology*, 61:285–305, February 2007.

[35] Q. Kang, P.C. Lichtner, and D.R. Janecky. Lattice Boltzmann method for reacting flows in porous media. *Advances in Applied Mathematics and Mechanics*, 2:545–563, January 2010.

[36] E.F. Keller and L.A. Segel. Initiation of slime mold aggregation viewed as an instability. *Journal of Theoretical Biology*, 26:399–415, 1970.

[37] E.F. Keller and L.A. Segel. Model for chemotaxis. *Journal of Theoretical Biology*, 30:225–234, 1971.

[38] E.F. Keller and L.A. Segel. Traveling bands of chemotactic bacteria: a theoretical analysis. *Journal of Theoretical Biology*, 30:235–248, 1971.

[39] C. Kennedy and R. Aris. Traveling waves in a simple population model involving growth and death. *Bulletin of Mathematical Biology*, 42(3):397–429, 1980.

[40] M. Kim and T. Kim. Diffusion-based and long-range concentration gradients of multiple chemicals for bacterial chemotaxis assays. *Analytical Chemistry*, 82(22): 9401–9409, November 2010.

[41] S. Labana, G. Pandey, D. Paul, and N.K. Sharma. Pot and field studies on bioremediation of p-nitrophenol contaminated soil using Arthrobacter protophormiae RKJ100. *Environmental Science and Technology*, 39(9):3330–3337, May 2005.

[42] S. Labana, O.V. Singh, A. Basu, and G. Pandey. A microcosm study on bioremediation of p-nitrophenol-contaminated soil using Arthrobacter protophormiae RKJ100. *Applied Microbiology and and Biotechnology*, 68(3):417–424, August 2005.

[43] I.R. Lapidus and R. Schiller. Bacterial chemotaxis in a fixed attractant gradient. *Journal of Theoretical Biology*, 53(1):215–222, September 1975.

[44] I.R. Lapidus and R. Schiller. Model for the chemotactic response of a bacterial population. *Biophysical Journal*, 16(7):779–789, July 1976.

[45] D. Lauffenburger, C.R. Kennedy, and R. Aris. Traveling bands of chemotactic bacteria in the context of population growth. *Bulletin of Mathematical Biology*, 46(1):19–40, 1984.

[46] A. Law. The effect of oxygen on chemotaxis to naphthalene by Pseudomonas putida G7. *Biotechnology and Bioengineering*, 93(3):457–464, February 2006.

[47] A. Law and M. Aitken. Continuous-flow capillary assay for measuring bacterial chemotaxis. *Applied and Environmental Microbiology*, 71(6):3137–3143, June 2005.

[48] A. Law and M. Aitken. Bacterial chemotaxis to naphthalene desorbing from a non-aqueous liquid. *Applied and Environmental Microbiology*, 69:5968–5973, 2003.

[49] P. Lewus and R.M. Ford. Quantification of random motility and chemotaxis bacterial transport coefficients using individual-cell and population scale assays. *Biotechnology and Bioengineering*, 75:292–304, 2001.

[50] W. Long and M. Hilpert. Lattice-Boltzmann modeling of contaminant degradation by chemotactic bacteria: Exploring the formation and movement of bacterial bands. *Water Resources Research*, 44:W09415, 2008.

[51] W. Long, H. Huang, J. Serlemitsos, E.B. Liu, A.H. Reed, , and M. Hilpert. A correlation for the collector efficiency of nanoparticles for clean-bed filtration in packings

of nonspherical collectors. *Colloids and Surfaces A: Physicochemical and Engineering Aspects*, 358:163–171, 2010.

[52] D.M. Mackay and J.A. Cherry. Groundwater contamination: pump-and-treat remediation. *Environmental Science and Technology*, 23(6):630–636, June 1989.

[53] M. Mansour. On traveling wave fronts in a bacterial growth model with density-dependent diffusion and chemotaxis. *Journal of Statistical Physics*, 143(1):197–204, 2011.

[54] R.B. Marx and M.D. Aitken. Bacterial chemotaxis enhances naphthalene degradation in a heterogeneous aqueous system. *Environmental Science and Technology*, 34: 3379–3383, 2000.

[55] R.B. Marx and M.D. Aitken. Quantification of chemotaxis to naphthalene by *Pseudomonas putida* G7. *Applied and Environmental Microbiology*, 65:2847–2852, 1999.

[56] P. Meakin and A. Tartakovsky. Modeling and simulation of porescale multiphase fluid flow and reactive transport in fractured and porous media. *Reviews of Geophysics*, July 2009.

[57] R. Moreno-Atanasio, R.A. Williams, and X. Jia. Combining X-ray microtomography with computer simulation for analysis of granular and porous materials. *Particuology*, 8(2):81–99, April 2010.

[58] P.P. Mukherjee, Q. Kang, and C. Wang. Pore-scale modeling of two-phase transport

in polymer electrolyte fuel cells—progress and perspective. *Energy and Environmental Science*, 4(2):346, 2011.

[59] H. Okabe and M.J. Blunt. Prediction of permeability for porous media reconstructed using multiple-point statistics. *Physical Review E, Statistical, Nonlinear, and Soft Matter Physics*, 70(6 Pt 2):066135, December 2004.

[60] C.J. O'Lenick, P.R. Bienkowski, P.D. Frymier, and R.N. Weinstein. Effect of Bacterial Chemotaxis on Biodegradation in a Porous Medium. *Bioremediation Journal*, 12(3): 131–144, August 2008.

[61] M.S. Olson, R.M. Ford, J.A. Smith, and E.J. Fernandez. Quantification of bacterial chemotaxis in porous media using magnetic resonance imaging. *Environmental Science and Technology*, 38(14):3864–3870, July 2004.

[62] C. Pan, J.F. Prins, and C.T. Miller. A high-performance lattice Boltzmann implementation to model flow in porous media. *Computer Physics Communications*, 158 (2):89–105, April 2004.

[63] C. Pan, L. Luo, and C.T. Miller. An evaluation of lattice Boltzmann schemes for porous medium flow simulation. *Computers and Fluids*, 35(8-9):898–909, 2006.

[64] G. Pandey and R.K. Jain. Bacterial chemotaxis toward environmental pollutants: role in bioremediation. *Applied and Environmental Microbiology*, 68(12):5789–5795, December 2002.

[65] J. Pandey, A. Chauhan, and R.K. Jain. Integrative approaches for assessing the ecological sustainability of in situ bioremediation. *FEMS Microbiology Reviews*, 33 (2):324–375, March 2009.

[66] R.E. Parales, J.L. Ditty, and C.S. Harwood. Toluene-degrading bacteria are chemotactic towards the environmental pollutants benzene, toluene, and trichloroethylene. *Applied and Environmental Microbiology*, 66(9):4098–4104, September 2000.

[67] J.A. Pedit, R.B. Marx, C.T. Miller, and M.D. Aitken. Quantitative analysis of experiments on bacterial chemotaxis to naphthalene. *Biotechnology and Bioengineering*, 78(6):626–634, June 2002.

[68] L.W. Perelo. Review: In situ and bioremediation of organic pollutants in aquatic sediments. *Journal of Hazardous Materials*, 177(1-3):81–89, May 2010.

[69] A. Raoof, H.M. Nick, T.K.T. Wolterbeek, and C.J. Spiers. Pore-scale modeling of reactive transport in wellbore cement under CO2 storage conditions. *International Journal of Greenhouse Gas Control*, 11:S67–S77, November 2012.

[70] B.E. Rittmann and P.L. McCarty. *Environmental biotechnology*. principles and applications. McGraw-Hill Science/Engineering/Math, 2001.

[71] M.A. Rivero, R.T. Tranquillo, H.M. Buettner, and D. Lauffenburger. Transport models for chemotactic cell populations based on individual cell behaviour. *Chemical Engineering Science*, 44(12):2881–2897, 1989.

[72] C.J. Roush, C.M. Lastoskie, and R.M. Worden. Denitrification and chemotaxis of Pseudomonas stutzeri KC in porous media. *Journal of Environmental Science and Health.Part A, Toxic/hazardous Substances and Environmental Engineering*, 41(6): 967–983, 2006.

[73] S.K. Samanta, B. Bhushan, and A. Chauhan. Chemotaxis of a Ralstonia sp.SJ98 toward different nitroaromatic compounds and their degradation. *Biochemical and Biophysical Research Communications*, 269(1):117–123, May 2000.

[74] J. Saragosti, V. Calvez, N. Bournaveas, A. Buguin, P. Silberzan, and B. Perthame. Mathematical description of bacterial traveling pulses. *PLoS Computational Biology*, 6(8), 2010.

[75] M.J. Tindall, P.K. Maini, S.L. Porter, and J.P. Armitage. Overview of mathematical approaches used to model bacterial chemotaxis II: bacterial populations. *Bulletin of Mathematical Biology*, 70(6):1570–1607, August 2008.

[76] G.M. Walker, J. Sai, A. Richmond, M. Stremler, C.Y. Chung, and J.P. Wikswo. Effects of flow and diffusion on chemotaxis studies in a microfabricated gradient generator. *Lab on A Chip*, 5(6):611–618, June 2005.

[77] M. Wang, R.M. Ford, and R.W. Harvey. Coupled effect of chemotaxis and growth on microbial distributions in organic-amended aquifer sediments: observations from laboratory and field studies. *Environmental Science and Technology*, 42(10):3556–3562, May 2008.

[78] X. Wang and T. Long. Bacterial chemotaxis toward a NAPL source within a pore-scale microfluidic chamber. *Biotechnology and Bioengineering*, 109(7):1622–1628, July 2012.

[79] C.J. Werth, C. Zhang, M.L. Brusseau, M. Oostrom, and T. Baumann. A review of non-invasive imaging methods and applications in contaminant hydrogeology research. *Journal of Contaminant Hydrology*, 113(1-4):1–24, April 2010.

Chapter 2. A Multiple-relaxation-time Lattice-Boltzmann Model for Bacterial Chemotaxis: Effects of Initial Concentration, Diffusion, and Hydrodynamic Dispersion on Traveling Bacterial Bands.

2.1 Abstract

Bacterial chemotaxis can enhance the bioremediation of contaminants in aqueous and subsurface environments if the contaminant is a chemoattractant that the bacteria degrade. The process can be promoted by traveling bands of chemotactic bacteria that form due to metabolism-generated gradients in chemoattractant concentration. We developed a multiple-relaxation-time (MRT) lattice Boltzmann method (LBM) to model chemotaxis, because LBMs are well-suited to model reactive transport in the complex geometries that

This paper except the Appendix B has been published (Yan Z. and Hilpert M.,*Bulletin of Mathematical Biology*, 76(10):2449-75, 2014 Oct.)

are typical for subsurface porous media. This MRT-LBM can attain a better numerical stability than its corresponding single-relaxation-time LBM. We performed simulations to investigate the effects of substrate diffusion, initial bacterial concentration, and hydrodynamic dispersion on the formation, shape, and propagation of bacterial bands. Band formation requires a sufficiently high initial number of bacteria and a small substrate diffusion coefficient. Uniform flow does not affect the bands while shear flow does. Bacterial bands can move both upstream and downstream when the flow velocity is small. However, the bands disappear once the velocity becomes too large due to hydrodynamic dispersion. Generally bands can only be observed if the dimensionless ratio between the chemotactic sensitivity coefficient and the effective diffusion coefficient of the bacteria exceeds a critical value, that is, when the biased movement due to chemotaxis overcomes the diffusion-like movement due to the random motility and hydrodynamic dispersion.

2.2 Introduction

Chemotaxis enables motile bacteria to sense chemical gradients in their surrounding environment and to move toward regions with high chemical concentration [2]. A large number of harmful chemicals (e.g., toluene, benzene, naphthalene, polycyclic aromatic hydrocarbons, and trichloroethylene) are found to be chemoattractants for various bacterial strains [42, 43, 38, 33, 55]. Chemotaxis can increase bioavailability of pollutants and accelerate their removal in aqueous and subsurface environments [15, 48, 16, 32].

A traveling band, a population of bacteria with a density maximum, can potentially

enhance contaminant degradation [29]. Adler [1] first observed the formation of traveling bands of chemotactic bacteria in capillary tubes. Bands of *E. coli* formed due to metabolism-generated gradients in the concentration of oxygen and organic nutrients, and moved at a speed of several mm/h. Afterward, several research groups reported the formation and propagation of bands in bacterial suspensions [6, 44]. However, bacterial chemotaxis does not always result in such bands. The bands are, for example, affected by chemoattractant diffusion, bacterial density, and hydrodynamic dispersion. The present study examines these dependencies.

A variety of mathematical models for chemotaxis has been developed. The Keller-Segel model has been proposed as a basis for modeling the propagation of traveling bands [26]. Tindall et al. [53] reviewed the application of mathematical modeling to understand the behavior of populations of chemotactic bacteria. Hillen and Painter [18] explored variations of the original Keller-Segel model. The existence of bacterial bands was typically investigated by considering different combinations of chemotactic sensitivity functions, production models and degradation expressions [21, 56]. These studies usually took advantage of mathematical conveniences, which do not always represent realistic microbial processes. Rivero et al. [47] developed a transport model for chemotactic cell populations from a probabilistic model, which was based on individual cell behavior. Furthermore, a new class of models for the collective motion of cells has emerged. In contrast to K-S models, in which the chemotactic fluxes are described by intuitive rules (or first-order approximations), these new models derive the fluxes from a mesoscopic description of

the run-and-tumble dynamics at the individual level and account for internal molecular pathways [39, 49, 50]. This type of model successfully modeled the phenomenon that the mean chemotactic velocity of *E. coli* cells increased monotonically with the spatial gradient of the logarithmic ligand concentration [25]; however, these model are restricted to small gradients in ligand concentration.

Numerical modeling approaches simulate bacterial chemotaxis either at the cell or at the population scale. Many of the population-scale approaches are based on finite difference or finite element formulations [11, 4, 36, 45, 54, 57], while random walk methods are used at the cell scale [12, 37]. Jabbarzadeh and Abrams [22, 23] coupled the finite difference method and the random walk method to simulate chemotaxis in a two-dimensional (2D) porous medium. Brosilow et al. [5] developed a lattice-Boltzmann method (LBM) for chemotaxis based on the idea that the Alt-Stroock equation for the run-and-tumble motion of bacteria is similar to the Boltzmann equation from gas dynamics. In the LBM, both bacteria and chemoattractants are represented by quasi-particles that move along a numerical lattice. In contrast to conventional methods, LBMs are generally well-suited to model transport in complex geometries due to their kinetic properties and easily-applied standard bounce-back (SBB) boundary conditions [7]. This SBB scheme is most widely used due to its simplicity, although corrections to the scheme can improve the numerical accuracy [24, 3]. Moreover, LBMs are easy to implement on parallel computational platforms because of the explicit time stepping and the locality of the computations [7, 40], although the development of parallel linear solvers has also facilitated the solution of

PDEs by conventional implicit methods on parallel platforms. Hilpert [19] developed a 2D single-relaxation-time (SRT) LBM that mimics solutions to the population-scale mass balance equations for chemotactic bacteria. Long and Hilpert [29] then extended the 2D model to a three-dimensional (3D) SRT-LBM.

In this paper, we implement a general reactive transport model based on the Keller-Segel model to study bacterial chemotaxis. Our mathematical model is able to represent relatively realistic microbial processes by accounting for bacterial growth and decay. First, we develop a novel 3D multiple-relaxation-time (MRT) LBM, which can achieve a better numerical stability than the corresponding SRT-LBM [9, 10]. This MRT model can simulate chemotactic processes in liquids that flow with relatively high convective velocity, for which Long and Hilpert [29]'s SRT model probably become numerically unstable. Section 2.3 presents the mathematical model and the corresponding MRT-LBM, while the Appendix contains the detailed mathematical model derivation. In section 2.4, we use this model to study the effects of substrate diffusion, initial bacterial concentration, and hydrodynamic dispersion on the formation, shape, and propagation of bacterial bands.

2.3 Model

2.3.1 Continuum-scale models for chemotaxis

Bacterial chemotaxis in a fluid can be described by partial differential equations (PDEs) that are based on mass balance equations [27, 20, 18]. In this work, we consider a system

in which the substrate is the only rate-limiting chemical, the reaction between the bacteria and the substrate is described by a Monod kinetics model, and the fluid is allowed to flow. The resulting two PDEs are given by

$$\frac{\partial b}{\partial t} + \vec{\nabla} \cdot \left[b(\vec{v} + \vec{v}_c) - \mu \vec{\nabla} b \right] = Yq \frac{s}{s + k_s} b - kb \tag{2.1}$$

$$\frac{\partial s}{\partial t} + \vec{\nabla} \cdot (s\vec{v} - D\vec{\nabla} s) = -q \frac{s}{s + k_s} b \tag{2.2}$$

where b is the bacterial concentration, s is the substrate concentration, $\vec{v}$ is the pore-water velocity, $\vec{v}_c$ is the chemotactic velocity, μ is the random motility coefficient of the bacteria, D is the diffusion coefficient of the substrate, q is the maximum reaction rate, k_s is the half-saturation coefficient, Y is the yield coefficient, and k is the decay rate. The chemotactic velocity is assumed to depend on the concentration of the substrate and its gradient, and can be described by the model derived by Rivero et al. [47]:

$$\vec{v}_c = \frac{2v_s}{3} \tanh \left(\frac{\chi_0}{2v_s} \frac{K_d}{(K_d + s)^2} |\vec{\nabla} s| \right) \frac{\vec{\nabla} s}{|\vec{\nabla} s|} \tag{2.3}$$

where v_s is the bacterial swimming speed, K_d is a dissociation constant, and χ_0 is the chemotactic sensitivity coefficient. This model is valid also for large gradients of chemoattractant concentration and ensures that the population velocity $\vec{v}_c$ does not exceed the bacterial swimming speed. Although the motility of bacteria is affected by fluid velocity, we neglect this interference due to the small fluid velocity gradients and small hydrodynamic

stresses in our study [30].

Like Long and Hilpert [29], we first nondimensionalize the transport equations (4.23) and (4.24). To that end, we introduce a typical length Δx [mm], a typical velocity v_0 [mm/s], a typical bacterial concentration b_0 [cfu/ml], and a typical substrate concentration s_0 [g/ml]. Then the transport equations become

$$\frac{\partial \hat{b}}{\partial \hat{t}} + \hat{\vec{\nabla}} \cdot \hat{b}(\hat{\vec{v}} + \hat{\vec{v}}_c) = \frac{1}{\mathsf{Pe}_b} \hat{\nabla}^2 \hat{b} + \hat{Y} \hat{r_s} - \hat{k}\hat{b} \tag{2.4}$$

$$\frac{\partial \hat{s}}{\partial \hat{t}} + \hat{\vec{\nabla}} \cdot \hat{s}\hat{\vec{v}} = \frac{1}{\mathsf{Pe}_s} \hat{\nabla}^2 \hat{s} - \hat{r_s} \tag{2.5}$$

where $\hat{b} = b/b_0$, $\hat{s} = s/s_0$, $\hat{t} = tv_0/\Delta x$, $\hat{\nabla} = \Delta x \nabla$, $\hat{\vec{v}} = \vec{v}/v_0$, $\hat{\vec{v}}_c = \vec{v}_c/v_0$, $\hat{Y} = Y s_0/b_0$, $\hat{k} = k\Delta x/v_0$, $\hat{r_s} = \hat{q}\hat{s}\hat{b}/(\hat{s} + \hat{k_s})$, $\hat{k_s} = k_s/s_0$, $\hat{q} = q b_0 \Delta x/s_0 v_0$, and

$$\mathsf{Pe}_b = \frac{\Delta x v_0}{\mu}, \qquad \mathsf{Pe}_s = \frac{\Delta x v_0}{D} \tag{2.6}$$

are lattice Peclet numbers with respect to the bacteria and the substrate, respectively.

2.3.2 Lattice-Boltzmann model for chemotaxis

In lattice-Boltzmann (LB) modeling, both the bacteria and the substrate are represented by particles which live on a numerical lattice. These particles can move from the nodes of the lattice to adjacent nodes, and the particles collide and react with each other at the nodes. At each lattice node $\vec{x}_j$ and for each discrete time t_n, distribution functions

$f_{b,i}(\vec{x}_j, t_n)$ and $f_{s,i}(\vec{x}_j, t_n)$ are defined and are proportional to the number of particles that have a lattice velocity $\vec{e}_i$, which connects a lattice site to its neighboring ones.

In the SRT-LBM, the distribution functions approach local equilibrium through a single relaxation time [7]. This method has been widely implemented due to its simplicity. However, it suffers from well-known deficiencies, such as the dependence of the pore boundary locations on the viscosity, and it is prone to numerical instability [17]. By contrast, the distribution functions in the MRT-LBM approach local equilibrium through multiple relaxation times. The MRT-LBM can overcome the deficiencies of the SRT-LBM and achieve "optimal" stability by tuning the relaxation times [10].

For 3D simulations, three types of cubic lattice models that differ in the number of lattice vectors (allowed particle velocities) have been widely used: the fifteen (D3Q15), nineteen (D3Q19), and twenty-seven (D3Q27) models [46]. The D3Q15 model is more prone to numerical instability, and the D3Q27 is more computationally intensive. Therefore, we selected the D3Q19 model, which provides a balance between computational reliability and efficiency [35]. The lattice is shown by Fig. 2.1, and its lattice velocities $\vec{e}_i$ are given by

$$(\vec{e}_1, \vec{e}_2, \ldots, \vec{e}_{19}) = \begin{pmatrix} 0 & 1 & -1 & 0 & 0 & 0 & 0 & 1 & -1 & 1 & -1 & 1 & -1 & 1 & -1 & 0 & 0 & 0 & 0 \\ 0 & 0 & 0 & 1 & -1 & 0 & 0 & 1 & -1 & -1 & 1 & 0 & 0 & 0 & 0 & 1 & -1 & 1 & -1 \\ 0 & 0 & 0 & 0 & 0 & 1 & -1 & 0 & 0 & 0 & 0 & 1 & -1 & -1 & 1 & 1 & -1 & -1 & 1 \end{pmatrix}$$

The particle distributions for the different velocities $\vec{e}_i$ form a 19-dimensional vector. Scale-up is achieved by relating the particle distribution functions to the continuum-scale

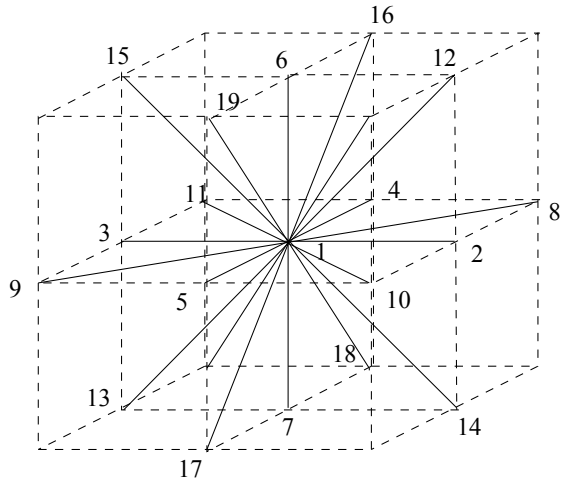

Figure 2.1: Lattice of the D3Q19 model used in our simulations

concentrations via

$$\hat{b}(\mathbf{x}_j, t_n) = \sum_{i=1}^{19} f_{b,i}(\mathbf{x}_j, t_n) \qquad \text{and} \qquad \hat{s}(\mathbf{x}_j, t_n) = \sum_{i=1}^{19} f_{s,i}(\mathbf{x}_j, t_n) \tag{2.7}$$

The MRT-LB equations for the bacteria and the substrate are given by

$$|f_b(\mathbf{x}_j + \delta\vec{e}_i, t_n + \delta)\rangle = |f_b(\mathbf{x}_j, t_n)\rangle - \mathsf{M}^{-1}\mathsf{S}_b \left[|m_b(\mathbf{x}_j, t_n)\rangle - |m_b^0(\mathbf{x}_j, t_n)\rangle\right] + |R_b(\mathbf{x}_j, t_n)\rangle \tag{2.8}$$

$$|f_s(\mathbf{x}_j + \delta\vec{e}_i, t_n + \delta)\rangle = |f_s(\mathbf{x}_j, t_n)\rangle - \mathsf{M}^{-1}\mathsf{S}_s \left[|m_s(\mathbf{x}_j, t_n)\rangle - |m_s^0(\mathbf{x}_j, t_n)\rangle\right] + |R_s(\mathbf{x}_j, t_n)\rangle \tag{2.9}$$

We used the "bra-ket" notation for the 19-dimensional column vectors, i.e.,

$$
\begin{aligned}
|f_\sigma(\mathbf{x}_j,t_n)\rangle &= (f_{\sigma,1}(\mathbf{x}_j,t_n), f_{\sigma,2}(\mathbf{x}_j,t_n),\ \cdots,\ f_{\sigma,19}(\mathbf{x}_j,t_n))^T \\
|m_\sigma(\mathbf{x}_j,t_n)\rangle &= (m_{\sigma,1}(\mathbf{x}_j,t_n), m_{\sigma,2}(\mathbf{x}_j,t_n),\ \cdots,\ m_{\sigma,19}(\mathbf{x}_j,t_n))^T \\
|m^0_\sigma(\mathbf{x}_j,t_n)\rangle &= (m^0_{\sigma,1}(\mathbf{x}_j,t_n), m^0_{\sigma,2}(\mathbf{x}_j,t_n),\ \cdots,\ m^0_{\sigma,19}(\mathbf{x}_j,t_n))^T \\
|R_\sigma(\mathbf{x}_j,t_n)\rangle &= (R_{\sigma,1}(\mathbf{x}_j,t_n), R_{\sigma,2}(\mathbf{x}_j,t_n),\ \cdots,\ R_{\sigma,19}(\mathbf{x}_j,t_n))^T,
\end{aligned}
$$

where the superscript T indicates the transposition of a row vector into a column vector, and σ denotes b or s. In Eqs. (2.8) and (3.14), the term on the left-hand-side and the first term on the right-hand-side describe travel steps, during which the particles travel with a velocity $\vec{e}_i$ from one lattice node to its adjacent lattice nodes, where δ is the dimensionless lattice spacing. The second and third terms on the right-hand-side describe collisions of particles on each lattice site. M is a 19×19 transformation matrix that allows calculating the hydrodynamic moments from the particle distribution function via $|m\rangle = \mathsf{M}|f\rangle$. In the Appendix, we show how to construct M following methods developed for fluid flow [10]. The corresponding 19 moments of $|m\rangle$ are the following: the mass density ($m_1 = C$), the kinetic energy ($m_2 = e$), the kinetic energy squared ($m_3 = \psi = e^2$), the momentum ($m_{4,6,8} = j_{x,y,z}$), the energy flux ($m_{5,7,9} = q_{x,y,z}$), the symmetric traceless viscous stress tensor ($m_{10} = 3p_{xx}$, $m_{11} = 3\pi_{xx}$, $m_{12} = p_{ww} = p_{yy}$ - p_{zz}, $m_{13} = \pi_{ww}$, $m_{14,15,16} = p_{xy,yz,zx}$, where $p_{xx} + p_{yy} + p_{zz} = 0$, π_{xx} is a function of free parameter w_{xx}, and π_{ww} is a function of p_{ww}), and the antisymmetric third-order moment ($m_{17,18,19} = m_{x,y,z}$). The moment vector is arranged in the following order:

$$|m\rangle = (C, e, \psi, j_x, q_x, j_y, q_y, j_z, q_z, 3p_{xx}, 3\pi_{xx}, p_{ww}, \pi_{ww}, p_{xy}, p_{yz}, p_{xz}, m_x, m_y, m_z)^T$$

Accordingly, appropriate equilibrium moments must be specified in order for a LB model to represent a given transport phenomenon. We define

$$\begin{aligned} |m_b^0\rangle &= (\hat{b}, -1.5\hat{b}, -\hat{b}, \hat{b}(\hat{v}_x + \hat{v}_{cx}), -\tfrac{7}{3}\hat{b}(\hat{v}_x + \hat{v}_{cx}), \hat{b}(\hat{v}_y + \hat{v}_{cy}), -\tfrac{7}{3}\hat{b}(\hat{v}_y + \hat{v}_{cy}), \\ &\quad \hat{b}(\hat{v}_z + \hat{v}_{cz}), -\tfrac{7}{3}\hat{b}(\hat{v}_z + \hat{v}_{cz}), 0, 0, 0, 0, 0, 0, 0, 0, 0, 0)^T \end{aligned}$$

$$|m_s^0\rangle = (\hat{s}, -1.5\hat{s}, -\hat{s}, \hat{s}\hat{v}_x, -\tfrac{7}{3}\hat{s}\hat{v}_x, \hat{s}\hat{v}_y, -\tfrac{7}{3}\hat{s}\hat{v}_y, \hat{s}\hat{v}_z, -\tfrac{7}{3}\hat{s}\hat{v}_z, 0, 0, 0, 0, 0, 0, 0, 0, 0, 0)^T$$

where $\hat{v}_{x,y,z}$ and $\hat{v}_{cx,cy,cz}$ are the dimensionless convective velocity and the dimensionless chemotactic velocity in the three Cartesian coordinate directions, respectively. We explain how to determine the $|m_b^{(0)}\rangle$ and $|m_s^{(0)}\rangle$ in the Appendix.

The S_b and S_s in Eqs. (2.8) and (3.14) are diagonal 19×19 collision matrices, the elements of which can be chosen to match macroscopic diffusive behavior and achieve optimal solutions. In our simulations, we choose

$$\begin{aligned} \mathsf{S}_b &= diag(0, 1, 1, \tau_b, 1, \tau_b, 1, \tau_b, 1, 1, 1, 1, 1, 1, 1, 1, 1, 1, 1) \\ \mathsf{S}_s &= diag(0, 1, 1, \tau_s, 1, \tau_s, 1, \tau_s, 1, 1, 1, 1, 1, 1, 1, 1, 1, 1, 1), \end{aligned}$$

where τ_b and τ_s are relaxation times, which are dependent of the diffusivities of the bacteria

and the substrate, respectively,

$$\tau_b = \frac{1}{2} + \frac{2}{\delta \mathsf{Pe}_b}, \qquad \tau_s = \frac{1}{2} + \frac{2}{\delta \mathsf{Pe}_s} \tag{2.10}$$

The $|R_b\rangle$ and $|R_s\rangle$ in Eqs. (2.8) and (3.14) represent mass gain or loss due to microbial reactions, that is, the growth and decay of the bacteria and the consumption of the substrate in the present study,

$$R_{b,i} = \delta Y \frac{q_s \Delta x}{v_0} \frac{s_0 \hat{s}}{s_0 \hat{s} + k_s} f_{b,i} - k \frac{\Delta x}{v_0} f_{b,i}, \qquad R_{s,i} = \delta \frac{q_s \Delta x b_0 \hat{b}}{v_0 (s_0 \hat{s} + k_s)} f_{s,i} \tag{2.11}$$

When the the lattice spacing δ approaches zero, the LB equations (2.8) and (3.14) approach the concentration fields of the continuum-scale equations (4.26) and (4.27). We present the elaborate derivation in the Appendix. In applications, one usually chooses $\delta = 1$, which means that the dimensional lattice spacing equals the typical length Δx. Consequently, the LB equations become

$$|f_b(\mathbf{x}_j + \vec{e}_i, t_n + 1)\rangle = |f_b(\mathbf{x}_j, t_n)\rangle - \mathsf{M}^{-1}\mathsf{S}_b \left[|m_b(\mathbf{x}_j, t_n)\rangle - |m_b^0(\mathbf{x}_j, t_n)\rangle\right] + |R_b(\mathbf{x}_j, t_n)\rangle \tag{2.12}$$

$$|f_s(\mathbf{x}_j + \vec{e}_i, t_n + 1)\rangle = |f_s(\mathbf{x}_j, t_n)\rangle - \mathsf{M}^{-1}\mathsf{S}_s \left[|m_s(\mathbf{x}_j, t_n)\rangle - |m_s^0(\mathbf{x}_j, t_n)\rangle\right] + |R_s(\mathbf{x}_j, t_n)\rangle \tag{2.13}$$

We validated the MRT-LBM by comparing simulation results with experiments by Pedit et al. [45]. In these experiments, capillary tubes, which contained a buffer solution

with an initially uniformly distributed chemoattractant, were dipped into a reservoir containing a bacterial suspension. Similar to the Adler [1]'s experiment, bacteria entered the tube to form a traveling band. Figure 2.2 shows that the simulation results agree well with the experiments, in which the number of cells that accumulated in the tube was measured as a function of time. More details about the validation procedure can be found in Long and Hilpert [29], who used the same experiments to validate their SRT model.

We also compared simulation results between our MRT model and Long and Hilpert [29]'s SRT model for different spatial resolutions Δx. In order to save CPU time, we chose a one-dimensional (1D) domain with length 20mm for simulations. A slug of the bacteria with length 1 mm was initially injected from the left into this domain, and the substrate was uniformly distributed. The bacteria consumed the substrate and formed a band, which moved toward the higher substrate concentration. Figure 2.3 shows the difference between the average bacterial traveling distance (first moment of concentration profile) simulated by our MRT model and by Long and Hilpert [29]'s SRT model for a fixed time and different spatial resolutions. The MRT-LBM and SRT-LBM converge to the same average traveling distance, $\bar{x} = 8.45$ mm, as we refine the grid. However, the MRT model can attain a better numerical stability than the corresponding SRT model (with the same lattice) as will be described below.

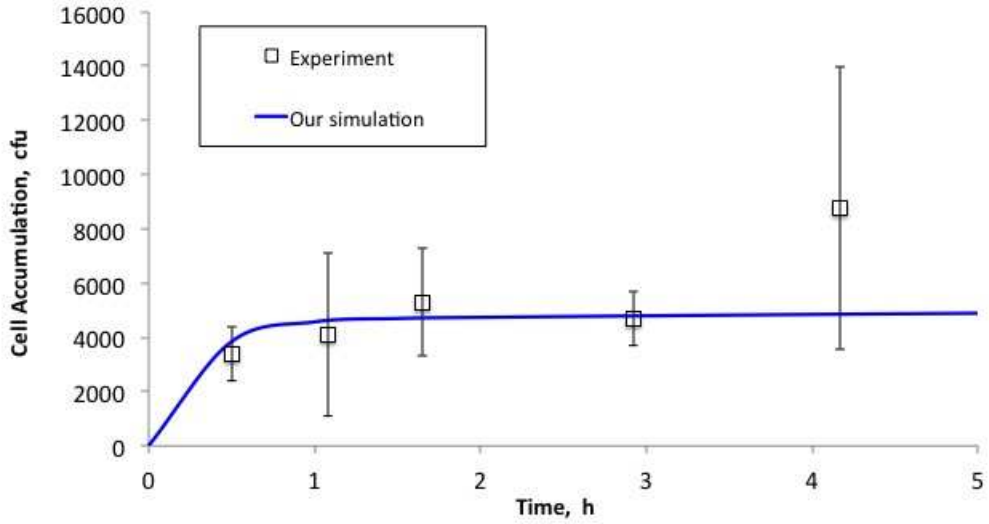

Figure 2.2: Comparisons of our MRT simulations with experiments [45]

2.4 Simulation results

2.4.1 Effects of substrate diffusion on bacterial bands

All simulations presented in this work are based on the parameter values shown in Table 4.2. Change of parameter values will be highlighted in the text. The b_0 and s_0 in Table 4.2 are initial concentrations of the bacteria and the substrate, respectively, and are used to nondimensionalize Eqs. (4.23) and (4.24). The bacterial swimming speed v_s is used as the typical velocity for nondimensionalization. Note that the MRT-LBM can simulate microbial processes with production and death, although no bacterial growth and decay occurs in this study.

Bacterial chemotaxis was first simulated in a 1D region with length 100 mm. The spatial resolution was $\Delta x = 0.04$ mm, and it was used as the typical length for nondi-

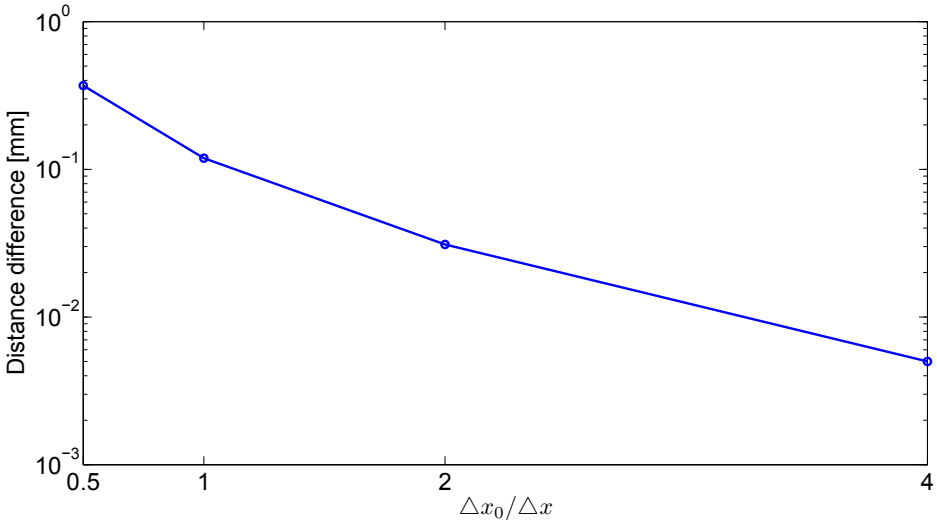

Figure 2.3: Difference between averaged bacterial traveling distance simulated by our MRT model and by Long and Hilpert [29]'s SRT model after 4.6 hrs under different spatial resolutions Δx ($\Delta x_0 = 0.04$ mm). The averaged traveling distance is $\bar{x} = 8.45$ mm.

Table 2.1: Parameter values for the chemotactic system that we simulated are based on the work by Marx and Aitken [33] and Pedit et al. [45].

Symbol	Value
b_0	4×10^6 cfu/ml
s_0	2.8×10^{-2} g/ml
D	7.5×10^{-6} cm^2/s
μ	3.2×10^{-7} cm^2/s
q	7.9×10^{-13} g/cfu/s
Y	0
k	0
K_d	2.1×10^{-3} g/ml
k_s	1.3×10^{-4} g/ml
χ_0	1.8×10^{-5} cm^2/s
v_s	4.8×10^{-3} cm/s

mensionalization. In the beginning, the substrate was uniformly distributed, and a 10 mm-long slug of bacteria was introduced on the left side of the domain. A no-flux boundary condition was prescribed at $x = 0$. The evolution of the bacteria was simulated for

two different diffusion coefficients D. Fig. 2.4 shows that the bacterial bands are much narrower and move more quickly for $D = 7.5 \times 10^{-7}$ cm^2/s than for $D = 7.5 \times 10^{-6}$ cm^2/s. The smaller D results in a larger gradient of substrate concentration and thus a larger chemotactic velocity as well as a faster band speed.

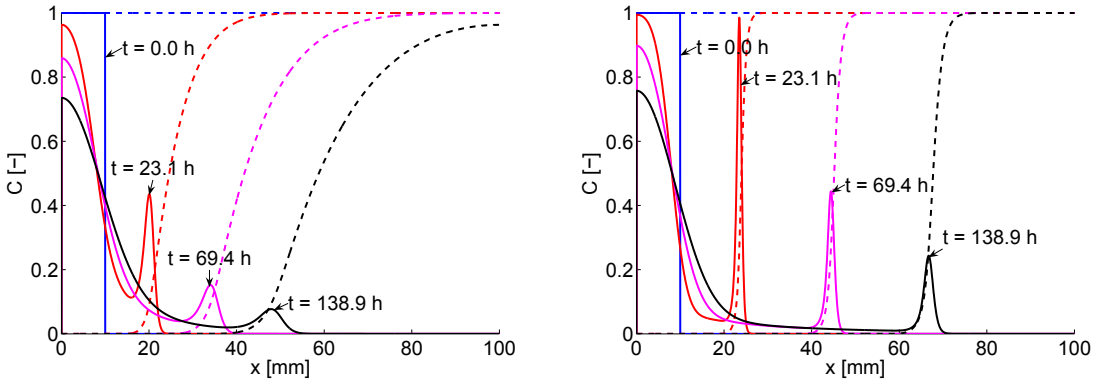

(a) $D = 7.5 \times 10^{-6}$ cm^2/s (b) $D = 7.5 \times 10^{-7}$ cm^2/s

Figure 2.4: Concentration profiles normalized by the initial concentrations as a function of time for different substrate diffusion coefficients: (a) $D = 7.5 \times 10^{-6}$ cm^2/s; and (b) $D = 7.5 \times 10^{-7}$ cm^2/s. Solid lines denote the bacteria and dash lines denote the substrate. Different colors stand for different moments in time.

For the case of negligible substrate diffusion, Long and Hilpert [28] derived that the necessary and sufficient condition for the presence of bacterial bands was $\lambda > 1$ where

$$\lambda = \frac{\chi_0}{\mu} \tag{2.14}$$

is a dimensionless number which compares the biased bacterial movement due to chemotaxis with the diffusion-like movement due to random motility. In this paper, we determine the critical λ value, above which a bacterial band is formed from an initial bacterial slug,

as a function of the substrate diffusion coefficient D. We varied D by four orders of magnitude. As shown in Table 2.2, the critical λ decreases and approaches one as D decreases. Therefore bacterial bands form more easily in a system with less substrate diffusion.

Table 2.2: The critical λ values for forming bacterial bands for different substrate diffusion coefficients D.

D (cm^2/s)	7.5×10^{-5}	7.5×10^{-6}	7.5×10^{-7}	7.5×10^{-8}
λ	50.6	14.1	5.63	2.25

2.4.2 Effects of initial bacterial concentration and uniform flow on spherical bacterial bands

We simulated the formation of bands due to injection of a ball of bacteria with radius 1.5 mm into a cuboid domain with a size 45×30×30 mm^3. Flow was potentially applied along the longest dimension of this domain. The ball was centered along the longitudinal axis. The substrate was initially uniformly distributed. Periodic boundary conditions were applied. The spatial resolution was $\Delta x = 0.2$ mm. First, we studied stagnant flow and used the initial bacterial concentration b_0 from Table 4.2. Fig. 2.5a illustrates that no bacterial band is observed and that the bacteria spread out in a diffusion-like manner. When using a higher initial bacterial concentration, $b_0 = 1 \times 10^8$ cfu/ml, the bacteria form an expanding shell (or band) as shown in Fig. 2.5b. The peak concentration of the band decreases quickly since the bacteria diffuse radially both inward and outward.

Figure 2.5c presents the position of the right bacterial peak in Fig. 2.5b. The results show that the traveling bacterial band moves outward while decreasing its speed and eventually disappearing after 3.5 hrs, because the replenishment of the substrate from outside of the bacterial shell decreases the gradient of the substrate concentration quickly. Eventually, diffusion becomes the sole transport mechanism for the bacteria, whereas chemotaxis has no effect. Therefore, a sufficiently high initial number of bacteria is necessary for forming a bacterial shell, and this bacterial shell caused by chemotaxis in a 3D geometry disappears more quickly than 1D.

We also considered uniform fluid flow along the longitudinal direction with a speed 4.6 $\times 10^{-5}$ cm/s. Figure 2.6 shows that the same concentration distributions are observed as for the stagnant flow, except that the bacteria and the substrate move downstream along with the flow. Thus the uniform velocity does not affect the formation and shape of bacterial bands. This behavior is also expected according to the Galilean invariance of the governing equations (4.23) and (4.24) for a uniform pore-water velocity $\vec{v}$.

2.4.3 Effects of hydrodynamic dispersion on bacterial bands

In this section, we examine the impact of hydrodynamic dispersion on bacterial bands in a round tube with radius $R = 0.05$ mm and length $L = 100$ mm. Periodic boundary conditions were applied. The spatial resolution was $\Delta x = 0.01$ mm. As illustrated in Fig. 2.7, a 10 mm-long bacterial slug was injected into the tube in which the substrate was uniformly distributed. The slug occupied the cylindrical region defined by 30 mm $\leq x \leq$

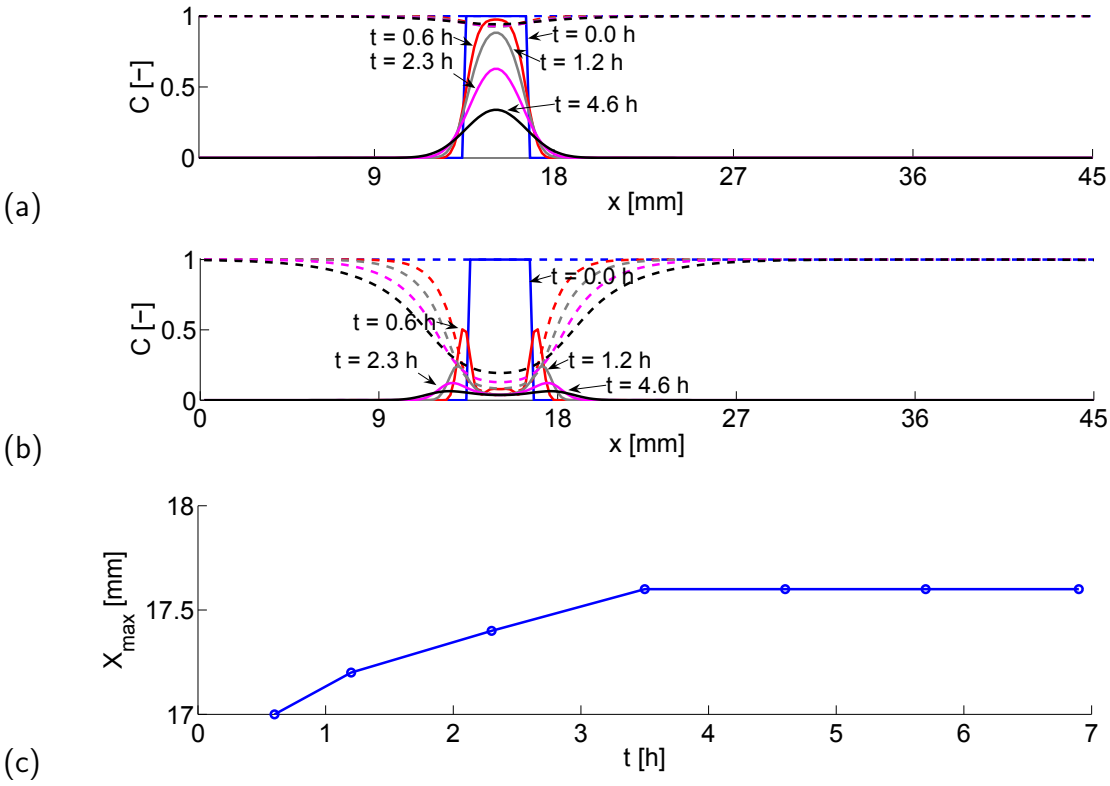

Figure 2.5: Simulations of 3D traveling bands originating from a bacterial ball with different initial bacterial concentrations. The fluid is stagnant. (a) and (b): Normalized concentration profiles along the longitudinal axis for $b_0 = 4 \times 10^6$ cfu/ml and $b_0 = 1 \times 10^8$ cfu/ml, respectively. Solid lines denote the bacteria and dash lines denote the substrate. The same color stands for the same time moment for the bacteria and the substrate. (c) Positions of the right bacterial peak shown in (b) as a function of time.

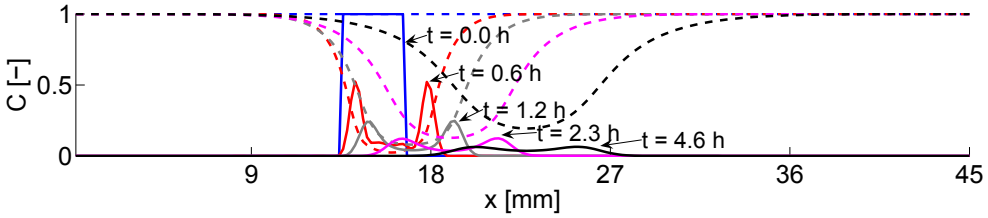

Figure 2.6: Normalized concentration profiles along the longitudinal axis for $b_0 = 1 \times 10^8$ cfu/ml. The fluid flows with a speed 4.6 $\times 10^{-5}$ cm/s. Solid lines denote the bacteria and dash lines denote the substrate. The same color stands for the same time moment for the bacteria and the substrate.

40 mm. Five cases with different Peclet numbers, Pe $= 2Rv/\mu$, were simulated by varying the pore-water velocity v (see Table 2.3).

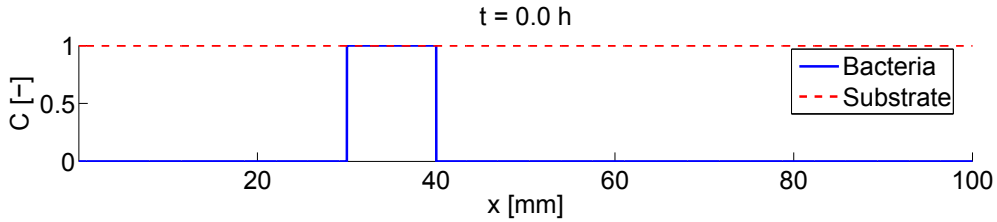

Figure 2.7: Initial normalized concentration profiles for the bacteria and the substrate along the centerline of the tube in which a parabolic velocity profile is established.

Figure 2.8 shows concentration profiles for the bacteria and the substrate for Pe $= 0$, 0.1 and 1, the Peclet numbers for which two traveling bacterial bands could be observed. Here we focus our discussion on the bacterial bands caused by chemotaxis and pay less attention to the band that travels downstream due to convection and diffusion. The latter band occurs no matter whether the bacteria perform chemotaxis or not and no matter how strong the dispersion is. For Pe $= 0$, two symmetric bacterial bands occur. They consume the substrate and move toward regions with high substrate concentration. When $t = 23.1$ hrs, the measured speed of the band is $c_{meas} = 1.20 \times 10^{-5}$ cm/s, which agrees reasonably well with an analytical result derived by Long and Hilpert [28]:

$$c_{ana} = \frac{qN_b}{\phi(s_0 - s(\xi_{min}) + k_s \ln \frac{s_0}{s(\xi_{min})})} = 1.77 \times 10^{-5} \text{ cm/s} \qquad (2.15)$$

where ξ_{min} is the location of the local minimum of the bacterial concentration, N_b is the number of bacteria per cross-sectional area inside the band, and ϕ is the tortuosity (which

equals one in a bulk fluid). For Pe $= 0.1$, although one might expect all bacteria to move downstream along with the flow, two approximately symmetrical bacterial bands form and move downstream and upstream, respectively. For Pe $= 1$, both bacterial bands move downstream because of the convection. The shapes of bacterial bands are similar for the small Peclet numbers, and the peak concentration values of these bands decrease with time.

For Pe $= 10$, two bands initially form and propagate downstream. The downstream band is much more populated than the upstream one, which disappears soon due to hydrodynamic dispersion (Fig. 2.9a). For comparison, we also simulated transport of non-chemotactic bacteria under otherwise the same conditions. Fig. 2.9b shows that only one band advects downstream with the average fluid velocity, which is smaller than the velocity of the downstream band in case of chemotaxis.

For Pe $= 30$, no bacterial band is formed by chemotaxis (see Fig. 2.10). Both the bacteria and the substrate undergo convective transport. A sole bacterial band propagates downstream with the average pore-water velocity and spreads out quickly due to hydrodynamic dispersion. The effective diffusion coefficient in the tube can be estimated by Taylor dispersion theory, $\mu_{eff} = \mu\left(1 + \mathrm{Pe}^2/192\right)$. When the Peclet number is large, the impact of chemotaxis, which does not depend on Pe, is negligible when compared with the effect of hydrodynamic dispersion, which increases with the square of Pe.

We analyzed the above findings by generalizing the dimensionless number λ according to Eq. (3.9), which has been developed for stagnant flow conditions. We replace the μ

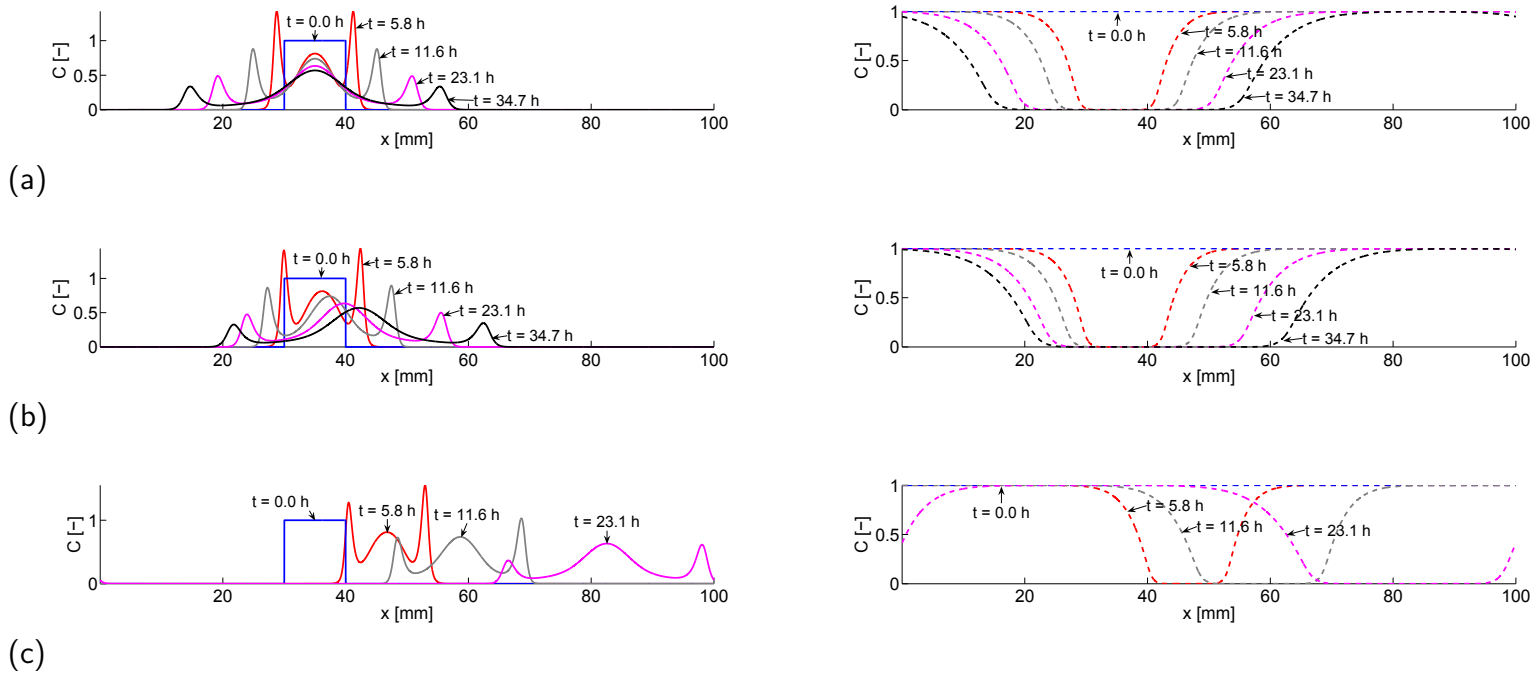

Figure 2.8: Concentration profiles of the bacteria (left) and substrate (right) along the centerline of the tube as a function of time for different Peclet numbers. Concentrations are normalized by the initial concentrations. (a) Pe = 0, (b) Pe = 0.1, and (c) Pe = 1.

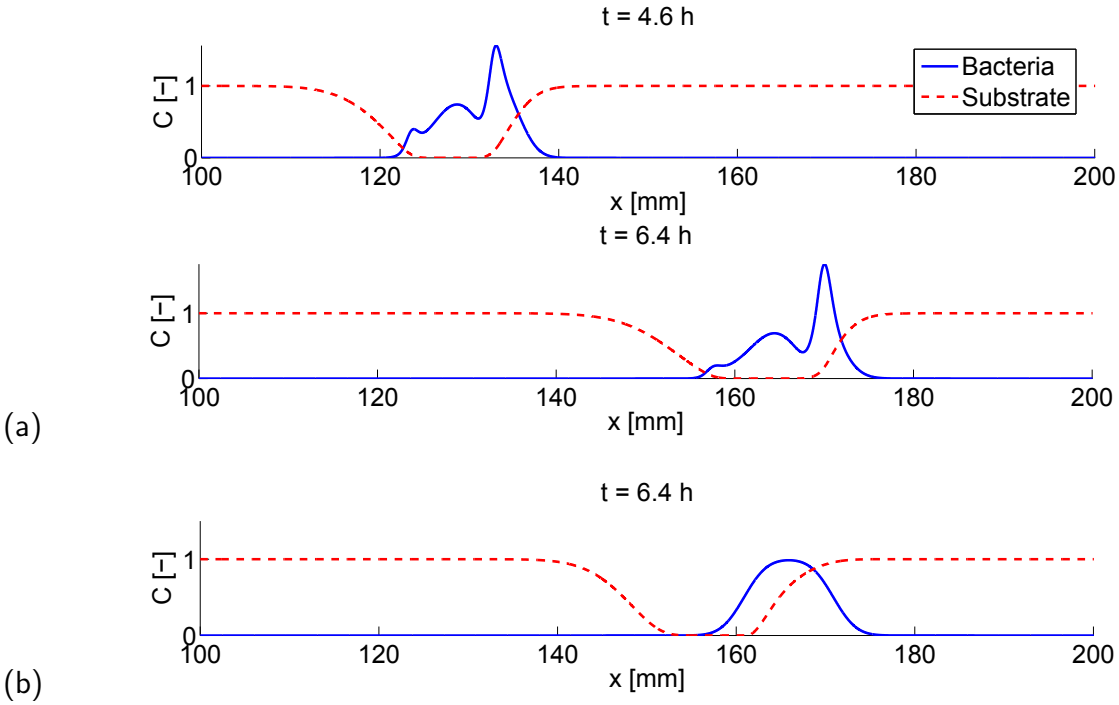

Figure 2.9: (a) Concentration profiles (normalized by the initial concentrations) along the centerline of the tube after the chemotactic bacteria are injected into the domain for times $t = 4.6$ hrs and 6.4 hrs. (b) Profiles if non-chemotactic bacteria are injected into the domain for $t = 6.4$ hrs. In both simulations, Pe $= 10$.

by the effective diffusion coefficient μ_{eff}, which accounts for both random motility and hydrodynamic dispersion, to define λ as follows:

$$\lambda = \frac{\chi_0}{\mu_{eff}} \tag{2.16}$$

This dimensionless number compares the biased movement of bacteria due to chemotaxis with the diffusion-like movement of bacteria due to random motility and hydrodynamic dispersion. Table 2.3 shows the λ-values for different Peclet numbers. Fig. 2.11 presents the corresponding shapes of bacterial bands at $t = 11.6$ hrs. As λ decreases, that is, as

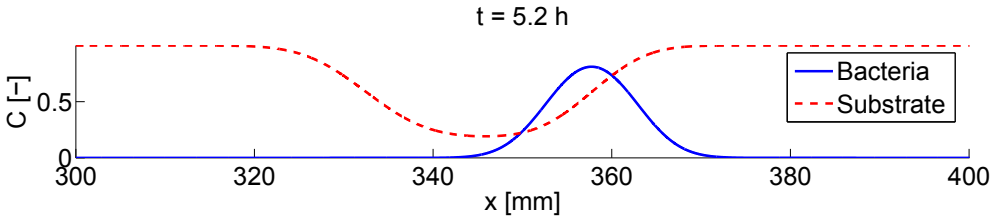

Figure 2.10: Concentration profiles (normalized by the initial concentrations) along the centerline of the tube at t = 5.2 hrs when Pe = 30.

hydrodynamic dispersion increases, the difference between the downstream and upstream bands increases. The downstream band first disappears as λ decreases; eventually both bands disappear. In the simulations presented here, the bacteria form two approximately symmetric bands when $\lambda \geq 56$, one band when $\lambda = 37$, and no band when $\lambda \leq 10$. Therefore, λ can be used to predict the formation and shape of bacterial bands.

Table 2.3: The λ value defined in Eq. (2.16) varies with the Peclet number and predicts the formation of bacterial bands caused by chemotaxis.

v (cm/s)	0	3.2×10^{-6}	3.2×10^{-5}	3.2×10^{-4}	9.6×10^{-4}
Pe	0	0.1	1	10	30
μ_{eff} (cm^2/s)	3.20×10^{-7}	3.20×10^{-7}	3.22×10^{-7}	4.87×10^{-7}	1.82×10^{-6}
λ	56.3	56.3	56	37	10
				Traveling bands $\longleftarrow$ |	

We also simulated the transport and fate of the bacteria and the substrate for larger Peclet numbers by using both MRT model and the corresponding SRT model with the same lattice. We found that both the MRT and SRT models became numerical unstable when Pe exceeds 32. However, the MRT model achieved stable solution even though Pe equals 35 when we set the collision matrices S_b as $diag(0, 0.2, 0.2, \tau_b, 1, \tau_b, 1, \tau_b, 1, 0.2, 0.2, 0.2, 0.2, 0.2, 0.2, 0.2, 0.2, 0.2, 0.2)$ and S_s as $diag(0, 0.2, 0.2, \tau_s, 1, \tau_s, 1, \tau_s, 1, 0.2, 0.2, 0.2, 0.2, 0.2, 0.2, 0.2, 0.2, 0.2, 0.2)$. Therefore, the MRT model can attain a better numerical

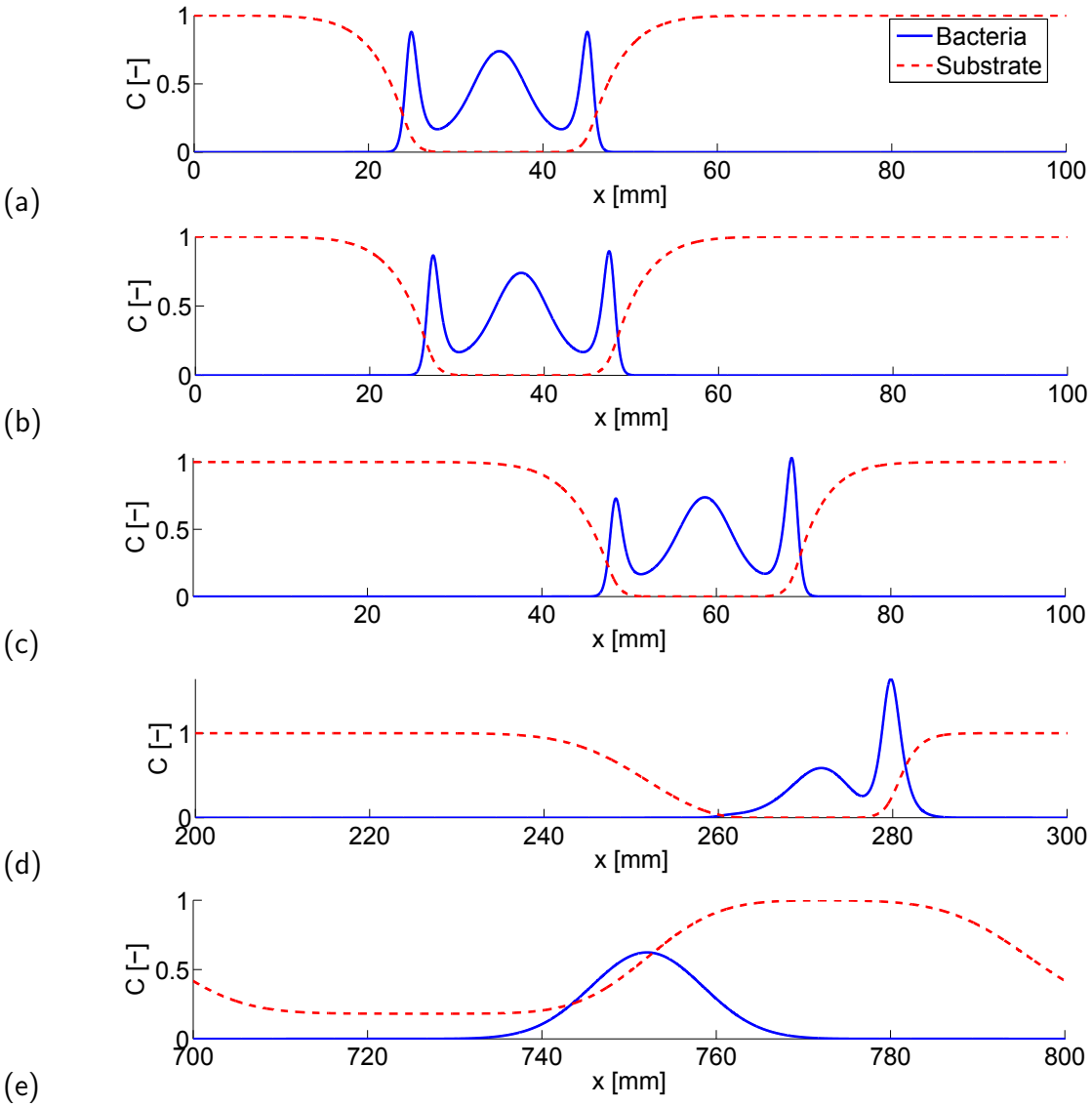

Figure 2.11: Concentration profiles (normalized by initial concentrations) along the centerline of the tube at $t = 11.6$ hrs for different Peclet numbers: (a) Pe $= 0$; (b) Pe $= 0.1$; (c) Pe $= 1$; (d) Pe $= 10$; and (e) Pe $= 30$.

stability than the corresponding SRT model if we choose appropriate collision matrices.

2.4.4 Bacterial chemotaxis in two-dimensional porous media

In order to explore the effects of hydrodynamic dispersion on bacterial bands in topologically more complex porous media, we performed simulations in a quasi-2D porous medium that represents a microfluidic device used to examine bacterial transport in porous media [51]. The device contained a square array of cylindrical grains of diameter 0.3 mm and pore-throat size 0.05 mm. The length and width of the porous medium domain were 18.2 mm and 6.12 mm, respectively. An injection port, where no grains were present, was located 2.45 mm downstream from the left primary inlet of the flow cell (see Fig. 2.12). The porosity of this device was $\epsilon = 0.42$. In our simulations, the bacteria were initially injected into the micromodel through the injection port, and the substrate was uniformly distributed.

We studied bacterial migration and substrate consumption under different initial bacterial concentrations and Darcy velocities w. As a control, we also performed simulations for which we assumed that the bacteria were not chemotactic. Table 2.4 presents the simulation schemes. Fig. 2.12 show the simulated concentration fields of the bacteria (left) and the substrate (right) after 0.26 hrs for five cases. Substrate removal is strongly correlated to the concentration and migration of the bacteria, which in turn depend on microorganisms survival and substrate bioavailability. Fig. 2.12a shows that no bacterial band is formed and little substrate is degraded for the base case (Case 1). In Case 2, a larger initial bacterial concentration, $b_0 = 4 \times 10^8$ cfu/ml, is used. Fig. 2.12b shows that a bacterial ring is formed which moves outward to regions with high substrate concentra-

tion due to chemotaxis. The results are consistent with the conclusion drawn from the simulations of spherical bacterial band that sufficient bacteria are necessary for generating a band by chemotaxis. This larger initial bacterial concentration is used in all following cases such that the initial bacterial concentration is not a limiting factor for forming a band. Case 3 uses a smaller Darcy velocity, while Case 4 uses a larger one. Fig. 2.12c shows that the bacteria form a ring when the velocity is small. In contrast to Case 2, which used an intermediate Darcy velocity, a portion of bacteria inside the ring moves upstream in Case 3, that is, the population-scale chemotactic velocity v_c exceeds the flow velocity. When the flow velocity is larger (Case 4), no bacterial band is observed due to the increased hydrodynamic dispersion and the bacteria are advected downstream along with the flow, which are shown in Fig. 2.12d. We also simulated Case 4, except that we assumed the bacteria to be non-chemotactic ($\chi_0 = 0$). Then no band was observed (results not shown). Therefore in Case 4, chemotaxis did not obviously promote the removal of the substrate due to the strong hydrodynamic dispersion. In Case 5, all parameters are the same as in Case 2 except that the bacteria is non-chemotactic ($\chi_0 = 0$). Fig. 2.12e shows that no band is observed and the bacteria move around due to convection, diffusion, and dispersion. Both the size of the domain in which substrate has been degraded and the amount of removed substrate are smaller in Case 5 than in Case 2. The results demonstrate that bacterial chemotaxis can result in traveling bands when the initial bacterial concentration is sufficiently high and hydrodynamic dispersion is weak. These bands can significantly improve substrate consumption (biodegradation).

Table 2.4: Cases simulated in the 2D porous medium. We varied the initial bacterial concentration b_0, the Darcy velocity w, and the chemotactic sensitivity coefficient χ_0.

Case	b_0 (cfu/ml)	w (cm/day)	χ_0 (cm^2/s)	λ
1	4.0×10^6	4	1.8×10^{-5}	
2	4.0×10^8	4	1.8×10^{-5}	25
3	4.0×10^8	0.4	1.8×10^{-5}	70
4	4.0×10^8	20	1.8×10^{-5}	6.3
5	4.0×10^8	4	0	

We also calculated λ values for cases 2-4 in Table 2.4 when $b_0 = 4.0 \times 10^8$ cfu/ml. Singh and Olson [51] measured the apparent transversal dispersivity and the tortuosity of the bacteria: $\alpha_T = 0.0048$ mm and $\phi = 1.57$. Unfortunately the longitudinal dispersivity was not measured. We empirically assume that the apparent longitudinal dispersivity, α_L, is ten-fold of the apparent transversal dispersivity such that $\alpha_L = 0.0048$ cm, because analysis of solute dispersion experiments in porous media suggests that $0.01\ \alpha_L < \alpha_T < 0.2\ \alpha_L$ [31]. We can therefore estimate an effective dispersion coefficient of the bacteria: $\mu_{eff} = \mu/\phi + \alpha_L \overline{v}$, where $\overline{v}$ is the average pore-water velocity ($\overline{v} = w/\epsilon$). Figure 2.12 illustrates that the bacterial chemotaxis strengthens with an increase in λ and results in a band when $\lambda \geq 25$.

2.5 Summary and discussion

Traveling bacterial bands that form due to chemotaxis are capable of improving the removal of contaminants in porous media even though flow occurs. The present paper investigates the effects of different factors on the formation, shape, and propagation of

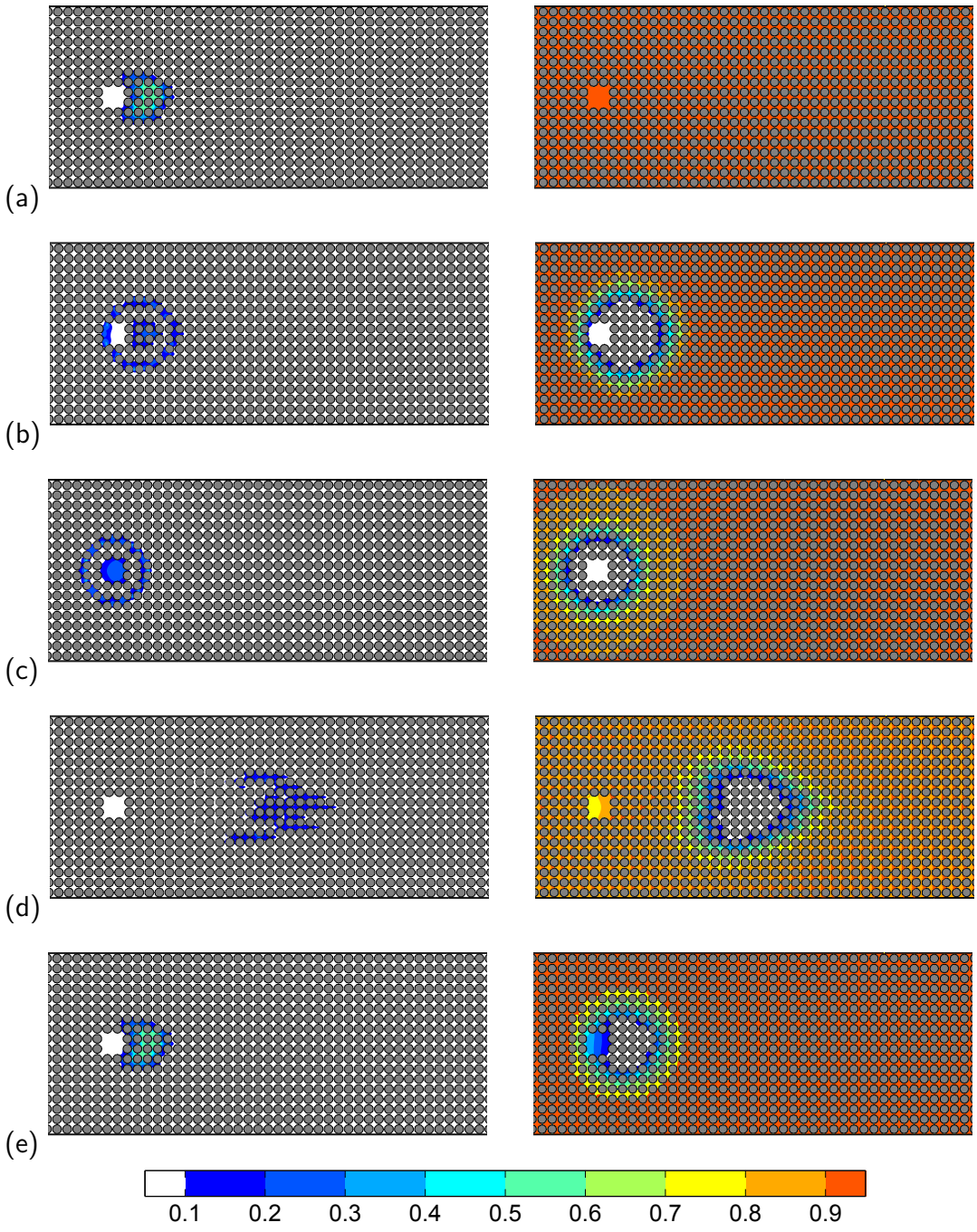

Figure 2.12: Concentration distributions of the bacteria (left) and the substrate (right) normalized by the initial concentrations 0.26 hrs after the bacteria were injected in the hole for different cases: (a) Case 1, (b) Case 2, (c) Case 3, (d) Case 4, and (e) Case 5.

such bands.

(1) A small substrate diffusion coefficient is necessary to allow for the formation of bacterial bands. A large diffusion coefficient leads to a small gradient in substrate concentration as well as to a small chemotactic velocity. As a result, the diffusion-like motion of the bacteria due to their random motility will overcome the biased motion due to chemotaxis, and therefore no band forms.

(2) A sufficiently high initial number of bacteria is required to form bacterial bands. When the initial bacterial concentration is too small, the metabolism-generated gradient of substrate concentration is not large enough to create bacterial bands. Therefore, it is necessary to inject enough bacteria when contaminant degradation via bacterial bands is sought.

(3) The spatial dimensionality of the bands significantly affects their fate. Spherical bacterial bands stop moving and disappear more quickly than 1D bands, because the bacteria are diluted more quickly as a band/shell expands outward and because metabolism-generated gradients in substrate concentration are weakened due to increased substrate replenishment in the 3D geometry.

(4) A uniform flow velocity has no impact on the formation and shape of bacterial bands while shear flow does. For laminar shear flow in a round tube, one can observe the following trends: For stagnant flow two symmetric bands form. For a nonzero but sufficiently small Peclet number, one can still observe two distinct traveling bands. However, for a further increase in the Peclet number, only the downstream band survives. When

the Peclet number becomes too large, hydrodynamic dispersion will overcome chemotaxis and no band forms.

(5) Bacterial bands move both upstream and downstream when the Darcy velocity in porous media is small, but they disappear when the Darcy velocity becomes large. The comparison between simulations with chemotactic and non-chemotactic bacteria suggests that bacterial chemotaxis is able to improve the removal of contaminants.

(6) The ratio of the chemotactic sensitivity coefficient to the effective diffusion coefficient of the bacteria, λ, can be used to predict the formation and shape of bacterial bands. Band formation is observed when λ exceeds a critical value that is dependent of the diffusivity of the substrate and the spatial dimensionality of the band.

(7) When seeking to enhance contaminant biodegradation through bacterial chemotaxis, we need to ensure that the diffusivity of the contaminant is small, the initial bacteria concentration is sufficiently high, and hydrodynamic dispersion is weak.

(8) The MRT-LBM can attain a better numerical stability than the corresponding SRT-LBM, which allows the MRT model to be applied to a wider range of reactive transport problems in subsurface environments; however, the stability of the MRT-LBM is dependent of the exact parameterization of the collision matrix. Moreover, although Pan et al. [41] reported that the MRT model for fluid flow used about 10 to 20% more CPU time than the SRT model, our MRT method uses about 10% less CPU time than the SRT method. A possible explanation is that computing the equilibrium moments in our MRT model requires less CPU time than in the MRT model for fluid flow, because

our equilibrium moment vector contains more zero elements, which do not need to be computed. Therefore, we recommend using the MRT method.

(9) In our simulations, the bacteria neither grow nor decay, therefore no net production occurs. However, growth and death significantly influence the removal efficiency of contaminants. Yan et al. [58] studied the coupled effects of bacterial growth and chemotaxis on bacterial migration and contaminant biodegradation. The interactions between growth and chemotaxis are capable of significantly accelerating the removal of contaminants.

(10) Our study can also be linked to studies on chemotaxis in turbulent flows. Fenchel [13] stated that bacterial bands cannot be observed in oceans due to turbulent mixing. Taylor and Stocker [52], however, showed in simulations that weak turbulence can be beneficial to chemotactic bacteria, because the turbulence stirs around the chemoattractant which then becomes more available to the bacteria. Since turbulent mixing is to some degree similar to mixing in porous media through hydrodynamic dispersion, it would be interesting to examine the effects of the substrate diffusion coefficient and initial bacterial concentration on chemotaxis and in particular on traveling bacterial bands in turbulent flows.

2.6 Appendix A: Chapman-Enskog expansion

Here we present the elaborate derivation that shows the LB equations (2.8) and (3.14) approximate solutions to the continuum-scale equations (4.26) and (4.27) via a Chapman-Enskog expansion [34]. To simplify the notation, we first consider a generic reactive and

chemotactic species that could represent either bacteria or substrate. For the special case of a substrate, $\hat{\vec{v}}_c = 0$ is used. We also set the reaction terms to zero, $R_{b,s} = 0$. The case of $R_{b,s} \neq 0$ can be dealt with as described by Hilpert [19].

The generic MRT-LB equation can be written as

$$|f(\mathbf{x_j} + \delta\vec{e}_i, t_n + \delta)\rangle = |f(\mathbf{x_j}, t_n)\rangle - \Omega\left[|f(\mathbf{x_j}, t_n)\rangle - |f^{(0)}(\mathbf{x_j}, t_n)\rangle\right] \tag{2.17}$$

where Ω is the collision matrix in particle space. In order to recover the MRT-LB equations (2.8) and (3.14), one just needs to insert the identity matrix $\mathsf{M}^{-1}\mathsf{M}$ behind Ω, and then obtains

$$|f(\mathbf{x_j} + \delta\vec{e}_i, t_n + \delta)\rangle = |f(\mathbf{x_j}, t_n)\rangle - \mathsf{M}^{-1}\mathsf{S}\left[|m(\mathbf{x_j}, t_n)\rangle - |m^{(0)}(\mathbf{x_j}, t_n)\rangle\right] \tag{2.18}$$

where $\mathsf{S} = \mathsf{M}\Omega\mathsf{M}^{-1}$ is the collision matrix in moment space. This matrix is constructed to be diagonal,

$$\mathsf{S} = diag(s_1, s_2, s_3, s_4, s_5, s_6, s_7, s_8, s_9, s_{10}, s_{11}, s_{12}, s_{13}, s_{14}, s_{15}, s_{16}, s_{17}, s_{18}, s_{19})$$

In order to relate Eq. (2.17) to a macroscopic equation, we apply a Taylor-series

expansion to the particle distribution function f,

$$f_i(\vec{x}+\vec{e}_i\delta, t+\delta) - f_i(\vec{x},t) = \sum_{n=1}^{\infty} \frac{\delta^n}{n!} \left[\vec{e}_i \cdot \vec{\nabla} + \frac{\partial}{\partial t}\right]^n f_i(\vec{x},t) \tag{2.19}$$

and further expand the particle distribution function

$$f_i = \sum_{n=0}^{\infty} \delta^n f_i^{(n)} \tag{2.20}$$

and the time derivative

$$\frac{\partial}{\partial t} = \sum_{n=0}^{\infty} \delta^n \frac{\partial_n}{\partial t} \tag{2.21}$$

We ensure that the expansion conserves mass locally by requiring that

$$\sum_{i=1}^{N} f_i^{(n)} = C^{(n)} = \begin{cases} C & \text{for} \quad n=0 \\ 0 & \text{for} \quad n>0 \end{cases} \tag{2.22}$$

where C is the dimensionless concentration of the bacteria or substrate, and N is the number of lattice vectors. By substituting Eqs. (2.19-2.21) into the LB equation (2.17), we obtain

$$\sum_{n=1}^{\infty} \frac{\delta^n}{n!} \left[\vec{e}_i \cdot \vec{\nabla} + \sum_{m=0}^{\infty} \delta^m \frac{\partial_m}{\partial t}\right]^n \sum_{p=0}^{\infty} \delta^p f_i^{(p)} = -\sum_{n=1}^{\infty} \delta^n \sum_{j=1}^{N} \Omega_{ij} f_j^{(n)} \tag{2.23}$$

Let us order this equation after powers of δ and assume that the coefficients of the δ^n

vanish. To the first order of δ, we obtain

$$\left[\frac{\partial_0}{\partial t} + \vec{e}_i \cdot \vec{\nabla}\right] f_i^{(0)} = -\sum_{j=1}^{N} \Omega_{ij} f_j^{(1)} \tag{2.24}$$

To the second order of δ, we obtain

$$\frac{\partial_1}{\partial t} f_i^{(0)} + \left(\frac{\partial_0}{\partial t} + \vec{e}_i \cdot \vec{\nabla}\right) \left[f_i^{(1)} - \frac{1}{2}\sum_{j=1}^{N} \Omega_{ij} f_j^{(1)}\right] = -\sum_{j=1}^{N} \Omega_{ij} f_j^{(2)} \tag{2.25}$$

Multiplying Eqs. (2.24) and (2.25) by the transformation matrix M converts them into moment space:

$$\frac{\partial_0}{\partial t}|m^{(0)}\rangle + \sum_{\alpha} \mathsf{A}^{(\alpha)} \vec{\nabla}_\alpha |m^{(0)}\rangle = -\mathsf{S}|m^{(1)}\rangle \tag{2.26}$$

$$\frac{\partial_1}{\partial t}|m^{(0)}\rangle + \frac{\partial_0}{\partial t}\left(\mathsf{I} - \frac{1}{2}\mathsf{S}\right)|m^{(1)}\rangle + \sum_{\alpha} \mathsf{A}^{(\alpha)} \vec{\nabla}_\alpha \left(\mathsf{I} - \frac{1}{2}\mathsf{S}\right)|m^{(1)}\rangle = -\mathsf{S}|m^{(2)}\rangle \tag{2.27}$$

Here $\mathsf{A}^{(\alpha)}$ is a constant $N \times N$ matrix, which is defined for all Cartesian directions α and the components of which are given by

$$\mathsf{A}_{pq}^{(\alpha)} = \sum_{i} \mathsf{M}_{pi} \vec{e}_{i,\alpha} \mathsf{M}_{iq}^{-1} \tag{2.28}$$

where $\vec{e}_{i,\alpha}$ is the αth Cartesian component of the ith lattice vector.

For the D3Q19 model, the lattice vectors are

$$(\vec{e}_1, \vec{e}_2, \ldots, \vec{e}_{19}) = \begin{pmatrix} 0 & 1 & -1 & 0 & 0 & 0 & 0 & 1 & -1 & 1 & -1 & 1 & -1 & 1 & -1 & 0 & 0 & 0 & 0 \\ 0 & 0 & 0 & 1 & -1 & 0 & 0 & 1 & -1 & -1 & 1 & 0 & 0 & 0 & 0 & 1 & -1 & 1 & -1 \\ 0 & 0 & 0 & 0 & 0 & 1 & -1 & 0 & 0 & 0 & 0 & 1 & -1 & -1 & 1 & 1 & -1 & -1 & 1 \end{pmatrix}$$

We used methods from d'Humières et al. [10]'s paper to construct the transformation matrix M, although we selected a different order of the lattice vectors in order to simplify numerical implementation.

$$\mathsf{M} = \begin{pmatrix} 1 & 1 & 1 & 1 & 1 & 1 & 1 & 1 & 1 & 1 & 1 & 1 & 1 & 1 & 1 & 1 & 1 & 1 & 1 \\ -30 & -11 & -11 & -11 & -11 & -11 & -11 & 8 & 8 & 8 & 8 & 8 & 8 & 8 & 8 & 8 & 8 & 8 & 8 \\ 12 & -4 & -4 & -4 & -4 & -4 & -4 & 1 & 1 & 1 & 1 & 1 & 1 & 1 & 1 & 1 & 1 & 1 & 1 \\ 0 & 1 & -1 & 0 & 0 & 0 & 0 & 1 & -1 & 1 & -1 & 1 & -1 & 1 & -1 & 0 & 0 & 0 & 0 \\ 0 & -4 & 4 & 0 & 0 & 0 & 0 & 1 & -1 & 1 & -1 & 1 & -1 & 1 & -1 & 0 & 0 & 0 & 0 \\ 0 & 0 & 0 & 1 & -1 & 0 & 0 & 1 & -1 & -1 & 1 & 0 & 0 & 0 & 0 & 1 & -1 & 1 & -1 \\ 0 & 0 & 0 & -4 & 4 & 0 & 0 & 1 & -1 & -1 & 1 & 0 & 0 & 0 & 0 & 1 & -1 & 1 & -1 \\ 0 & 0 & 0 & 0 & 0 & 1 & -1 & 0 & 0 & 0 & 0 & 1 & -1 & -1 & 1 & 1 & -1 & -1 & 1 \\ 0 & 0 & 0 & 0 & 0 & -4 & 4 & 0 & 0 & 0 & 0 & 1 & -1 & -1 & 1 & 1 & -1 & -1 & 1 \\ 0 & 2 & 2 & -1 & -1 & -1 & -1 & 1 & 1 & 1 & 1 & 1 & 1 & 1 & 1 & -2 & -2 & -2 & -2 \\ 0 & -4 & -4 & 2 & 2 & 2 & 2 & 1 & 1 & 1 & 1 & 1 & 1 & 1 & 1 & -2 & -2 & -2 & -2 \\ 0 & 0 & 0 & 1 & 1 & -1 & -1 & 1 & 1 & 1 & 1 & -1 & -1 & -1 & -1 & 0 & 0 & 0 & 0 \\ 0 & 0 & 0 & -2 & -2 & 2 & 2 & 1 & 1 & 1 & 1 & -1 & -1 & -1 & -1 & 0 & 0 & 0 & 0 \\ 0 & 0 & 0 & 0 & 0 & 0 & 0 & 1 & 1 & -1 & -1 & 0 & 0 & 0 & 0 & 0 & 0 & 0 & 0 \\ 0 & 0 & 0 & 0 & 0 & 0 & 0 & 0 & 0 & 0 & 0 & 0 & 0 & 0 & 0 & 1 & 1 & -1 & -1 \\ 0 & 0 & 0 & 0 & 0 & 0 & 0 & 0 & 0 & 0 & 0 & 1 & 1 & -1 & -1 & 0 & 0 & 0 & 0 \\ 0 & 0 & 0 & 0 & 0 & 0 & 0 & 1 & -1 & 1 & -1 & -1 & 1 & -1 & 1 & 0 & 0 & 0 & 0 \\ 0 & 0 & 0 & 0 & 0 & 0 & 0 & -1 & 1 & 1 & -1 & 0 & 0 & 0 & 0 & 1 & -1 & 1 & -1 \\ 0 & 0 & 0 & 0 & 0 & 0 & 0 & 0 & 0 & 0 & 0 & 1 & -1 & -1 & 1 & -1 & 1 & 1 & -1 \end{pmatrix}$$

This matrix transfers the particle distribution function f to the hydrodynamic moment vector $|m\rangle$,

$$|m\rangle = \mathsf{M}|f\rangle = (C, e, \psi, j_x, q_x, j_y, q_y, j_z, q_z, 3p_{xx}, 3\pi_{xx}, p_{ww}, \pi_{ww}, p_{xy}, p_{yz}, p_{xz}, m_x, m_y, m_z)^T$$

We only consider the first, fourth, sixth, and eighth moments, which represent the concentration and the mass flux density in the continuum-scale equations (4.26) and (4.27). Since $\vec{e}_i$ and M are now known, we can calculate the three $\mathsf{A}^{(\alpha)}$ matrices according to Eq. (2.28),

$$\mathsf{A}^{(x)} = \begin{pmatrix}
0 & 0 & 0 & 1 & 0 & 0 & 0 & 0 & 0 & 0 & 0 & 0 & 0 & 0 & 0 & 0 & 0 & 0 & 0 \\
0 & 0 & 0 & 21/5 & 19/5 & 0 & 0 & 0 & 0 & 0 & 0 & 0 & 0 & 0 & 0 & 0 & 0 & 0 & 0 \\
0 & 0 & 0 & 0 & 1 & 0 & 0 & 0 & 0 & 0 & 0 & 0 & 0 & 0 & 0 & 0 & 0 & 0 & 0 \\
10/19 & 1/57 & 0 & 0 & 0 & 0 & 0 & 0 & 0 & 1/3 & 0 & 0 & 0 & 0 & 0 & 0 & 0 & 0 & 0 \\
0 & 4/63 & 10/63 & 0 & 0 & 0 & 0 & 0 & 0 & -2/9 & 5/9 & 0 & 0 & 0 & 0 & 0 & 0 & 0 & 0 \\
0 & 0 & 0 & 0 & 0 & 0 & 0 & 0 & 0 & 0 & 0 & 0 & 0 & 1 & 0 & 0 & 0 & 0 & 0 \\
0 & 0 & 0 & 0 & 0 & 0 & 0 & 0 & 0 & 0 & 0 & 0 & 0 & 1 & 0 & 0 & 0 & 0 & 0 \\
0 & 0 & 0 & 0 & 0 & 0 & 0 & 0 & 0 & 0 & 0 & 0 & 0 & 0 & 0 & 1 & 0 & 0 & 0 \\
0 & 0 & 0 & 0 & 0 & 0 & 0 & 0 & 0 & 0 & 0 & 0 & 0 & 0 & 0 & 1 & 0 & 0 & 0 \\
0 & 0 & 0 & 6/5 & -1/5 & 0 & 0 & 0 & 0 & 0 & 0 & 0 & 0 & 0 & 0 & 0 & 0 & 0 & 0 \\
0 & 0 & 0 & 0 & 1 & 0 & 0 & 0 & 0 & 0 & 0 & 0 & 0 & 0 & 0 & 0 & 0 & 0 & 0 \\
0 & 0 & 0 & 0 & 0 & 0 & 0 & 0 & 0 & 0 & 0 & 0 & 0 & 0 & 0 & 0 & 1 & 0 & 0 \\
0 & 0 & 0 & 0 & 0 & 0 & 0 & 0 & 0 & 0 & 0 & 0 & 0 & 0 & 0 & 0 & 1 & 0 & 0 \\
0 & 0 & 0 & 0 & 0 & 2/5 & 1/10 & 0 & 0 & 0 & 0 & 0 & 0 & 0 & 0 & 0 & 0 & -1/2 & 0 \\
0 & 0 & 0 & 0 & 0 & 0 & 0 & 0 & 0 & 0 & 0 & 0 & 0 & 0 & 0 & 0 & 0 & 0 & 0 \\
0 & 0 & 0 & 0 & 0 & 0 & 0 & 2/5 & 1/10 & 0 & 0 & 0 & 0 & 0 & 0 & 0 & 0 & 0 & 1/2 \\
0 & 0 & 0 & 0 & 0 & 0 & 0 & 0 & 0 & 0 & 0 & 2/3 & 1/3 & 0 & 0 & 0 & 0 & 0 & 0 \\
0 & 0 & 0 & 0 & 0 & 0 & 0 & 0 & 0 & 0 & 0 & 0 & 0 & -1 & 0 & 0 & 0 & 0 & 0 \\
0 & 0 & 0 & 0 & 0 & 0 & 0 & 0 & 0 & 0 & 0 & 0 & 0 & 0 & 0 & 1 & 0 & 0 & 0
\end{pmatrix}$$

$$
\mathsf{A}^{(y)} = \begin{pmatrix}
0 & 0 & 0 & 0 & 0 & 1 & 0 & 0 & 0 & 0 & 0 & 0 & 0 & 0 & 0 & 0 & 0 & 0 & 0 \\
0 & 0 & 0 & 0 & 0 & 21/5 & 19/5 & 0 & 0 & 0 & 0 & 0 & 0 & 0 & 0 & 0 & 0 & 0 & 0 \\
0 & 0 & 0 & 0 & 0 & 0 & 1 & 0 & 0 & 0 & 0 & 0 & 0 & 0 & 0 & 0 & 0 & 0 & 0 \\
0 & 0 & 0 & 0 & 0 & 0 & 0 & 0 & 0 & 0 & 0 & 0 & 0 & 1 & 0 & 0 & 0 & 0 & 0 \\
0 & 0 & 0 & 0 & 0 & 0 & 0 & 0 & 0 & 0 & 0 & 0 & 0 & 1 & 0 & 0 & 0 & 0 & 0 \\
10/19 & 1/57 & 0 & 0 & 0 & 0 & 0 & 0 & 0 & -1/6 & 0 & 1/2 & 0 & 0 & 0 & 0 & 0 & 0 & 0 \\
0 & 4/63 & 10/63 & 0 & 0 & 0 & 0 & 0 & 0 & 1/9 & -5/18 & -1/3 & 5/6 & 0 & 0 & 0 & 0 & 0 & 0 \\
0 & 0 & 0 & 0 & 0 & 0 & 0 & 0 & 0 & 0 & 0 & 0 & 0 & 0 & 1 & 0 & 0 & 0 & 0 \\
0 & 0 & 0 & 0 & 0 & 0 & 0 & 0 & 0 & 0 & 0 & 0 & 0 & 0 & 1 & 0 & 0 & 0 & 0 \\
0 & 0 & 0 & 0 & 0 & -3/5 & 1/10 & 0 & 0 & 0 & 0 & 0 & 0 & 0 & 0 & 0 & 0 & -3/2 & 0 \\
0 & 0 & 0 & 0 & 0 & 0 & -1/2 & 0 & 0 & 0 & 0 & 0 & 0 & 0 & 0 & 0 & 0 & -3/2 & 0 \\
0 & 0 & 0 & 0 & 0 & 3/5 & -1/10 & 0 & 0 & 0 & 0 & 0 & 0 & 0 & 0 & 0 & 0 & -1/2 & 0 \\
0 & 0 & 0 & 0 & 0 & 0 & 1/2 & 0 & 0 & 0 & 0 & 0 & 0 & 0 & 0 & 0 & 0 & -1/2 & 0 \\
0 & 0 & 0 & 2/5 & 1/10 & 0 & 0 & 0 & 0 & 0 & 0 & 0 & 0 & 0 & 0 & 0 & 1/2 & 0 & 0 \\
0 & 0 & 0 & 0 & 0 & 0 & 0 & 2/5 & 1/10 & 0 & 0 & 0 & 0 & 0 & 0 & 0 & 0 & 0 & -1/2 \\
0 & 0 & 0 & 0 & 0 & 0 & 0 & 0 & 0 & 0 & 0 & 0 & 0 & 0 & 0 & 0 & 0 & 0 & 0 \\
0 & 0 & 0 & 0 & 0 & 0 & 0 & 0 & 0 & 0 & 0 & 0 & 0 & 1 & 0 & 0 & 0 & 0 & 0 \\
0 & 0 & 0 & 0 & 0 & 0 & 0 & 0 & 0 & -1/3 & -1/6 & -1/3 & -1/6 & 0 & 0 & 0 & 0 & 0 & 0 \\
0 & 0 & 0 & 0 & 0 & 0 & 0 & 0 & 0 & 0 & 0 & 0 & 0 & 0 & -1 & 0 & 0 & 0 & 0
\end{pmatrix}
$$

$$
\mathsf{A}^{(z)} = \begin{pmatrix}
0 & 0 & 0 & 0 & 0 & 0 & 0 & 1 & 0 & 0 & 0 & 0 & 0 & 0 & 0 & 0 & 0 & 0 & 0 \\
0 & 0 & 0 & 0 & 0 & 0 & 0 & 21/5 & 19/5 & 0 & 0 & 0 & 0 & 0 & 0 & 0 & 0 & 0 & 0 \\
0 & 0 & 0 & 0 & 0 & 0 & 0 & 0 & 1 & 0 & 0 & 0 & 0 & 0 & 0 & 0 & 0 & 0 & 0 \\
0 & 0 & 0 & 0 & 0 & 0 & 0 & 0 & 0 & 0 & 0 & 0 & 0 & 0 & 0 & 1 & 0 & 0 & 0 \\
0 & 0 & 0 & 0 & 0 & 0 & 0 & 0 & 0 & 0 & 0 & 0 & 0 & 0 & 0 & 1 & 0 & 0 & 0 \\
0 & 0 & 0 & 0 & 0 & 0 & 0 & 0 & 0 & 0 & 0 & 0 & 0 & 0 & 1 & 0 & 0 & 0 & 0 \\
0 & 0 & 0 & 0 & 0 & 0 & 0 & 0 & 0 & 0 & 0 & 0 & 0 & 0 & 1 & 0 & 0 & 0 & 0 \\
10/19 & 1/57 & 0 & 0 & 0 & 0 & 0 & 0 & 0 & -1/6 & 0 & -1/2 & 0 & 0 & 0 & 0 & 0 & 0 & 0 \\
0 & 4/63 & 10/63 & 0 & 0 & 0 & 0 & 0 & 0 & 1/9 & -5/18 & 1/3 & -5/6 & 0 & 0 & 0 & 0 & 0 & 0 \\
0 & 0 & 0 & 0 & 0 & 0 & 0 & -3/5 & 1/10 & 0 & 0 & 0 & 0 & 0 & 0 & 0 & 0 & 0 & 3/2 \\
0 & 0 & 0 & 0 & 0 & 0 & 0 & 0 & -1/2 & 0 & 0 & 0 & 0 & 0 & 0 & 0 & 0 & 0 & 3/2 \\
0 & 0 & 0 & 0 & 0 & 0 & 0 & -3/5 & 1/10 & 0 & 0 & 0 & 0 & 0 & 0 & 0 & 0 & 0 & -1/2 \\
0 & 0 & 0 & 0 & 0 & 0 & 0 & 0 & -1/2 & 0 & 0 & 0 & 0 & 0 & 0 & 0 & 0 & 0 & -1/2 \\
0 & 0 & 0 & 0 & 0 & 0 & 0 & 0 & 0 & 0 & 0 & 0 & 0 & 0 & 0 & 0 & 0 & 0 & 0 \\
0 & 0 & 0 & 0 & 0 & 2/5 & 1/10 & 0 & 0 & 0 & 0 & 0 & 0 & 0 & 0 & 0 & 0 & 1/2 & 0 \\
0 & 0 & 0 & 2/5 & 1/10 & 0 & 0 & 0 & 0 & 0 & 0 & 0 & 0 & 0 & 0 & 0 & -1/2 & 0 & 0 \\
0 & 0 & 0 & 0 & 0 & 0 & 0 & 0 & 0 & 0 & 0 & 0 & 0 & 0 & 0 & -1 & 0 & 0 & 0 \\
0 & 0 & 0 & 0 & 0 & 0 & 0 & 0 & 0 & 0 & 0 & 0 & 0 & 0 & 1 & 0 & 0 & 0 & 0 \\
0 & 0 & 0 & 0 & 0 & 0 & 0 & 0 & 0 & 1/3 & 1/6 & -1/3 & -1/6 & 0 & 0 & 0 & 0 & 0 & 0
\end{pmatrix}
$$

Now we evaluate the first component of Eq. (2.26) and get

$$\frac{\partial_0 C^{(0)}}{\partial t} + \frac{\partial j_x^{(0)}}{\partial x} + \frac{\partial j_y^{(0)}}{\partial y} + \frac{\partial j_z^{(0)}}{\partial z} = 0 \tag{2.29}$$

where $C^{(0)} = C$. To ensure that this first-order mass balance equation describes the advective transport of the concentration C, the equilibrium mass flux vector must be given by

$$\vec{j}^{(0)} = C(\hat{\vec{v}} + \hat{\vec{v}}_c) \tag{2.30}$$

where $\hat{\vec{v}}$ is the known dimensionless fluid velocity, and $\hat{\vec{v}}_c$ is the dimensionless bacterial

chemotactic velocity. For the substrate, $\hat{\vec{v}}_c = 0$. The concentration change due to diffusion is quantified by the first component of Eq. (2.27),

$$\frac{\partial_1 C}{\partial t} + \frac{\partial}{\partial x}\left[\left(1 - \tfrac{1}{2}s_4\right) j_x^{(1)}\right] + \frac{\partial}{\partial y}\left[\left(1 - \tfrac{1}{2}s_6\right) j_y^{(1)}\right] + \frac{\partial}{\partial z}\left[\left(1 - \tfrac{1}{2}s_8\right) j_z^{(1)}\right] = 0 \qquad (2.31)$$

In order to determine $j_x^{(1)}$, $j_y^{(1)}$ and $j_z^{(1)}$, we evaluate the fourth, sixth, and eighth components of Eq. (2.26),

$$\frac{\partial_0 j_x^{(0)}}{\partial t} + \frac{\partial}{\partial x}\left(\tfrac{10}{19}C + \tfrac{1}{57}e^{(0)} + p_{xx}^{(0)}\right) + \frac{\partial p_{xy}^{(0)}}{\partial y} + \frac{\partial p_{zx}^{(0)}}{\partial z} = -s_4 j_x^{(1)} \qquad (2.32)$$

$$\frac{\partial_0 j_y^{(0)}}{\partial t} + \frac{\partial p_{xy}^{(0)}}{\partial x} + \frac{\partial}{\partial y}\left(\tfrac{10}{19}C + \tfrac{1}{57}e^{(0)} - \tfrac{1}{2}p_{xx}^{(0)} + \tfrac{1}{2}p_{ww}^{(0)}\right) + \frac{\partial p_{yz}^{(0)}}{\partial z} = -s_6 j_y^{(1)} \qquad (2.33)$$

$$\frac{\partial_0 j_z^{(0)}}{\partial t} + \frac{\partial p_{zx}^{(0)}}{\partial x} + \frac{\partial p_{yz}^{(0)}}{\partial y} + \frac{\partial}{\partial z}\left(\tfrac{10}{19}C + \tfrac{1}{57}e^{(0)} - \tfrac{1}{2}p_{xx}^{(0)} - \tfrac{1}{2}p_{ww}^{(0)}\right) = -s_8 j_z^{(1)} \qquad (2.34)$$

By solving Eqs. (2.32), (2.33) and (2.34) for $j_x^{(1)}$, $j_y^{(1)}$ and $j_z^{(1)}$, and substituting the results into Eq. (2.31), we obtain

$$\begin{aligned}
\frac{\partial_1 C}{\partial t} &= \frac{\partial}{\partial x}\left\{\left(\frac{1}{s_4} - \frac{1}{2}\right)\left[\frac{\partial_0 j_x^{(0)}}{\partial t} + \frac{\partial}{\partial x}\left(\tfrac{10}{19}C + \tfrac{1}{57}e^{(0)} + p_{xx}^{(0)}\right) + \frac{\partial p_{xy}^{(0)}}{\partial y} + \frac{\partial p_{zx}^{(0)}}{\partial z}\right]\right\} \qquad (2.35)\\
&+ \frac{\partial}{\partial y}\left\{\left(\frac{1}{s_6} - \frac{1}{2}\right)\left[\frac{\partial_0 j_y^{(0)}}{\partial t} + \frac{\partial p_{xy}^{(0)}}{\partial x} + \frac{\partial}{\partial y}\left(\tfrac{10}{19}C + \tfrac{1}{57}e^{(0)} - \tfrac{1}{2}p_{xx}^{(0)} + \tfrac{1}{2}p_{ww}^{(0)}\right) + \frac{\partial p_{yz}^{(0)}}{\partial z}\right]\right\}\\
&+ \frac{\partial}{\partial z}\left\{\left(\frac{1}{s_8} - \frac{1}{2}\right)\left[\frac{\partial_0 j_z^{(0)}}{\partial t} + \frac{\partial p_{zx}^{(0)}}{\partial x} + \frac{\partial p_{yz}^{(0)}}{\partial y} + \frac{\partial}{\partial z}\left(\tfrac{10}{19}C + \tfrac{1}{57}e^{(0)} - \tfrac{1}{2}p_{xx}^{(0)} - \tfrac{1}{2}p_{ww}^{(0)}\right)\right]\right\}
\end{aligned}$$

In order to model isotropic diffusion, mixed spatial quantities must vanish, thus $p_{zx}^{(0)} = p_{yz}^{(0)} = p_{zx}^{(0)} = 0$. Furthermore, for the sake of symmetry, we set $p_{xx}^{(0)} = p_{ww}^{(0)} = 0$ and use

the same collision rates in all three Cartesian directions, $s_4 = s_6 = s_8 := 1/\tau$. $s_1 = 0$ is required to ensure mass conservation. All other elements of S are free to choose, and they only affect numerical stability rather than mass conservation. The only remaining unknown parameter is $e^{(0)}$. In order to obtain a similar expression for the relaxation time as the SRT-LB model, d'Humières et al. [10] chose $e^{(0)} = -11C$ when applying the MRT-LB model to simulate a velocity field. However, this value makes our simulations unstable, which could be due to the fact that the momentum of neither the bacteria nor the chemoattractant is generally conserved. As a result, we choose $e^{(0)} = -1.5C$, which has the best stability in our parameter tests. Therefore,

$$\frac{\partial_1 C}{\partial t} = \frac{1}{2}\left(\tau - \frac{1}{2}\right)\hat{\vec{\nabla}}^2 C + \left(\tau - \frac{1}{2}\right)\hat{\vec{\nabla}} \cdot \frac{\partial_0 \vec{j}^{(0)}}{\partial t} \tag{2.36}$$

Like Hilpert [19], we assume that the velocity fields, $\hat{\vec{v}}$ and $\hat{\vec{v}}_c$, vary slowly in both time and space dimension, such that $\partial_0 \hat{\vec{v}}/\partial t \approx 0$, $\partial_0 \hat{\vec{v}}_c/\partial t \approx 0$, $\hat{\vec{\nabla}} \cdot \hat{\vec{v}} \approx 0$, and $\hat{\vec{\nabla}} \cdot \hat{\vec{v}}_c \approx 0$. We can then use Eq. (2.29) to rewrite the mixed derivative on the right-hand-side of Eq. (2.36), $\hat{\vec{\nabla}} \cdot \partial_0 \vec{j}^{(0)}/\partial t = -||\hat{\vec{v}} + \hat{\vec{v}}_c||^2 C$. By multiplying Eq. (2.36) by δ and adding the result to Eq. (2.29), we obtain the transport equation accurate to second order,

$$\frac{\partial C}{\partial t} + \hat{\vec{\nabla}} \cdot C(\hat{\vec{v}} + \hat{\vec{v}}_c) = \hat{D}\hat{\vec{\nabla}}^2 C - 2\hat{D}||\hat{\vec{v}} + \hat{\vec{v}}_c||^2 \hat{\vec{\nabla}}^2 C + O(\delta^2) \tag{2.37}$$

where

$$\hat{D} = \delta \frac{1}{2}\left(\tau - \frac{1}{2}\right) \tag{2.38}$$

In LBM simulations, one needs to guarantee $||\hat{\vec{v}} + \hat{\vec{v}}_c|| \ll 1$, which can be achieved by choosing a suitable typical velocity to nondimensionalize the transport equation. Otherwise, the simulations become numerical unstable. Therefore, the second term on the right-hand-side of Eq. (2.37) is much smaller than the first term on the right-hand-side and can be ignored. When $\delta \to 0$, the LB model achieves solutions to the following dimensionless advection diffusion equation:

$$\frac{\partial C}{\partial t} + \hat{\vec{\nabla}} \cdot C(\hat{\vec{v}} + \hat{\vec{v}}_c) = \hat{D}\hat{\vec{\nabla}}^2 C \tag{2.39}$$

where $\hat{D} = 1/\text{Pe}$ as in Eqs. (4.26) and (4.27). We still need to make choices for $\psi^{(0)}$, $q^{(0)}_{x,y,z}$ and $m^{(0)}_{x,y,z}$. Like d'Humières et al. [10], we choose $\psi^{(0)} = -C$, $q^{(0)}_x = -7j^{(0)}_x/3$, $q^{(0)}_y = -7j^{(0)}_y/3$, $q^{(0)}_z = -7j^{(0)}_z/3$, and $m^{(0)}_{x,y,z} = 0$. For clarity, we display the entire equilibrium moment vector of the bacteria and the substrate:

$$\begin{aligned} |m^0_b\rangle \;=\; & (\hat{b}, -1.5\hat{b}, -\hat{b}, \hat{b}(\hat{v}_x + \hat{v}_{c,x}), -\tfrac{7}{3}\hat{b}(\hat{v}_x + \hat{v}_{c,x}), \hat{b}(\hat{v}_y + \hat{v}_{c,y}), -\tfrac{7}{3}\hat{b}(\hat{v}_y + \hat{v}_{c,y}), \\ & \hat{b}(\hat{v}_z + \hat{v}_{c,z}), -\tfrac{7}{3}\hat{b}(\hat{v}_z + \hat{v}_{c,z}), 0, 0, 0, 0, 0, 0, 0, 0, 0, 0)^T \end{aligned}$$

$$|m^0_s\rangle \;=\; (\hat{s}, -1.5\hat{s}, -\hat{s}, \hat{s}\hat{v}_x, -\tfrac{7}{3}\hat{s}\hat{v}_x, \hat{s}\hat{v}_y, -\tfrac{7}{3}\hat{s}\hat{v}_y, \hat{s}\hat{v}_z, -\tfrac{7}{3}\hat{s}\hat{v}_z, 0, 0, 0, 0, 0, 0, 0, 0, 0, 0)^T$$

2.7 Appendix B: Accuracy analysis of multiple-relaxation-time lattice Boltzmann method

To further analyze the order of accuracy of the MRT-LBM, we simulated pure diffusion of a chemical in a dilute solution and compared the simulation results to an analytical solution. In 1D, the problem is mathematically described by the following partial differential equation:

$$\frac{\partial c}{\partial t} = D\frac{\partial^2 c}{\partial x^2} \tag{2.40}$$

where c is the concentration of the dissolved chemical. We chose the diffusion coefficient to be $D = 5 \times 10^{-6}$. With periodic boundary condition, $c(-\pi, t) = c(\pi, t)$ for $t > 0$, and the initial condition, $c(x, 0) = e^{-x^2}$ for $-\pi \leq x \leq \pi$, we obtained the following analytical solution via the method of separation of variables [8]:

$$c(x,t) = \frac{i}{4\sqrt{\pi}} \sum_{n=-\infty}^{\infty} e^{-\frac{n^2}{4}} \left[\text{erfi}\left(\frac{n}{2} - i\pi\right) - \text{erfi}\left(\frac{n}{2} + i\pi\right)\right] \cos(nx) e^{-n^2 Dt} \tag{2.41}$$

where erfi is the imaginary error function, which can be defined in terms of the error function $\text{erf}(x) = \frac{2}{\sqrt{\pi}} \int_0^x e^{-t^2} dt$ through $\text{erfi}(x) = -i\ \text{erf}(ix)$.

The MRT-LBM was used to simulate the diffusion problem, and simulation results were compared to the analytical solution. Figure 2.13 shows this comparison for different grid spacings Δx. The findings illustrate that the simulation results agree well with the analytical solution.

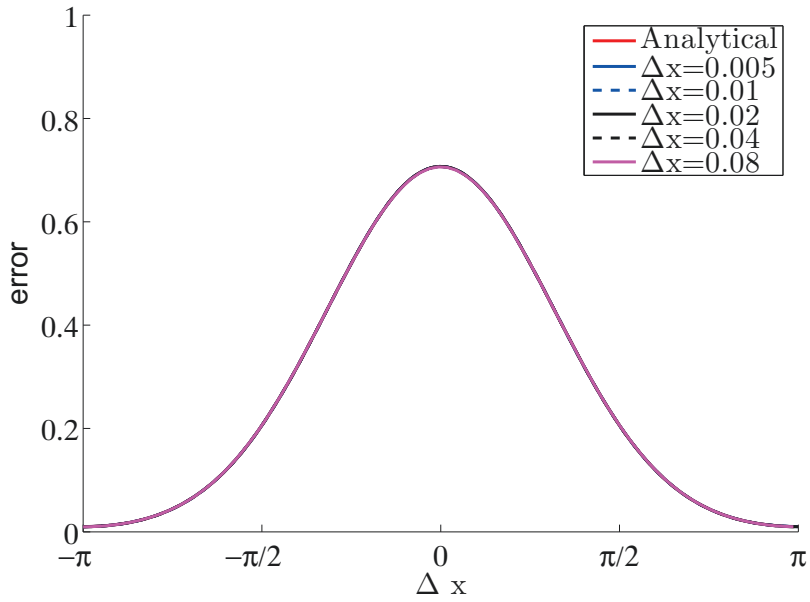

Figure 2.13: Comparison of simulation results for different grid spacings against the analytical solution when $t = 50000$.

Since this problem has an analytical solution, we can evaluate the order of accuracy of the MRT-LBM by calculating the following average error:

$$\epsilon = \frac{\sum_{i=1}^{N} |c_i^{analytical} - c_i^{simulation}|}{N} \tag{2.42}$$

where c_i is the concentration at grid nodes that discretize the domain and N is the number of the nodes. The error is plotted as a function of the grid spacing in Figure 2.14. This error asymptotically approaches a slope of 2: the error is reduced by two orders of magnitude when the grid spacing is reduced one order of magnitude. Therefore, the MRT-LBM is a second-order scheme [14].

In the analysis, we used Matlab^{TM} to calculate the analytical solution in Eq. (2.41).

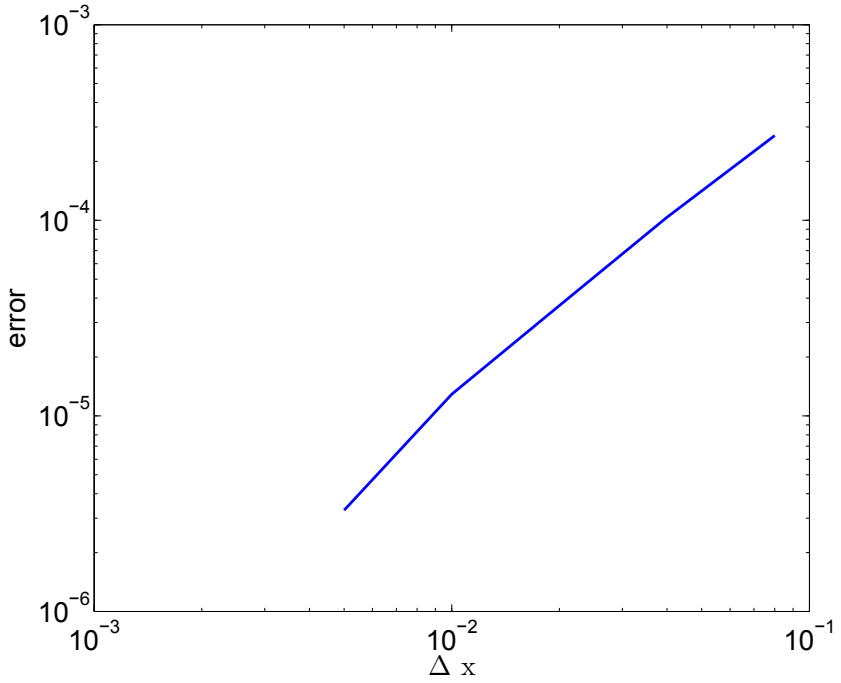

Figure 2.14: Average error in the pure diffusion as a function of grid spacing.

The maximum allowable $|n|$ value was 38, and larger values could not be evaluated. Consequently, the simulation results were compared to an approximate analytical solution instead of the exact solution. This difference between the approximate analytical solution and the exact solution is much smaller than the error in Eq. (2.42) and can be neglected as long as the grid spacing is not too small. However, if the grid spacing becomes too fine, this difference becomes comparable to the error and invalidates the accuracy analysis. That is why we do not present the error ϵ for smaller grid spacings.

Bibliography

[1] J.P. Adler. Chemotaxis in bacteria. *Science*, 153:708–716, 1966.

[2] G. Alexandre, S. Greer-Phillips, and I. Zhulin. Ecological role of energy taxis in microorganisms. *FEMS Microbiology Reviews*, 28(1):113–126, feb 2004.

[3] S. Bennett, P. Asinari, and P.J. Dellar. A lattice Boltzmann model for diffusion of binary gas mixtures that includes diffusion slip - Bennett - 2011 - International Journal for Numerical Methods in Fluids - Wiley Online Library. *International Journal for Numerical Methods in Fluids*, 69(1):171–189, May 2012.

[4] T. Bosma, J.L. Schnoor, and G. Schraa. Simulation model for biotransformation of xenobiotics and chemotaxis in soil columns. *Journal of Contaminant Hydrology*, 2 (3):225–236, July 1988.

[5] B.J. Brosilow, R.M. Ford, S.S. Sarman, and P.T. Cummings. Numerical solution of transport equations for bacterial chemotaxis. *SIAM Journal on Applied Mathematics*, 56:1639–1663, 1996.

[6] E.O. Budrene and H.C. Berg. Dynamics of formation of symmetrical patterns by chemotactic bacteria. *Nature*, 376(6535):49–53, July 1995.

[7] S. Chen and G. Doolen. Lattice Boltzmann method for fluid flows. *Annual Review of Fluid Mechanics*, 30:329–364, 1998.

[8] J. Crank. *The Mathematics of Diffusion*. Oxford Science Publications, 1980.

[9] D. d'Humières. Generalized lattice-Boltzmann equations. *Rarefied Gas Dynamics-Theory and Simulations; Proceedings of the 18th International Symposium on Rarefied Gas Dynamics, Univ.of British Columbia, Vancouver, Canada; United States*, pages 26–30, 1992.

[10] D. d'Humières, I. Ginzburg, M. Krafczyk, P. Lallemand, and L.S. Luo. Multiple-relaxation-time lattice Boltzmann models in three dimensions. *Philosophical Transactions of The Royal Society of London Series A*, 360(1792):437–451, 2002.

[11] R. Dillon and L. Fauci. A microscale model of bacterial and biofilm dynamics in porous media. *Biotechnology and Bioengineering*, 68(5):536–547, June 2000.

[12] K.J. Duffy, P.T. Cummings, and R.M. Ford. Random walk calculations for bacterial migration in porous media. *Biophysical Journal*, 68:800–806, 1995.

[13] T. Fenchel. Microbial behavior in a heterogeneous world. *Science*, 296(5570):1068–1071, May 2002.

[14] J.H. Ferziger and M. Perić. Computational methods for fluid dynamics. 1999.

[15] A.C. Grimm and C.S. Harwood. Chemotaxis of $Pseudomonas$ spp.to the polyaro-

matic hydrocarbon naphthalene. *Applied and Environmental Microbiology*, 63(10): 4111–4115, 1997.

[16] A.C. Hawkins and C.S. Harwood. Chemotaxis of Ralstonia eutropha JMP134 (pJP4) to the herbicide 2, 4-dichlorophenoxyacetate. *Applied and Environmental Microbiology*, 68(2):968–972, February 2002.

[17] X. He, Q. Zou, L Luo, and M. Dembo. Analytic solutions of simple flows and analysis of nonslip boundary conditions for the lattice Boltzmann BGK model. *Journal of Statistical Physics*, 1997.

[18] T. Hillen and K.J. Painter. A user's guide to PDE models for chemotaxis. *Journal of Mathematical Biology*, 58:183–217, 2009.

[19] M. Hilpert. Lattice-Boltzmann model for bacterial chemotaxis. *Journal of Mathematical Biology*, 51(3):302–332, May 2005.

[20] D. Horstmann. From 1970 until present: the Keller-Segel model in chemotaxis and its consequences I. *Jahresbericht DMV*, 105(3):103–165, 2003.

[21] D. Horstmann and A. Stevens. A Constructive Approach to Traveling Waves in Chemotaxis. *Journal of Nonlinear Science*, 14(1):1–25, 2004.

[22] E. Jabbarzadeh and C.F. Abrams. Simulations of Chemotaxis and Random Motility in Finite Domains. *Cambridge Univ Press*, 2005.

[23] E. Jabbarzadeh and C.F. Abrams. Simulations of chemotaxis and random motility in 2D random porous domains. *Bulletin of Mathematical Biology*, 69(2):747–764, February 2007.

[24] M. Junk and Z. Yang. One-point boundary condition for the lattice Boltzmann method. *Physical Review E*, 72(6):066701, December 2005.

[25] Y.V. Kalinin, L. Jiang, Y. Tu, and M. Wu. Logarithmic sensing in Escherichia coli bacterial chemotaxis. *Biophysical Journal*, 96(6):2439–2448, March 2009.

[26] E.F. Keller and L.A. Segel. Traveling bands of chemotactic bacteria: A theoretical analysis. *Journal of Theoretical Biology*, 30(2):235–248, February 1971.

[27] E.F. Keller and L.A. Segel. Model for chemotaxis. *Journal of Theoretical Biology*, 30:225–234, 1971.

[28] W. Long and M. Hilpert. Analytical solutions for bacterial energy taxis (chemotaxis): traveling bacterial bands. *Advances in Water Resources*, 30:2262–2270, 2007.

[29] W. Long and M. Hilpert. Lattice-Boltzmann modeling of contaminant degradation by chemotactic bacteria: Exploring the formation and movement of bacterial bands. *Water Resources Research*, 44:W09415, 2008.

[30] Marcos, Henry C Fu, Thomas R Powers, and Roman Stocker. Bacterial rheotaxis. *Proceedings of the National Academy of Sciences of the United States of America*, 109(13):4780–4785, March 2012.

[31] G.D. Marsily. *Quantitative Hydrogeology: Groundwater Hydrology for Engineers*. Academic Press, 1986.

[32] R.B. Marx and M.D. Aitken. Bacterial chemotaxis enhances naphthalene degradation in a heterogeneous aqueous system. *Environmental Science and Technology*, 34: 3379–3383, 2000.

[33] R.B. Marx and M.D. Aitken. Quantification of chemotaxis to naphthalene by *Pseudomonas putida* G7. *Applied and Environmental Microbiology*, 65:2847–2852, 1999.

[34] M.E. McCracken and J. Abraham. Multiple-relaxation-time lattice-Boltzmann model for multiphase flow. *Physical Review E*, 71:036701, 2005.

[35] R. Mei, W. Shyy, D. Yu, and L. Luo. Lattice boltzmann method for 3-D flows with curved boundary. *Journal of Computational Physics*, 161(2):680–699, July 2000.

[36] M.R. Myerscough, P.K. Maini, and K.J. Painter. Pattern formation in a generalized chemotactic model. *Bulletin of Mathematical Biology*, 60(1):1–26, January 1998.

[37] K.E. Nelson and T.R. Ginn. Theoretical investigation of bacterial chemotaxis in porous media. *Langmuir*, 17:5635–5645, 2001.

[38] M.S. Olson, R.M. Ford, J.A. Smith, and E.J. Fernandez. Quantification of bacterial chemotaxis in porous media using magnetic resonance imaging. *Environmental Science and Technology*, 38(14):3864–3870, July 2004.

[39] H.G. Othmer and T. Hillen. The diffusion limit of transport equations derived from velocity-jump processes. *SIAM Journal on Applied Mathematics*, 61(3):751–775, January 2000.

[40] C. Pan, J.F. Prins, and C.T. Miller. A high-performance lattice Boltzmann implementation to model flow in porous media. *Computer Physics Communications*, 158 (2):89–105, April 2004.

[41] C. Pan, L. Luo, and C.T. Miller. An evaluation of lattice Boltzmann schemes for porous medium flow simulation. *Computers and Fluids*, 35(8-9):898–909, 2006.

[42] G. Pandey and R.K. Jain. Bacterial chemotaxis toward environmental pollutants: role in bioremediation. *Applied and Environmental Microbiology*, 68(12):5789–5795, December 2002.

[43] R.E. Parales, J.L. Ditty, and C.S. Harwood. Toluene-degrading bacteria are chemotactic towards the environmental pollutants benzene, toluene, and trichloroethylene. *Applied and Environmental Microbiology*, 66(9):4098–4104, September 2000.

[44] S. Park, P.M. Wolanin, E.A. Yuzbashyan, H. Lin, N.C. Darnton, J.B. Stock, P. Silberzan, and R. Austin. Influence of topology on bacterial social interaction. *Proceedings of the National Academy of Sciences of the United States of America*, 100 (24):13910–13915, November 2003.

[45] J.A. Pedit, R.B. Marx, C.T. Miller, and M.D. Aitken. Quantitative analysis of exper-

iments on bacterial chemotaxis to naphthalene. *Biotechnology and Bioengineering*, 78(6):626–634, June 2002.

[46] Y. Qian, S. Succi, and S. Orszag. Recent advances in lattice Boltzmann computing. *Annual Reviews of Computationnal Physics III*, pages 195–242, 1995.

[47] M.A. Rivero, R.T. Tranquillo, H.M. Buettner, and D. Lauffenburger. Transport models for chemotactic cell populations based on individual cell behaviour. *Chemical Engineering Science*, 44(12):2881–2897, 1989.

[48] S.K. Samanta, B. Bhushan, and A. Chauhan. Chemotaxis of a Ralstonia sp.SJ98 toward different nitroaromatic compounds and their degradation. *Biochemical and Biophysical Research Communications*, 269(1):117–123, May 2000.

[49] J. Saragosti, V. Calvez, N. Bournaveas, A. Buguin, P. Silberzan, and B. Perthame. Mathematical description of bacterial traveling pulses. *PLoS Computational Biology*, 6(8), 2010.

[50] J. Saragosti, V. Calvez, N. Bournaveas, B. Perthame, A. Buguin, and P. Silberzan. Directional persistence of chemotactic bacteria in a traveling concentration wave. *Proceedings of the National Academy of Sciences of the United States of America*, 108(39):16235–16240, September 2011.

[51] R. Singh and M.S. Olson. Transverse mixing enhancement due to bacterial random

motility in porous microfluidic devices. *Environmental Science and Technology*, 45 (20):8780–8787, October 2011.

[52] J.R. Taylor and R. Stocker. Trade-offs of chemotactic foraging in turbulent water. *Science*, 338(6107):675–679, November 2012.

[53] M.J. Tindall, P.K. Maini, S.L. Porter, and J.P. Armitage. Overview of mathematical approaches used to model bacterial chemotaxis II: bacterial populations. *Bulletin of Mathematical Biology*, 70(6):1570–1607, August 2008.

[54] R. Tyson, L.G. Stern, and R.J. LeVeque. Fractional step methods applied to a chemotaxis model. *Journal of Mathematical Biology*, 41(5):455–475, November 2000.

[55] X. Wang and T. Long. Bacterial chemotaxis toward a NAPL source within a pore-scale microfluidic chamber. *Biotechnology and Bioengineering*, 109(7):1622–1628, July 2012.

[56] Z Wang. Mathematics of traveling waves in chemotaxis–review paper. *Discrete and Continuous Dynamical Systems Series B*, 18(3):601–604, May 2013.

[57] M.T. Widman, D. Emerson, C.C. Chiu, and R.M. Worden. Modeling microbial chemotaxis in a diffusion gradient chamber. *Biotechnology and Bioengineering*, 55 (1):191–205, July 1997.

[58] Z. Yan, E. Bouwer, and M. Hilpert. Coupled effects of chemotaxis and growth on

traveling bacterial waves. *Journal of Contaminant Hydrology*, 164:138–152, June 2014.

Chapter 3. Coupled Effects of Chemotaxis and Growth on Traveling Bacterial Waves

3.1 Abstract

Traveling bacterial waves are capable of improving contaminant remediation in the subsurface. It is fairly well understood how bacterial chemotaxis and growth separately affect the formation and propagation of such waves. However, their interaction is not well understood. We therefore perform a modeling study to investigate the coupled effects of chemotaxis and growth on bacterial migration, and examine their effects on contaminant remediation. We study the waves by using different initial electron acceptor concentrations for different bacteria and substrate systems. Three types of traveling waves can occur: a chemotactic wave due to the biased movement of chemotactic bacteria resulting from metabolism-generated substrate concentration gradients; a growth/decay/motility wave due to a dynamic equilibrium between bacterial growth, decay and random motility; and an integrated wave due to the interaction between bacterial chemotaxis and growth. Chemotaxis hardly enhances the bacterial propagation if it is too weak to form a chemo-

This paper has been published (Yan Z., Bouwer E. and Hilpert M., *Journal of Contaminant Hydrology*, 164:138-152, 2014 Aug.)

tactic wave or its wave speed is less than half of the growth/decay/motility wave speed. However, chemotaxis significantly accelerates bacterial propagation once its wave speed exceeds the growth/decay/motility wave speed. When convection occurs, it speeds up the growth/decay/motility wave but slows down or even eliminates the chemotactic wave due to the dispersion. Bacterial survival proves particularly important for bacterial propagation. Therefore we develop a conceptual model to estimate the speed of growth/decay/motility waves.

3.2 Introduction

Groundwater pollution is a critical concern to public health. In 2004, the US EPA reported that approximately 294,000 contaminated field sites were in need of remediation [2]. A major challenge is to clean up the large number of aquifers contaminated by organic pollutants. Conventional cleanup technologies, such as pump-and-treat, are time consuming and expensive. Biodegradation, contaminant mass decrease through microbial activity without excavating contaminated samples, has increased in popularity as an alternative treatment due to its effectiveness and cost efficiency. Among all remediation projects, about one in four makes use of *in situ* bioremediation [22, 7, 38].

Bioremediation is difficult to predict because many biotic factors (inoculum density and size, preinduction, cell immobilization, adaptation of degradative microorganism towards environmental stresses) and abiotic factors (pH, temperature, concentration of target pollutants and cross-contamination by other non-targeted pollutants, moisture content,

nutrient availability, volatilization, sorption and desorption) are usually not quantifiable [38]. Many studies have shown that bacterial survival is one of the most important biotic factors determining the applicability and sustainability of *in situ* bioremediation [26, 27, 21]. Among all the abiotic factors, bioavailability has been identified as a major limitation to bioremediation efficiency because microorganisms tend to be present in zones with high hydraulic conductivity and leave behind contaminant sources in regions with fairly low conductivity [4].

Random motility and chemotaxis are two common cell motion mechanisms [24, 33]. The former gives rise to diffusive behavior at the population scale, while the latter enables motile bacteria to sense chemical gradients in their surrounding environment and to move toward regions with high chemical concentration [5]. Chemotaxis has been reported to increase the bioavailability of pollutants and to improve their removal in aqueous environments [14, 46, 34, 17]. A large number of harmful chemicals (e.g., toluene, benzene, naphthalene, polycyclic aromatic hydrocarbons, and trichloroethylene) have been found to be chemoattractants for various bacterial strains [35, 39, 37, 36, 52].

Traveling bacterial waves can promote the removal of contaminants [32]. These waves can be formed by traveling bacterial bands, i.e., populations of bacteria with a concentration peak [19], or waves that involve propagating fronts, with a concentration plateau behind this front [33]. Adler [1] first observed the formation of traveling bands of chemotactic bacteria in capillary tubes. Bands of *E. coli* formed due to metabolism-generated gradients in the concentration of organic nutrients and oxygen, and moved at a speed of

several mm/h. Afterward, much research examined how chemotaxis produced such bands, but bacterial growth and decay were usually ignored [41, 30, 31]. However, Kennedy and Aris [24] found that a bacterial band could be formed in the absence of chemotaxis, due to the balance of growth, death and random motility, and the band speed could be increased by the additional action of chemotaxis. Lauffenburger et al. [28] investigated the effects of chemotaxis on bacterial movement in the presence of growth and death by using different functional forms of chemotactic sensitivity. They proposed two types of traveling bands: 1) growth/death/motility band; and 2) pure chemotactic band. Regardless of bacterial decay, Funaki et al. [12] and Mansour [33] studied traveling wave fronts by combining simplified chemotaxis and growth models. However, the coupled effects of chemotaxis and growth on the formation and migration of waves are still not well understood. We address this issue in the present study.

Another significant factor influencing bacterial survival and contaminant bioremediation is electron acceptor concentration. However, most chemotaxis-related research assumed that electron acceptor was in excess and not a rate-limiting compound. One exception is the study by Law [29], who found that low oxygen concentration could decrease naphthalene removal by reducing the naphthalene degradation rate and hence inhibiting chemotaxis toward the naphthalene source. This factor probably inhibits contaminant degradation in the subsurface, where the electron acceptor availability is typically limited.

The microbial process of biodegradation in subsurface environments is complicated. A realistic biodegradation model requires one to take into account the electron acceptor

concentration and to study chemotaxis together with growth and decay. In this paper, we investigate the coupled effects of chemotaxis and growth on the formation and propagation of bacterial waves, and examine their impacts on contaminant remediation. The influences of electron acceptor concentration and groundwater flow are examined in order to provide more realistic implications to contaminant remediation in natural subsurface environments.

3.3 Mathematical model

Reactive transport of chemotactic bacteria and dissolved chemicals in the subsurface can be described by partial differential equations that are based on mass balance equations [23, 20, 18]. In this work, we consider a system in which both substrate and electron acceptor are rate-limiting chemicals. The reaction between the bacteria and the substrate is described by a double-Monod kinetics model [44]. The resulting PDEs are given by

$$\frac{\partial b}{\partial t} + \vec{\nabla} \cdot \left[b(\vec{v} + \frac{\vec{v}_c}{\tau}) - D_b \vec{\nabla} b \right] = Y q_s \frac{s}{s + k_s} \frac{e}{e + k_e} b - kb \tag{3.1}$$

$$\frac{\partial s}{\partial t} + \vec{\nabla} \cdot (s\vec{v} - D_s \vec{\nabla} s) = -q_s \frac{s}{s + k_s} \frac{e}{e + k_e} b \tag{3.2}$$

$$\frac{\partial e}{\partial t} + \vec{\nabla} \cdot (e\vec{v} - D_e \vec{\nabla} e) = -q_e \frac{e}{e + k_e} \frac{s}{s + k_s} b \tag{3.3}$$

where b is the bacterial concentration, s is the substrate concentration, e is the electron acceptor concentration, $\vec{v}$ is the average pore water velocity, $\vec{v}_c$ is the chemotactic velocity, D_b is the effective dispersion coefficient of bacteria, D_s is the effective dispersion

coefficient of substrate, D_e is the effective dispersion coefficient of electron acceptor, τ is the tortuosity of porous medium, Y is the yield coefficient, k is the decay rate, q_s is the maximum reaction rate of substrate, q_e is the maximum reaction rate of electron acceptor, k_s is the half-saturation coefficient of substrate, and k_e is the half-saturation coefficient of electron acceptor. The chemotactic velocity $\vec{v_c}$ is assumed to depend on the substrate concentration and its gradient, and can be described by the model derived by Rivero et al. [45],

$$\vec{v_c} = \frac{2v_s}{3} \tanh\left(\frac{\chi_0}{2v_s}\frac{K_d}{(K_d+s)^2}|\vec{\nabla}s|\right)\frac{\vec{\nabla}s}{|\vec{\nabla}s|} \tag{3.4}$$

where v_s is the bacterial swimming speed, K_d is a dissociation constant, and χ_0 is the chemotactic sensitivity coefficient. This model predicts chemotactic transport of a bacterial population from the properties of individual bacteria and the concentration distribution of the substrate. χ_0 is usually estimated by fitting to experimental data. For a bacteria/substrate system without chemotaxis, $\chi_0 = 0$.

We attempted to define three bacteria/substrate model systems that are representative of real systems. These three model systems represent some of the diversity of real subsurface bacterial systems that are relevant to the biodegradation of environmental pollutants. We emphasize, however, that the model systems by no means cover the vast parameter space of the real systems. We have chosen bacterial strains that degrade organic pollutants:

- The first two bacterial strains, *P. putida* G7 and *P. putida* F1, exhibit chemotaxis to-

ward naphthalene and toluene, respectively, and metabolize these substances under aerobic conditions [41, 52].

- The other bacterial strain, *Azoarcus tolulyticus*, can degrade toluene under nitrate-reducing conditions; however, it is not known to exhibit chemotaxis [10].

We used the literature in order to come up with meaningful parameterizations for these three systems. Table 3.1 presents the parameter values. b_0, s_0 and e_0 are the initial concentrations of bacteria, substrate, and electron acceptor, respectively. D_{mb} is the random motility coefficient of bacteria, D_{ms} is the molecular diffusion coefficient of substrate, and D_{me} is the molecular diffusion coefficient of electron acceptor. For each system, most parameters were obtained from a single study; however, some parameters needed as modeling input were not reported, therefore we have to estimate them.

For the *P. putida* G7/naphthalene system, Pedit et al. [41] provided most parameter values except those related to bacterial growth/decay and oxygen consumption. In Pedit et al. [41]'s experiments, cell mass was measured in units of colony-forming-units (CFU) instead of milligram that we use. To convert the units, we assumed the equivalent sphere diameter of *P. putida* G7 to be 2.2 μm [50] and its density to be 1 g/cm^3. Therefore 1 CFU $= 5.57\times10^{-9}$ mg. In this study, we take into account bacterial growth/decay and oxygen consumption, and select k and Y from Ahn et al. [3]. To derive the stoichiometry of the bacterial metabolism, we have to estimate the dry weight of bacteria according to their wet weight. One usually assumes the water content of a bacterium to be 70%, which yields $Y = 0.538$ mg dry weight cells/mg naph based on $Y = 1.79$ mg wet weight

Table 3.1: Parameter values for the three bacteria/substrate model systems. Symbol "-" means no experimental reference.

Symbol	*P. putida* G7 /naphthalene [a]	*P. putida* F1 /toluene [f]	*Azoarcus tolulyticus* /toluene [j]
b_0 mg/L	22.3	2	200 [k]
s_0 mg/L	28.3	40	40 [k]
e_0 mg/L	–	–	–
D_{mb} cm^2/s	3.2 $\times 10^{-7}$	3.2 $\times 10^{-6}$ [g]	3.2 $\times 10^{-7}$ [l]
D_{ms} cm$^2/s$	7.5 $\times 10^{-6}$	9 $\times 10^{-6}$ [h]	9 $\times 10^{-6}$ [h]
D_{me} cm^2/s	2 $\times 10^{-5}$ [b]	2 $\times 10^{-5}$ [b]	1.8 $\times 10^{-5}$ [m]
q_s mg substrate/mg cell-s	1.42 $\times 10^{-4}$	1.87 $\times 10^{-4}$	2.15 $\times 10^{-5}$
q_e mg electron acceptors/mg cell-s	3.2 $\times 10^{-4}$ [c]	2.6 $\times 10^{-4}$ [c]	1.45 $\times 10^{-4}$
Y mg cell/mg substrate	1.79 [d]	1.28	5.3
k s^{-1}	1.66$\times 10^{-5}$ [d]	5.78$\times 10^{-5}$ [i]	–
K_d mg/L	2.1	92 [g]	–
k_s mg/L	0.5 [e]	13.8	51.5
k_e mg/L	0.4 [e]	0.4 [e]	93
χ_0 cm^2/s	1.8$\times 10^{-5}$	5$\times 10^{-6}$ [g]	–
v_s cm/s	4.8 $\times 10^{-3}$	4.4 $\times 10^{-3}$ [g]	4.8 $\times 10^{-3}$ [l]

cells/mg naph. Oxygen consumption by bacterial decay is neglected. Therefore, in light of Y, the stoichiometry can be expressed by

$$C_{10}H_8 + 9O_2 + 0.6NH_3 \longrightarrow 0.6C_5H_7O_2N + 7CO_2 + 2.8H_2O \tag{3.5}$$

On a mass basis, the maximum rate of oxygen consumption is 2.25 times that of the substrate, $q_e = 2.25q_s$. The value of D_{me} is from Han and Bartels [15], k_s and k_e are

from Law [29].

For the *P. putida* F1/toluene system, the biodegradation kinetics were studied by Reardon and Mosteller [42], while Wang and Long [52] estimated parameter values for chemotaxis. However, these studies did not report oxygen consumption. We consider the impact of oxygen concentration and use the k_e value of the *P. putida* G7/naphthalene system. The value of D_{ms} is from Schwarzenbach et al. [47], and k is from Singh and Olson [48]. Neglecting the oxygen consumption by bacterial decay, we derived the stoichiometry from Y,

$$C_7H_8 + 4O_2 + NH_4^+ \longrightarrow C_5H_7O_2N + 2CO_2 + 2H_2O + H^+ \tag{3.6}$$

Therefore $q_e = 1.39q_s$.

For the *Azoarcus tolulyticus*/toluene system, we assumed that nitrate is reduced to nitrite and that bacterial growth and substrate biodegradation are not inhibited by nitrite. The same initial substrate concentration is used as for the *P. putida* F1/toluene system. However, we increased the initial bacterial concentration by 100-fold, because the reaction rate in the *Azoarcus tolulyticus*/toluene system is much smaller than in the *P. putida*

[a] Most parameter values are from Pedit et al. [41]. Exceptions are indicated.
[b] From Han and Bartels [15]
[c] Derived from Y and q_s
[d] From Ahn et al. [3]
[e] From Law [29]
[f] Most parameter values are from Reardon and Mosteller [42]. Exceptions are indicated.
[g] From Schwarzenbach et al. [47]
[h] From Wang and Long [52]
[i] From Singh and Olson [48]
[j] Most parameter values are from Elmen et al. [10]. Exceptions are indicated.
[k] Selected by authors to ensure waves formation
[l] From Hashitani and Tanaka [16]
[m] Assumed the same as *P. putida* G7

F1/toluene system. We assumed that *Azoarcus tolulyticus* had the same random motility coefficient and swimming speed as *P. putida* G7. The value of D_{me} is from Hashitani and Tanaka [16], and all other parameter values are from Elmen et al. [10]. We do not use the stoichiometry to estimate q_e from q_s because both of them were given by Elmen et al. [10].

Since the parameter values in Table 3.1 were attained in a stagnant solution ($v = 0$), we first investigated the coupled effects of chemotaxis and growth on traveling bacterial waves without convection. When $v = 0$, $D_b = D_{mb}/\tau$, $D_s = D_{ms}/\tau$, and $D_e = D_{me}/\tau$. We selected τ as 2.2 given by Pedit et al. [41]. Bioremediation for the three bacteria/substrate systems is simulated in a one-dimensional domain with a wall on its left end. The length of the domain is 100 mm, and the numerical grid spacing, Δl, is 0.04 mm. At the beginning of simulations, the substrate and the electron acceptor were distributed uniformly with concentrations s_0 and e_0, respectively. A 10 mm long bacterial slug with concentration b_0 was initially present on the left side. No-flux boundary conditions were used. The concentration profiles normalized by the initial concentrations are shown in Figure 3.1a.

When convection occurs, we estimate the effective dispersion coefficient $D_\star$ ($\star$ denotes b, s, or e) in terms of random motility or molecular diffusion coefficient $D_{m\star}$ and Peclet number $Pe_{m\star} = vd/D_{m\star}$, where d is the median diameter of grains in porous media [8]. In our simulations, we selected d as 50 μm given by Pedit et al. [41]. When $Pe_{m\star} < 5$, $D_\star = D_{m\star}/\tau$, the dispersion caused by shear flow can be ignored. When $5 < Pe_{m\star} < 300$, $D_\star = (1/\tau + 0.5Pe_{m\star}^{1.2})\times D_{m\star}$, the dispersion increases with average pore water velocity.

We modify the initial conditions and boundary conditions for the convection situation. A slug of bacteria was initially injected into a region ranging from 95 mm to 105 mm in a one-dimensional domain with 200 mm length (see Figure 3.1b). The substrate and oxygen were uniformly distributed everywhere. Periodic boundary conditions were applied.

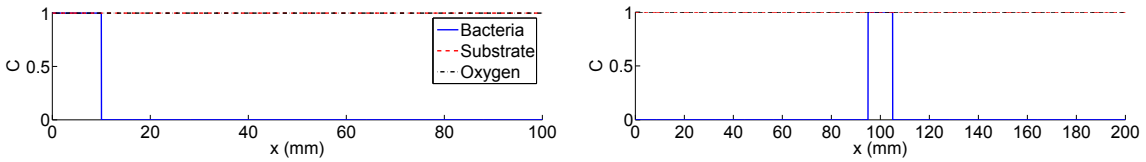

(a) (b)

Figure 3.1: Normalized concentration profiles at the beginning of simulations for the cases of (a) no convection, and (b) with convection.

The lattice-Boltzmann method was used to simulate the bacteria and substrate systems; details of this numerical method are given in the Appendix. Long and Hilpert [32] have validated this method by comparing simulating results with experiments by Pedit et al. [41]. In these experiments, capillary tubes being filled with naphthalene solution were dipped into a reservoir containing a bacterial suspension, which entered the tube to form a traveling band. The simulation results agreed well with the experiments, in which the number of cells that accumulated in the tube was measured as a function of time. More details about the validation procedure can be found in Long and Hilpert [32].

3.4 Simulation results

3.4.1 Effects of electron acceptor concentration on bacterial propagation and substrate degradation

We investigate the impact of electron acceptor concentration on bacterial propagation and substrate degradation. Specifically, we evaluate the effects of the presence and absence of chemotaxis and growth/decay for the *P. putida* G7/naphthalene and *P. putida* F1/toluene systems. In this analysis, we consider the growth rate Yq_s and the chemotactic sensitivity coefficient χ_0 as mathematically independent variables, even though chemotaxis and growth can be linked biologically. This is because a cell's chemotactic response can be triggered either by uptake and metabolism of the chemical stimulus or by metabolism-independent sensing [49]. Additionally, considering Yq_s and χ_0 as independent variables makes it possible to build appropriate mathematical models and quantitatively study their effects on bacterial propagation. The *Azoarcus tolulyticus*/toluene system is not examined because *Azoarcus tolulyticus* exerts no chemotaxis toward toluene.

3.4.1.1 P. putida G7/naphthalene

To estimate the impact of electron acceptor concentration on the bioremediation of naphthalene by *P. putida* G7, we studied four different initial oxygen concentrations: e_0 = 11.3 mg/L, the saturated solubility of atmospheric oxygen in fresh water at 10°C; e_0 = 53.8 mg/L, the saturated solubility of pure oxygen in fresh water at 10°C; e_0 =

113 mg/L, an oversaturated oxygen concentration; and $e_0 = 1.0$ mg/L, a more realistic oxygen concentration in natural subsurface environments. For each oxygen concentration, three cases were simulated: (a) with chemotaxis but without growth/decay ($\chi_0 > 0$; Y, $k = 0$); (b) with growth/decay but without chemotaxis (Y, $k > 0$; $\chi_0 = 0$); and (c) with chemotaxis and with growth/decay ($\chi_0 > 0$; Y, $k > 0$). The random motility coefficient $D_{mb} > 0$ in all three cases.

3.4.1.1.1 Initial oxygen concentration e_0 = 11.3 mg/L

Figure 3.2a-c show the simulated concentration profiles 46.1 hours after the bacterial slug was introduced into the domain for the three cases. Oxygen is depleted quickly after the bacteria move through. Traveling bands are observed once bacterial growth/decay occurs. Like Lauffenburger et al. [28], we name the band, which occurs in the absence of chemotaxis ($Y, k > 0$; $\chi_0 = 0$), a growth/decay/motility band. We call a band, which occurs in the presence of both chemotaxis and growth/decay ($\chi_0 > 0$; $Y, k > 0$), an integrated band. No band is observed if chemotaxis is the only driving mechanism ($\chi_0 > 0$; $Y, k = 0$). This is surprising because one would expect chemotaxis to produce biased movement and result in greater net bacterial migration than bacterial growth, which by itself is not a mechanism for bacterial motion. Figure 3.2d shows the location of the bacterial peak, x, as a function of time, t, for the two cases $Y, k > 0; \chi_0 = 0$ and $\chi_0 >; Y, k > 0$. In both cases, the slopes of the $x(t)$ curve approach the same constant value 0.4 mm/h, which is the steady-state speed of the traveling bacterial bands. We

also calculated the overall percentage of removed substrate in the whole domain. 4.7% of all substrate is consumed in the case $\chi_0 > 0;\ Y,\ k = 0$, while 6% is consumed in the two cases $Y, k > 0; \chi_0 = 0$ and $\chi_0 >; Y, k > 0$. The results illustrate that the formation of a traveling wave facilitates the removal of substrate, and chemotaxis minimally affects bacterial movement and substrate degradation when $e_0 = 11.3$ mg/L.

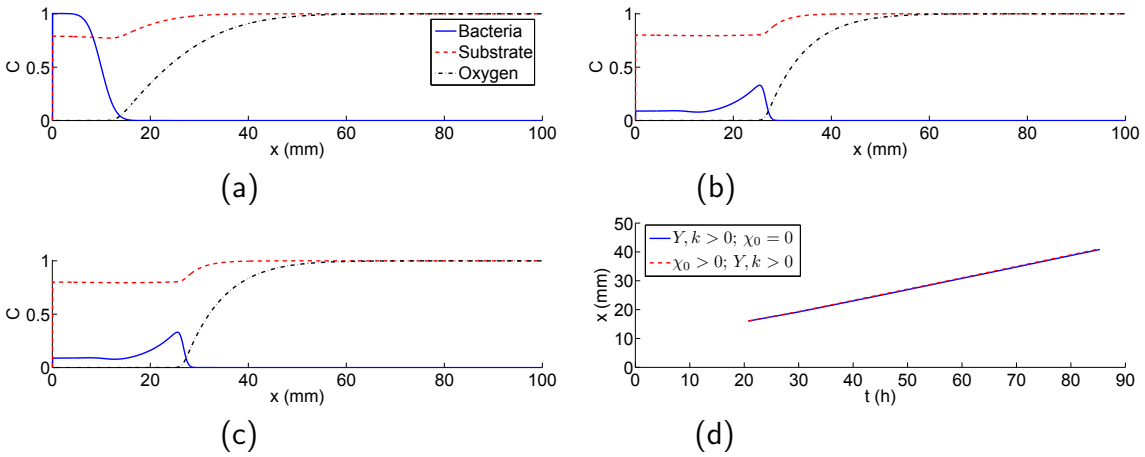

Figure 3.2: Normalized concentration profiles 46.1 hours after a slug of *P. putida* G7 was introduced into a domain containing uniformly distributed naphthalene and oxygen: (a) with chemotaxis but without growth/decay ($\chi_0 > 0;\ Y,\ k = 0$); (b) with growth/decay but without chemotaxis ($Y,\ k > 0;\ \chi_0 = 0$); and (c) with chemotaxis and with growth/decay ($\chi_0 > 0;\ Y,\ k > 0$). (d) Location of bacterial peak in (b) and (c) as a function of time. The initial oxygen concentration is $e_0 = 11.3$ mg/L.

We also calculated the total number of bacteria inside the traveling band, which only included the bacteria ahead of the bacterial concentration minimum that is located immediately behind the bacterial peak, as a function of time for the case $Y, k > 0; \chi_0 = 0$. The result shows that this total number first increases and then approaches a constant value, which means that the bacteria eventually reach a dynamic equilibrium between bacterial growth, decay and diffusion. However, the speed of this growth/decay/motility band be-

comes nearly constant before the equilibrium is achieved, and this speed is independent of the total amount of the bacteria inside the band. This finding is different from traveling bands caused by chemotaxis, where the band speed increases with the total number of bacteria inside the band [31]. When the random motility is the only transport mechanism ($\chi_0 = 0; Y, k = 0$), the bacteria diffuse from regions with high concentration to those with low concentration (results not shown). The bacterial population does not move with a constant speed, because the transport is diffusion limited, which significantly decreases the effectiveness of a bioremediation action.

During the process of forming a growth/decay/motility band, the bacteria diffuse to the right into previously unoccupied areas due to their random motility. They grow due to substrate consumption and experience simultaneously decay. Here we try to develop an understanding of this process by considering a point P in the unoccupied area. When the bacteria arrive at P, the growth rate is larger than the decay rate because enough electron donor and acceptor are available; hence the bacterial concentration at P increases. As the electron donor and acceptor concentrations decrease, the growth rate decreases but the decay rate remains unchanged. The bacterial population keeps increasing if the growth rate is still larger than the decay rate. Once the two rates become the same, the bacterial concentration at P reaches a maximum. Afterward, as the electron donor and acceptor concentrations further decrease, the decay rate exceeds the growth rate, and the bacterial concentration decreases. This process is repeated over and over again at points ahead of P. As a result, the location of the maximum bacterial concentration propagates, and a

traveling bacterial band forms.

3.4.1.1.2 Higher initial oxygen concentration e_0 = 53.8 mg/L

Pure oxygen can be injected into the subsurface in order to promote biodegradation of organic compounds. Figure 3.3a-c show the simulated concentration profiles 46.1 hours after the bacterial slug was introduced into the domain for the three cases. Traveling bacterial bands are observed in all cases. Like in Lauffenburger et al. [28], we define the band in the case Y, $k = 0$; $\chi_0 > 0$ as a chemotactic band. The amount of oxygen is still not enough to degrade all of the substrate.

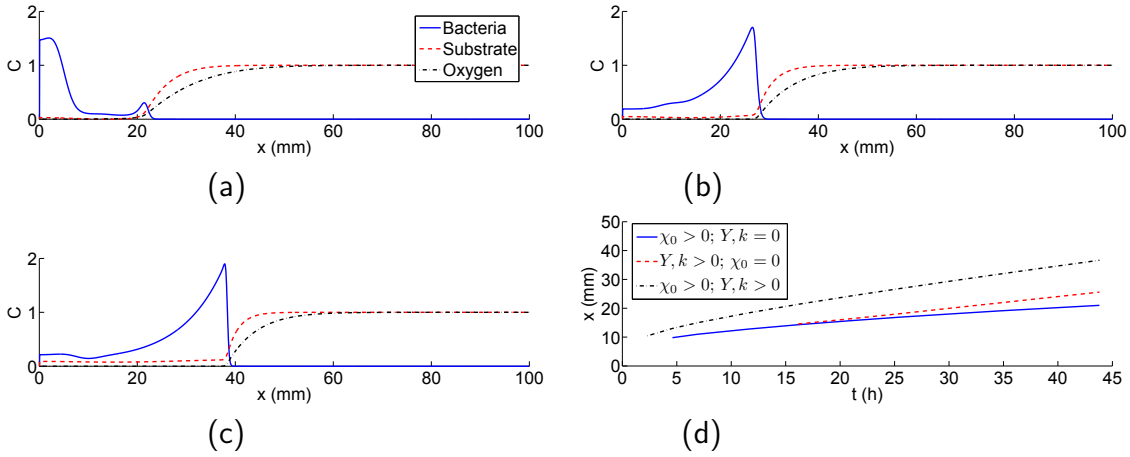

Figure 3.3: Normalized concentration profiles 46.1 hours after a slug of *P. putida* G7 was introduced into a domain containing uniformly distributed naphthalene and oxygen: (a) with chemotaxis but without growth/decay ($\chi_0 > 0$; Y, $k = 0$); (b) with growth/decay but without chemotaxis (Y, $k > 0$; $\chi_0 = 0$); and (c) with chemotaxis and with growth/decay ($\chi_0 > 0$; Y, $k > 0$). (d) Location of bacterial peak in (a-c) as a function of time. The initial oxygen concentration is $e_0 = 53.8$ mg/L.

Figure 3.3d presents the location of the bacterial peak as a function of time for all three types of bands. The growth/decay/motility band moves with a constant velocity, $v_{gb} = 0.4$

mm/h. However, the speeds of the chemotactic band, v_{cb}, and the integrated band, v_{ib}, decrease gradually from initial values 0.5 mm/h and 1.11 mm/h, respectively. The latter band eventually reaches a dynamic equilibrium and moves at a speed of 0.52 mm/h, while the former band finally disappears. Although the higher initial oxygen concentration does not change the speed of the growth/decay/motility band, it enables bacteria to form a chemotactic band and promotes the bacterial migration, since the integrated band moves faster than the growth/decay/motility band. The percentage of removed substrate in Figures 3.3a, b, and c are 25.2%, 29%, and 36.7%, respectively. The results demonstrate that the removal efficiency of substrate is proportional to distance traveled by the bacterial bands.

In contrast to $e_0 = 11.3$ mg/L, where chemotaxis minimally affects the bacterial movement, chemotaxis increases the bacterial propagation in the case of $e_0 = 53.8$ mg/L, especially when the integrated band is initially formed. This difference probably results from different dominant mechanisms of bacterial motion: chemotaxis and random motility. If chemotaxis dominates, it improves the bacterial propagation driven originally by random motility and growth, which is the case of $e_0 = 53.8$ mg/L. If random motility dominates, chemotaxis is too weak to affect the bacterial movement, which is the case of $e_0 = 11.3$ mg/L.

Long and Hilpert [31] derived a dimensionless parameter to judge whether chemotactic bacteria can form a band (neglecting bacterial growth/decay and substrate diffusion). This parameter compares the actions between bacterial chemotaxis and random motility. When

the biased motion due to chemotaxis overcomes the diffusion-like motion due to random motility, a band forms. However, this criterion becomes invalid here because bacterial growth and decay occur. Not only chemotaxis improves the bacterial propagation driven originally by bacterial random motility and growth, but bacterial growth also accelerates the bacterial movement driven originally by chemotaxis. This interaction makes predicting the formation of a band and calculating its speed complicated. Further discussions of the interaction between chemotaxis and growth will be presented in later sections.

3.4.1.1.3 Highest initial oxygen concentration e_0 = 113 mg/L

We also considered a very high initial oxygen concentration, $e_0 = 113$ mg/L, which allows for complete substrate degradation. Hydrogen peroxide is usually used to achieve such oversaturated oxygen conditions during *in situ* biodegradation [40]. The ability of hydrogen peroxide to inhibit bacterial growth is neglected due to the relatively high cell density and the relatively low concentration of hydrogen peroxide needed in our study [40].

Figure 3.4a-c show the simulated concentration profiles 46.1 hours after the bacterial slug was introduced into the domain for different cases. Traveling bacterial bands are observed in all cases. Behind the bands, all substrate is degraded, and about half of the oxygen remains. When the oxygen is in excess, the substrate is consumed quickly and generates a large gradient of concentration. Consequently, the portion of bacteria, which are located inside the region holding this large gradient, exhibits a fast chemotactic

velocity and moves quickly toward regions with higher substrate concentration. Since this portion of bacteria is exposed to more electron acceptor and donor than other bacteria, they grow much faster than others. This is why the bacteria in Figure 3.4c form a sharp band with a large maximum concentration. If chemotaxis is not strong enough to form such a portion of fast moving bacteria, all bacteria experience the same diffusion, growth and decay. Therefore no sharp band occurs, which is the case in Figure 3.3c.

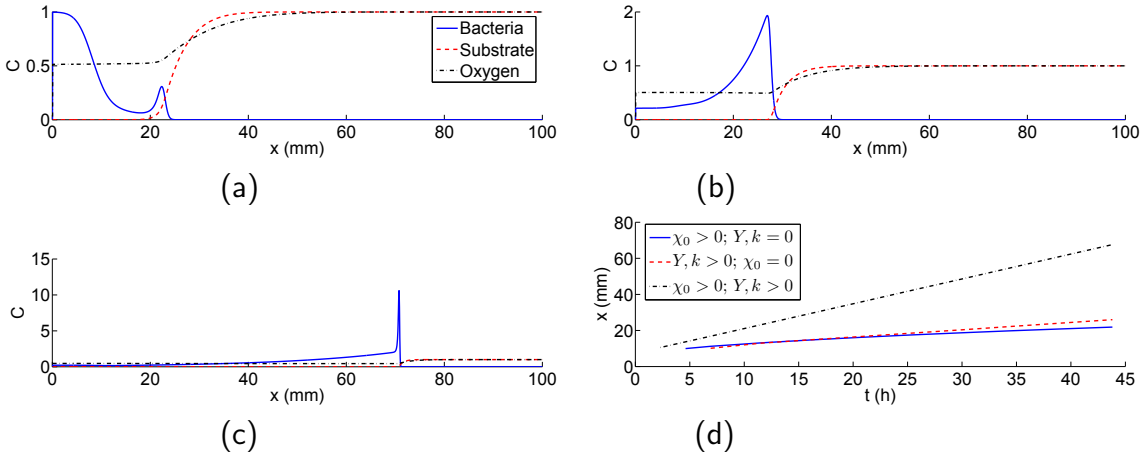

Figure 3.4: Normalized concentration profiles 46.1 hours after a slug of *P. putida* G7 was introduced into a domain containing uniformly distributed naphthalene and oxygen: (a) with chemotaxis but without growth/decay ($\chi_0 > 0$; Y, $k = 0$); (b) with growth/decay but without chemotaxis (Y, $k > 0$; $\chi_0 = 0$); and (c) with chemotaxis and with growth/decay ($\chi_0 > 0$; Y, $k > 0$). (d) Location of bacterial peak in (a-c) as a function of time. The initial oxygen concentration is $e_0 = 113$ mg/L.

Figure 3.4d presents the location of the bacterial peaks as a function of time for the three types of bands. The speeds of the growth/decay/motility band, v_{ib}, and the integrated band, v_{gb}, are both constant ($v_{ib} = 0.4$ mm/h and $v_{gb} = 1.38$ mm/h). The process of bacterial growth, decay, random motility and chemotaxis reaches a dynamic equilibrium shortly after the integrated band is formed. The speed of the chemotactic

band decreases gradually from an initial value of 0.54 mm/h. Although the excessive oxygen does not change the speed of the growth/decay/motility band and only slightly increases the chemotactic band speed, it strongly increases the integrated band speed. The latter, v_{ib}, is much larger than the sum of v_{cb} and v_{gb} due to the interaction between bacterial chemotaxis and growth, which will be further explained later.

3.4.1.1.4 Lower initial oxygen concentration e_0 = 1.0 mg/L

In the subsurface, the oxygen concentration is usually far below the solubility of oxygen because of the relatively slow rate of re-aeration and significant biological oxygen demand. We therefore examine a lower initial oxygen concentration, $e_0 = 1.0$ mg/L. The concentration distributions of bacteria, substrate, and oxygen are similar to these shown in Figure 3.2, except that more bacteria decay quickly and less substrate is degraded. Small bands are still observed when growth/decay occurs ($Y, k > 0$), and their speeds are 0.3 mm/h. Therefore, limitations in electron acceptor availability slow down the growth/decay/motility band. A sufficiently high initial electron acceptor concentration is required for essential bacterial survival and contaminant degradation.

3.4.1.1.5 Wave speed as a function of the initial oxygen concentration

To further examine the effect of oxygen on bacterial propagation, we performed simulations for additional intermediate initial oxygen concentrations e_0, and determined the three different band speeds, v_{cb}, v_{gb}, and v_{ib}, as a function of e_0. The simulation results

reveal five different regimes (see Figure 3.5). If $e_0 \leq 11.3$ mg/L, v_{gb} increases with e_0, and chemotaxis is too weak to result in a band. As a result, v_{ib} has about the same speed as v_{gb}. For 11.3 $< e_0 \leq 40$ mg/L, v_{gb} remains nearly constant, and chemotaxis begins to promote bacterial propagation but is not strong enough to result in a band. Hence v_{ib} increases with e_0 only slightly. For 40 $< e_0 \leq 60$ mg/L, v_{gb} still does not change significantly, while v_{cb} increases quickly. Consequently, v_{ib} increases rapidly with e_0. For 60 $< e_0 \leq 80$ mg/L, v_{ib} increases rapidly, although both v_{gb} and v_{cb} remain essentially unchanged. Note that $e_0 = 63.7$ mg/L is the critical value for all substrate being consumed according to the stoichiometry Eq. (3.5). During this transition from insufficient oxygen to excessive oxygen for complete substrate degradation, a larger e_0 causes more bacteria to grow and thus more substrate to be consumed, which results in a larger substrate gradient. Consequently, this larger gradient produces a larger chemotactic velocity as well as a faster traveling band. This faster band in turn assists the bacteria to access more substrate and grow more quickly. Such coupled effects between chemotaxis and growth make integrated bands move much faster than that expected if one naively assumed the integrated band speed to be the sum of the growth/decay/motility band speed and the chemotactic one. Indeed v_{ib} increases with e_0 even though both v_{gb} and v_{cb} do not change significantly with e_0. If $e_0 > 80$ mg/L, all v_{gb}, v_{cb} and v_{ib} remain unchanged, because the electron acceptor is not a limiting factor for the bacterial metabolism anymore. To sum up, injecting sufficient oxygen so that the bacteria can degrade all substrate is crucial for improving the removal efficiency of contaminants by means of chemotaxis. However,

too much oxygen is unnecessary, because complete substrate degradation requires only a finite amount of oxygen. A concentration that is slightly higher than the critical one for all substrate being consumed is a good choice.

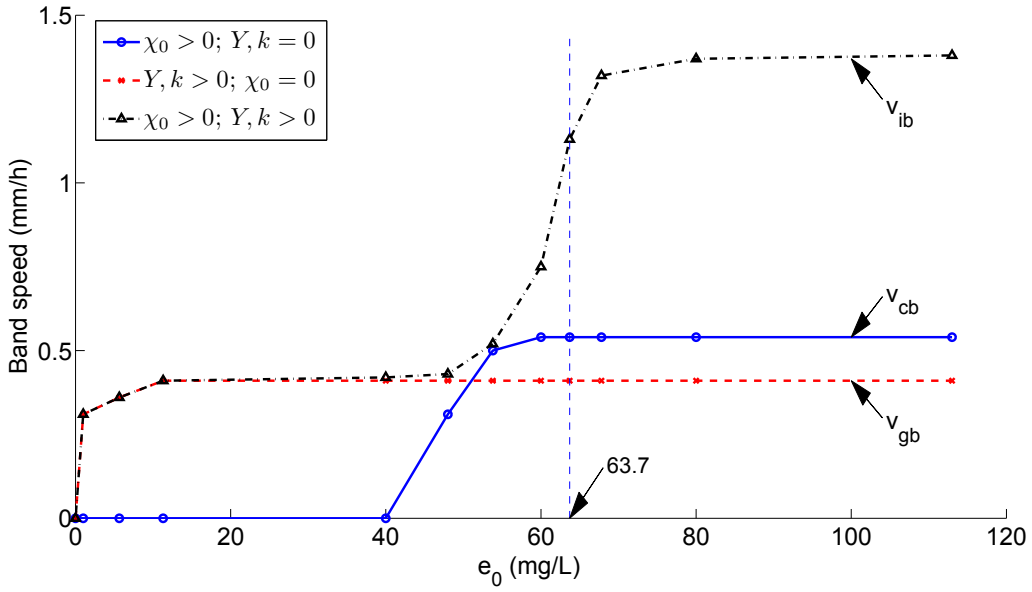

Figure 3.5: Speeds of three traveling bands as a function of initial oxygen concentration e_0 for the *P. putida* G7/naphthalene system. Note that $e_0 = 63.7$ mg/L is the critical value for all substrate being consumed.

Figure 3.5 illustrates that the speed of the growth/decay/motility band increases with e_0 only when e_0 is small. To further explore this dependence, we examined the speed of the growth/decay/motility band as a function of the half-saturation coefficient of the electron acceptor, k_e. The findings show that the band speed decreases with an increase in k_e, and the extent of decrease is much smaller for $e_0 = 53.8$ mg/L than for $e_0 = 11.3$ mg/L. Particularly, the band speed remains almost unchanged for $e_0 = 53.8$ mg/L when k_e is small. These results can be explained by Eq. (4.23), in which e_0 minimally changes the bacte-

rial growth rate, which significantly determines the speed of the growth/decay/motility band, if it is much larger than k_e. Otherwise, the bacterial growth rate increases with e_0. Therefore, the effects of e_0 on the growth/decay/motility band speed are dependent on the comparison of e_0 with k_e.

3.4.1.2 P. putida F1/toluene

In this section, the *P. putida* F1/toluene system is selected to study the bacterial propagation and contaminant degradation for different initial electron acceptor concentrations e_0. We found that more bacteria are produced and less substrate remains as e_0 increases. However, the bacterial distributions look similar for different e_0 values, and no chemotactic band is observed. Therefore, we only present the results for $e_0 = 113$ mg/L.

Figure 3.6a-c show the concentration distributions of bacteria, substrate, and oxygen 46.1 hours after a slug of *P. putida* F1 was introduced into the domain containing uniformly distributed toluene and oxygen. Traveling bands are observed for the cases $Y, k > 0; \chi_0 = 0$ and $\chi_0 > 0; Y, k > 0$. They have about the same speed 1.0 mm/h according to the slopes of the $x(t)$ curves in Figure 3.6d, a value that is larger than for the *P. putida* G7/naphthalene system under the same e_0 value. One possible explanation is that the random motility of *P. putida* F1, the dominant motion mechanism in this case, is ten times that of *P. putida* G7. All of the substrate is degraded behind the traveling bands. No traveling band is found in the case $\chi_0 > 0; Y, k = 0$, and chemotaxis hardly affects the bacterial movement. One possible reason is that the small χ_0 and the large K_d make

chemotaxis too weak to form a band. The finding is consistent with experimental results by Elmen et al. [10], who did not observe bands.

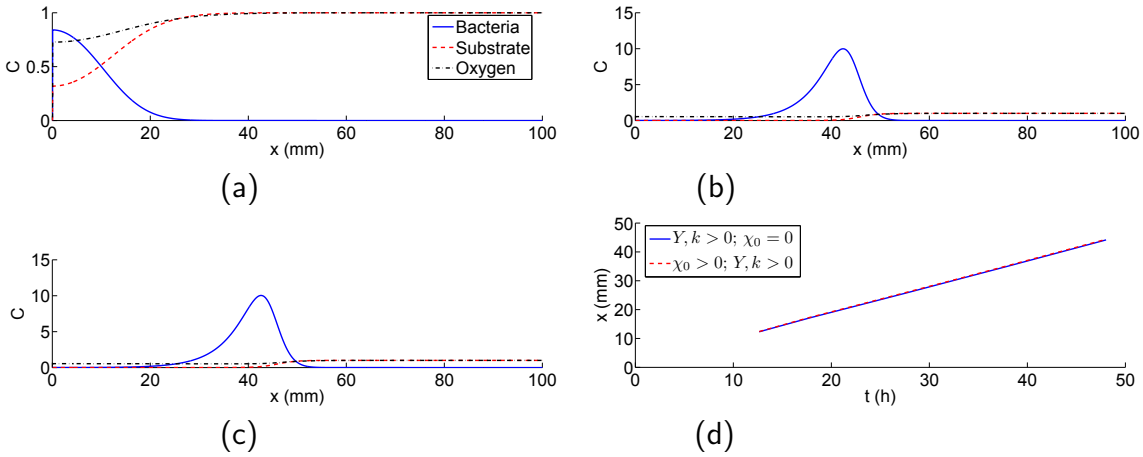

Figure 3.6: Normalized concentration profiles 46.1 hours after a slug of *P. putida* F1 was introduced into a domain containing uniformly distributed toluene and oxygen: (a) with chemotaxis but without growth/decay ($\chi_0 > 0$; Y, $k = 0$); (b) with growth/decay but without chemotaxis (Y, $k > 0$; $\chi_0 = 0$); and (c) with chemotaxis and with growth/decay ($\chi_0 > 0$; Y, $k > 0$). (d) Location of bacterial peak in (b) and (c) as a function of time. The initial oxygen concentration is $e_0 = 113$ mg/L.

3.4.2 The effects of chemotaxis on bacterial propagation in the presence of bacterial growth and decay

For the *P. putida* G7/naphthalene system, we have found that, in the presence of bacterial growth and decay, chemotaxis improves bacterial propagation as well as substrate degradation only if chemotaxis alone ($Y = k = 0$) is strong enough to develop a traveling band. It is reasonable to examine the sensitivity of bacterial migration to a change in χ_0, because χ_0 depends on the exact experimental conditions, e.g., buffer solution chemistry [35, 41], and can also be changed through genetic engineering, e.g., through

transfer of chemoreceptor genes [25]. To exclude the dependence on the electron acceptor concentration, we selected $e_0 = 113$ mg/L such that the electron acceptor is not a rate-limiting chemical.

Figure 3.7 shows the simulated speeds of chemotactic, growth/decay/motility, and integrated bands as a function of χ_0 for the *P. putida* G7/naphthalene system. The speed of the growth/decay/motility band is shown only for $\chi_0 = 0$, the condition for this type of band. The plot illustrates that both the chemotactic band speed, v_{cb}, and the integrated band speed, v_{ib}, increase with χ_0. When $\chi_0 \leq 2{\times}10^{-6}$ cm^2/s, v_{ib} is very close to v_{gb}, and v_{cb} is small compared to v_{gb}. This means that chemotaxis hardly improves bacterial movement when it is too weak to result in a chemotactic band or when the speed of that band is small compared to the growth/decay/motility band speed. When v_{cb} approaches about half of v_{gb}, chemotaxis begins to enhance bacterial propagation. Chemotaxis almost doubles v_{gb} when v_{cb} is close to v_{gb} (e.g., $v_{gb} = 0.4$ mm/h, $v_{cb} = 0.42$ mm/h, $v_{ib} = 0.94$ mm/h when $\chi_0 = 1.2{\times}10^{-5}$ cm^2/s). Afterward, v_{ib} increases quickly with χ_0 even though v_{cb} increases slowly. Therefore, chemotaxis barely enhances bacterial propagation until v_{cb} approaches half of v_{gb}, and significantly accelerates bacterial migration once v_{cb} exceeds v_{gb}. This conclusion is also valid for other initial electron acceptor concentrations, as shown in Figure 3.5.

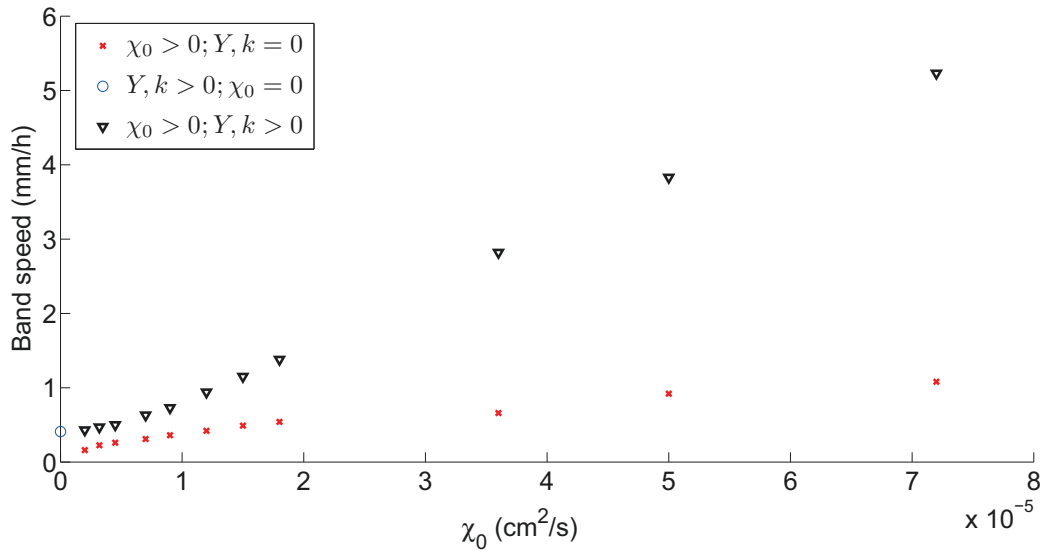

Figure 3.7: Speeds of the chemotactic band ($\chi_0 > 0; Y, k = 0$), the growth/decay/motility band ($Y, k > 0; \chi_0 = 0$), and the integrated band ($\chi_0 > 0; Y, k > 0$) as a function of chemotactic sensitivity coefficient χ_0 for the *P. putida* G7/naphthalene system.

3.4.3 Effects of convective velocity on bacterial propagation and substrate degradation

So far we have investigated bacterial migration without convection, which usually plays a significant role in microbial transport and contaminant remediation in groundwater. Here we study the effects of convective transport on bacterial propagation and substrate degradation. The *P. putida* G7/naphthalene system is chosen, because all three types of bacterial bands may occur for this system, as long as e_0 is large enough. An e_0 of 113 mg/L was selected to ensure the band formation. We choose three different convective velocities, v = 0, 1 and 50 mm/h, to examine the effect of convection.

We present the results for v = 1 and 50 mm/h in Figure 3.8. The concentration

profiles for $v = 0$ are the same as for $v = 1$ mm/h except that the bands do not move downstream as a whole (not shown). When $v = 1$ mm/h, the dispersion caused by convection is negligible and does not affect the formation of bacterial bands. Chemotaxis increases the bacterial movement. Two integrated bands, which move separately downstream and upstream, have faster speed than either the growth/decay/motility band or the chemotactic one. The downstream band migrates with 2.4 mm/h, and the upstream band moves against convection with -0.4 mm/h (- means moving upstream). This upstream band is of great significance in groundwater cleanup, because it enables microorganisms to remediate contaminants located in upstream areas. When $v = 50$ mm/h, convection plays a dominate role in bacterial transport and delivers bacteria far away from the injection location. Bacteria cannot generate a chemotactic band due to the strong dispersion, so chemotaxis fails to improve the bacterial propagation. However, the strong dispersion forces the bacteria to move around and enables the growth/decay/motility band to achieve a large speed. The growth/decay/motility band for $v = 50$ mm/h moves faster than the integrated band for $v = 1$ mm/h, and their relative speeds to flowing fluid are 2.6 mm/h and 1.4 mm/h, respectively. Therefore, convection improves bacterial migration and contaminant biodegradation, even though it weakens the effect of chemotaxis.

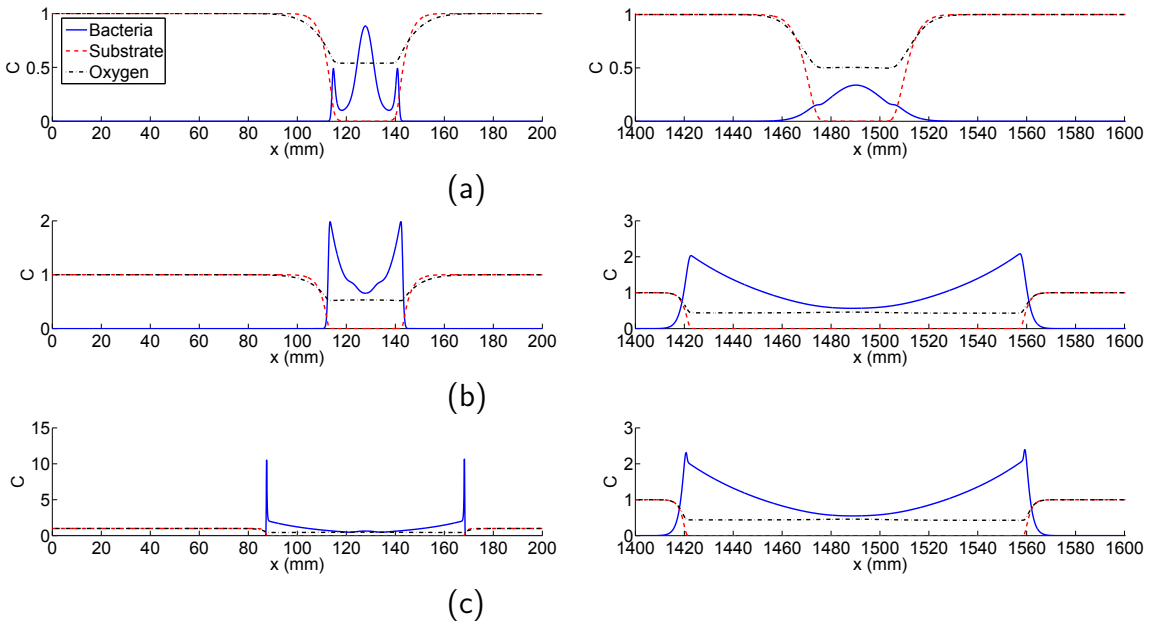

Figure 3.8: Normalized concentration profiles 27.7 hours after the slug of *P. putida* G7 was introduced into a domain containing uniformly distributed naphthalene and oxygen. The left figures and right ones show the distributions for $v = 1$ and 50 mm/h, respectively, for three different cases: (a) with chemotaxis but without growth/decay ($\chi_0 > 0$; Y, $k = 0$); (b) with growth/decay but without chemotaxis (Y, $k > 0$; $\chi_0 = 0$); and (c) with chemotaxis and with growth/decay ($\chi_0 > 0$; Y, $k > 0$).

3.4.4 Speed of growth/decay/motility waves in the absence of chemotaxis and convection

The previous simulations have shown that bacteria can form a traveling band in the absence of chemotaxis, due to the balance between growth, decay and random motility. In this section, we evaluate the quantitative relation between the speed of growth/decay/motility waves and various microbial factors: decay rate k, yield coefficient Y, maximum reaction rate of substrate q_s, and random motility coefficient of bacteria D_{mb}. The *Azoarcus tolulyticus*/toluene system, in which *Azoarcus tolulyticus* metabolize

toluene under nitrate-reducing condition [10], is examined. In the beginning, we chose the Maximum Contaminant Level (MCL) of nitrate in drinking water as the initial concentration of the electron acceptor, e_0 = 44.3 mg/L. We found that this concentration does not guarantee band formation for all investigated cases. Thus, we chose e_0 = 443 mg/L, which ensures that the bacteria form a band in each case. All parameter values, except the ones we varied, are listed in Table 3.1. The effects of different factors on the growth/decay/motility waves are evaluated as follows.

3.4.4.0.1 The impact of decay rate k

First we examine the effect of decay rate k on bacterial propagation and contaminant remediation. Figure 3.9 shows the simulated concentration profiles for four different k values. When k = 0, the bacteria form a traveling wave front, and all substrate is remediated behind this front. If the bacteria decay, a traveling band is observed (e.g., for $k = 5\times10^{-6}$ s^{-1}). When k is further increased, the total number of the bacteria inside the band decreases, and the maximum bacterial concentration decreases. The substrate remaining behind the band increases with k. Once k exceeds a certain value, all bacteria decay quickly, and no further substrate degradation occurs (e.g., $k = 5.78\times10^{-5}$ s^{-1}). Figure 3.10a presents the positions of the wave front (for k = 0) and of the bands (for $k = 5\times10^{-6}$, 1.66×10^{-5}, and 5.78×10^{-5} s^{-1}) as a function of time. (We assumed that the wave front is located where $C = 0.5C_0$ and the band is located where C is maximum.) The traveling waves will eventually reach a steady state due to the balance between growth,

decay, and random motility. The speeds of the traveling waves, v_{gb}, are 0.16, 0.15, and 0.12 mm/h for $k = 0$, $5{\times}10^{-6}$, and $1.66{\times}10^{-5}$ s^{-1}, respectively. Figure 3.10b shows v_{gb} as a function of k. The results illustrate that v_{gb} decreases with an increase in k, but this decrease is minor when k is small.

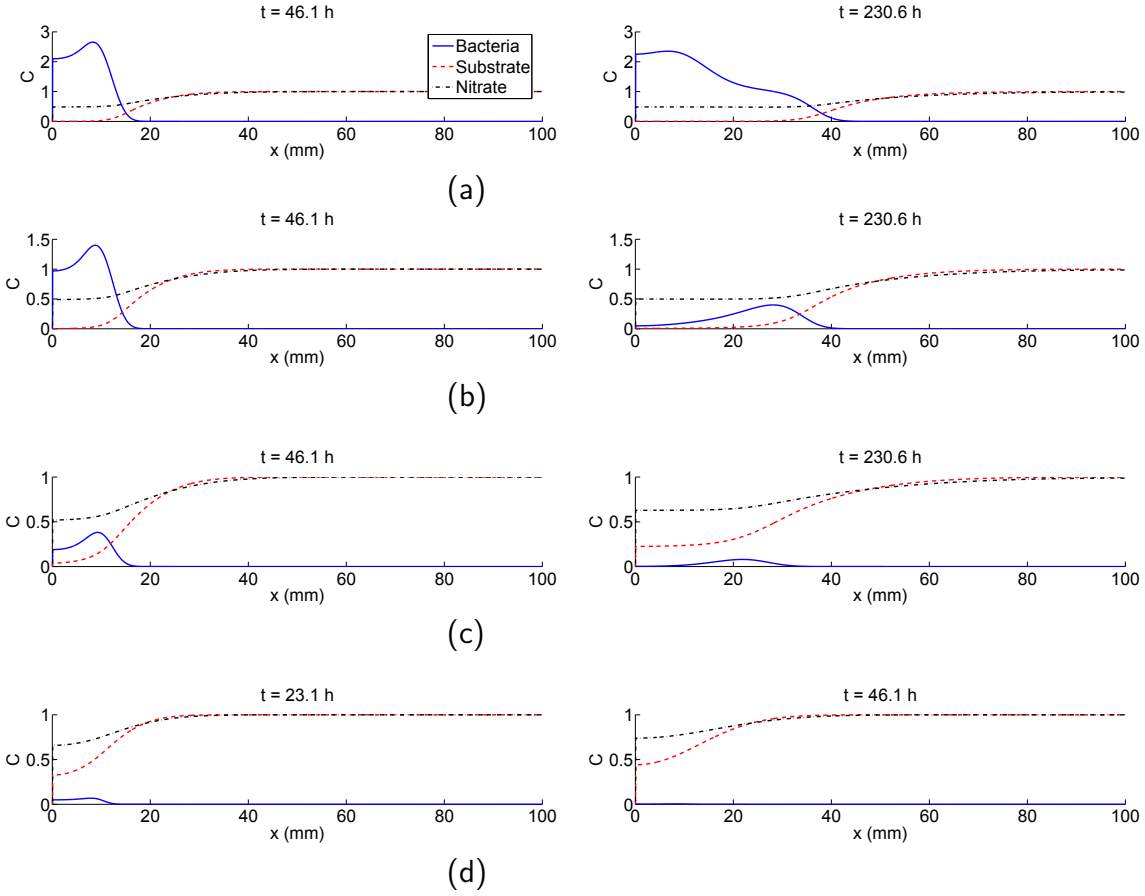

Figure 3.9: Normalized concentration profiles at two time moments for four decay rates for the *Azoarcus tolulyticus*/toluene system. (a) $k = 0$; (b) $k = 5{\times}10^{-6}$ s^{-1}; (c) $k = 1.66{\times}10^{-5}$ s^{-1}; and (d) $k = 5.78{\times}10^{-5}$ s^{-1}.

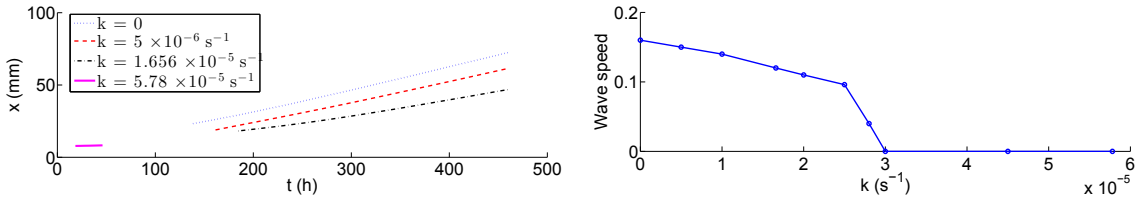

(a) (b)

Figure 3.10: (a) Location of bacterial waves, including front and band, as a function of time for four bacterial decay rates k. (b) Wave speed as a function of k.

3.4.4.0.2 The impact of yield coefficient Y

Here we examine the impact of yield coefficient Y. We selected $k = 5{\times}10^{-6}$ s^{-1}. The Y in Table 3.1 indicates that about 95% of the substrate is utilized by bacterial growth, and this value is almost the largest yield coefficient in a real biological system. Therefore, we considered smaller values, $Y = 3$ and 1 mg cell/mg substrate. No band was observed for $Y = 1$ mg cell/mg substrate, because the growth rate was relatively small compared to the decay rate (results not shown). A small band was observed for $Y = 3$ mg cell/mg substrate. We added an unrealistically high yield coefficient, $Y = 15$ mg cell/mg substrate, to examine the effect of Y on bacterial bands. Figure 3.11, together with Figure 3.9c, show the simulated concentration profiles for $Y = 3$, 5.3 and 15 mg cell/mg substrate, respectively. The plots show that the speed and peak of the traveling bands increase with Y, because a larger Y decreases the time for bacteria to reach their maximum concentration (starting out from zero) and because v_{gb} is inversely proportional to this time. The band speeds are 0.08, 0.15, and 0.28 mm/h for $Y = 3$, 5.3, and 15 mg cell/mg substrate, respectively. Therefore v_{gb} is approximately proportional to the square root of Y when the growth rate is relatively large compared to the decay rate such

that bacterial decay does not affect bacterial propagation. Otherwise, v_{gb} exponentially increases with Y with an exponent less than one half.

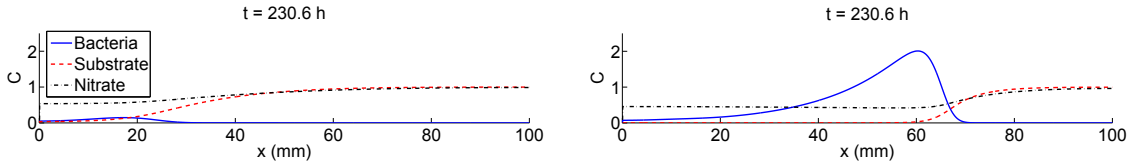

(a) (b)

Figure 3.11: Normalized concentration profiles for different yield coefficients Y for the *Azoarcus tolulyticus*/toluene system. (a) $Y = 3$ mg cell/mg substrate, and (b) $Y = 15$ mg cell/mg substrate.

3.4.4.0.3 The impact of the maximum reaction rate of substrate q_s

Here we examine the effects of the maximum reaction rate of substrate q_s. We selected $k = 5.0{\times}10^{-6}$ s^{-1} and $Y = 5.3$ mg substrate/mg cell-s. Because q_e is proportional to q_s, its value changes with q_s. Figure 3.12, together with Figure 3.9c, show the simulated concentration profiles for three q_s values. The plots show that v_{gb} increases with q_s. The band speeds are 0.15, 1.1, and 1.5 mm/h for $q_s = 2.15{\times}10^{-5}$, $8{\times}10^{-4}$, and $1.5{\times}10^{-3}$ mg substrate/mg cell-s, respectively. Therefore, v_{gb} is also approximately proportional to the square root of q_s.

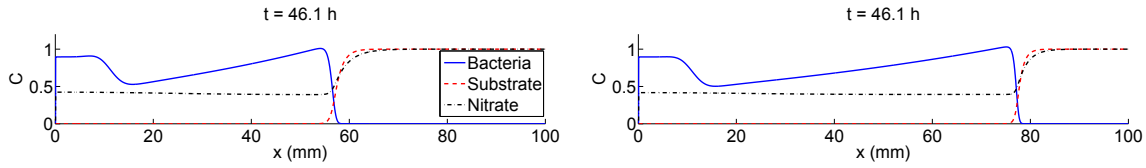

(a) (b)

Figure 3.12: Normalized concentration profiles for different maximum reaction rates of substrate q_s for the *Azoarcus tolulyticus*/toluene system. (a) $q_s = 8{\times}10^{-4}$ mg substrate/mg cell-s, and (b) $q_s = 1.5{\times}10^{-3}$ mg substrate/mg cell-s.

3.4.4.0.4 The impact of bacterial random motility coefficient D_{mb}

The random motility coefficient of bacteria D_{mb} has been thought to affect v_{gb} [28]. Here we try to build a quantitative relation between D_{mb} and v_{gb}. We selected $k = 5\times10^{-6}$ s^{-1}, $Y = 5.3$ mg cell/mg substrate, and $q_s = 2.15\times10^{-5}$ mg substrate/mg cells. Figure 3.13, together with Figure 3.9c, show the simulated concentration profiles for three D_{mb} values. The plots show that v_{gb} increases with D_{mb}. Note that we present the results at time $t = 92.2$ hrs for $D_{mb} = 3.2\times10^{-6}$ cm^2/s because the band is not yet observed when $t = 46.1$ hrs. The band speeds are 0.15, 0.5, and 1.5 mm/h for $D_{mb} = 3.2\times10^{-7}$, 3.2×10^{-6}, and 3.2×10^{-5} cm^2/s, respectively. Therefore, v_{gb} is approximately proportional to the square root of D_{mb}, which is consistent with results by Lauffenburger et al. [28].

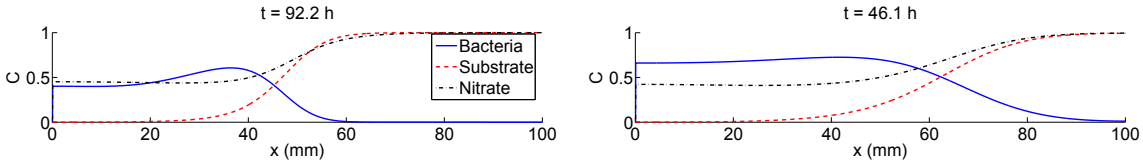

(a) (b)

Figure 3.13: Normalized concentration profiles for different random motility coefficients of bacteria D_{mb} for the *Azoarcus tolulyticus*/toluene system. (a) $D_{mb} = 3.2\times10^{-6}$ cm^2/s, and (b) $D_{mb} = 3.2\times10^{-5}$ cm^2/s.

3.4.4.0.5 Correlation equation for v_{gb}

The above simulations illustrate that v_{gb} increases with the square roots of Y, q_s, and D_{mb}. Several studies have addressed the traveling waves for reaction-diffusion equations [6, 11]. They usually introduced complicated mathematical methods to analyze the partial

differential equations and discuss the existence of solutions under certain conditions. For the sake of simplicity, we present a conceptual model that explains how the bacteria form a traveling wave if chemotaxis and convection is absent and also explains the observed dependencies. The idea is that the combination of bacterial motion (due to their random motility) and growth allows bacteria to form a traveling wave, which would not be possible without growth. Figure 3.14 illustrates the joint effects of random motility and growth. If bacterial growth was not present, a bacterial front present at time t would, in a time step Δt, spread out by a distance

$$\Delta x \sim \sqrt{D_{mb}\Delta t} \tag{3.7}$$

with no net movement to the right. However, when growth occurs, the bacterial concentration at the front increases because both substrate and electron acceptor are available. If the front advances in a steady motion, growth allows the bacterial profile at time $t+\Delta t$ to be the same as at time t, except that it is shifted to the right. The time step during which the concentration at the front manages to increase to the steady concentration is on the order of

$$\Delta t \sim \frac{1}{Yq_s} \tag{3.8}$$

Here we exclude initial bacteria and substrate concentrations, because they are constant and do not change the relation in Eq. (3.8). If growth occurs, the Δx in Eq. (3.7) can be interpreted as the distance by which the front advances during the time step Δt.

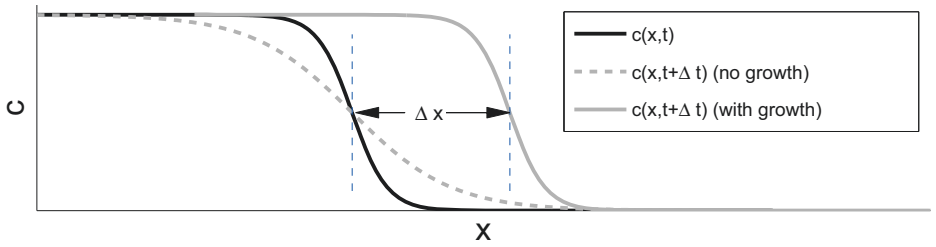

Figure 3.14: Conceptual model that explains how bacterial growth can cause a traveling bacterial wave. The bacterial motility causes a bacterial front to spread out (dashed line). Superimposed growth increases the bacterial concentration such that a front is formed at time $t + \Delta t$ that has the same shape as the front at time t.

Therefore, we can calculate the band speed via $v_{gb} = \Delta x/\Delta t$. Combining Eqs. (3.7) and (3.8) yields

$$v_{gb} \sim \sqrt{D_{mb} Y q_s} \tag{3.9}$$

Our conceptual model illustrates the relation between growth/decay/motility wave speed and bacterial growth and random motility. If bacterial decay exists, the mechanism for bacteria to migrate forward is the same as in the case without decay, except that the traveling front changes to a traveling band. When the decay rate is relatively small compared to the growth rate, Eq. (3.9) is still approximately valid. However, with the increase in k, v_{gb} exponentially increases with Y with an exponent less than one half and eventually becomes zero, as Figure 3.10b shows. To test the expression Eq. (3.9), we performed simulations with different D_{mb}, Y, q_s values in all three bacteria/substrate systems, in which chemotaxis was neglected. Figure 3.15 shows v_{gb} as a function of γ ($\gamma = \sqrt{D_{mb} Y q_s}$). For each system, the v_{gb} versus γ data is well represented by a linear model. Therefore, γ can be used to estimate v_{gb}.

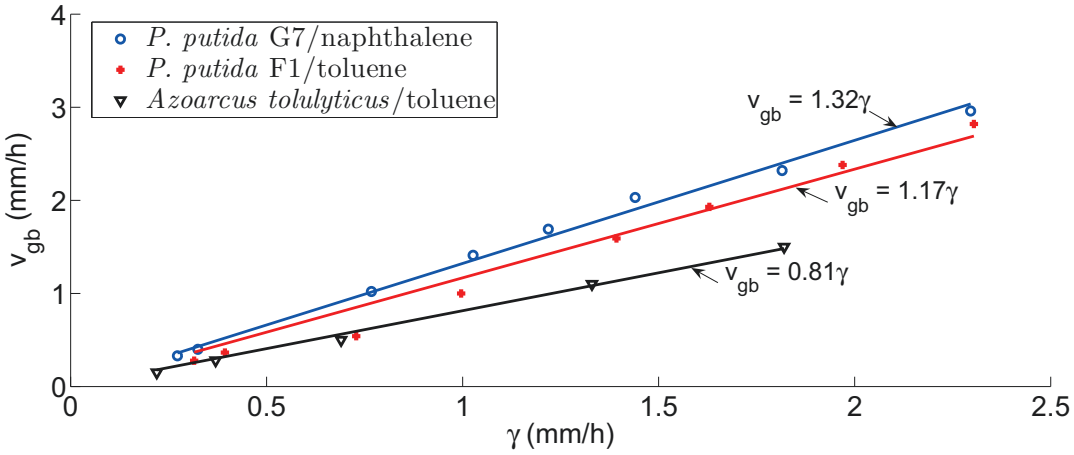

Figure 3.15: The simulated band speed v_{gb} varies with γ ($\gamma = \sqrt{D_{mb} Y q_s}$) for the three bacteria/substrate systems.

3.5 Concluding remarks

Traveling bacterial waves are capable of enhancing contaminant bioremediation in the subsurface. The removal efficiency increases with the speed of traveling waves. This paper studies the coupled effects of chemotaxis and growth on the formation and propagation of bacterial waves. The following conclusions can be drawn:

(1) Three types of traveling waves can be formed by chemotactic bacteria in the presence of growth and decay: (i) a chemotactic wave due to the biased movement of chemotactic bacteria toward high substrate concentration; (ii) a growth/decay/motility wave due to the balance between bacterial growth, decay and random motility; and (iii) an integrated wave due to the interaction between growth and chemotaxis.

(2) Both the growth/decay/motility wave and the integrated wave eventually exhibit a constant speed, while the chemotactic wave experiences a decreasing speed. The speeds

of the growth/decay/motility wave and the integrated wave are independent of the total number of bacteria inside the wave, while the speed of the chemotactic wave is proportional to this number.

(3) Bacterial growth is particularly important for bacterial propagation and contaminant remediation. If growth is absent, bacterial transport will eventually be dominated by random motility, even though chemotaxis initially produces a band. This diffusion limitation will significantly decrease the effectiveness of a bioremediation action.

(4) The initial electron acceptor concentration e_0 affects the growth/decay/motility wave speed v_{gb}, depending on the comparison of e_0 with the half-saturation coefficient of electron acceptor, k_e. If e_0 is much larger than k_e, it does not change v_{gb}. Otherwise, v_{gb} increases with e_0.

(5) Injecting sufficient electron acceptor so that the bacteria can degrade all substrate is crucial for improving the efficiency of contaminant removal by means of chemotaxis. However, too much electron acceptor is unnecessary due to limitations in substrate availability. An initial concentration that is slightly higher than the critical one for all substrate being consumed is a good choice.

(6) The effects of chemotaxis on bacterial propagation depend on the strength of chemotaxis. If chemotaxis alone is too weak to form a wave or if the speed of this chemotactic wave is less than half of the speed of the growth/decay/motility wave, chemotaxis hardly improves bacterial propagation. However, once the former speed exceeds the latter one, chemotaxis substantially improves the bacterial propagation.

(7) Convection speeds up the growth/decay/motility wave but slows down or even eliminates the chemotactic wave. When convection is weak, the traveling bacterial waves can move upstream against groundwater, which enable bioremediation to occur in upstream areas. As the convective velocity increases, the chemotactic waves finally disappear and chemotaxis hardly improves bacterial propagation. However, a stronger convection can improve bioavailability and bioremediation of contaminants by increasing the effective dispersion of both bacteria and contaminants.

(8) The speed of the growth/decay/motility wave, v_{gb}, is proportional to the square roots of the yield coefficient Y, the maximum reaction rate of substrate q_s, and the random motility coefficient of bacteria D_{mb}. We can use the variable $\gamma = \sqrt{D_{mb} Y q_s}$ to estimate v_{gb}. v_{gb} decreases with an increase in bacterial decay rate k, but this decrease is minor when the decay rate is relatively small compared to the growth rate.

(9) Although, to our best knowledge, no literature has reported the formation of integrated waves during an *in situ* bioremediation, Wang et al. [51] has demonstrated that the combination of chemotaxis and growth greatly accelerated the migration of bacteria toward regions with higher contaminant concentration in both laboratory and field aquifer. Our work provides prediction whether the interactions between chemotaxis and growth allow optimizing the biodegradation of contaminants in the subsurface. If we seek to enhance contaminant biodegradation by bacterial chemotaxis and growth, we need to ensure that initial bacteria and electron donor concentrations are sufficiently high, the field environment should be suitable for bacterial survival and production, and the

groundwater flow slowly so that the dispersion is weak.

In our study, we neglected many important mechanisms for bacterial transport in the natural subsurface. For example, bacteria can be deposited to surfaces of grains by electrostatic force or remain inside the secondary energy minimum, or be trapped in pore throats due to straining [13, 43]. Moreover, we assume bacteria as dilute suspension, which means bacteria do not interact each other. However, this assumption is invalid when the bacterial concentration is high. The interaction of dense bacterial populations can generate active flow and affect the transport of bacteria and contaminants [9]. All these mechanisms can significantly affect bacterial transport and contaminant bioremediation. We plan to include these principles in our future work.

3.6 Appendix: lattice Boltzmann model

We used lattice Boltzmann model to simulate the transport and fate of bacteria and substrates in this paper. The dimensionless version of Eqs. (4.23), (4.24) and (3.3) are:

$$\frac{\partial \hat{b}}{\partial \hat{t}} + \hat{\vec{\nabla}} \cdot \hat{b}(\hat{\vec{v}} + \frac{\hat{\vec{v_c}}}{\tau}) = \frac{1}{Pe_b}\hat{\nabla}^2\hat{b} + \hat{Y}\hat{q_s}\frac{\hat{s}}{\hat{s}+\hat{k_s}}\frac{\hat{e}}{\hat{e}+\hat{k_e}}\hat{b} - \hat{k}\hat{b} \tag{3.10}$$

$$\frac{\partial \hat{s}}{\partial \hat{t}} + \hat{\vec{\nabla}} \cdot \hat{s}\hat{\vec{v}} = \frac{1}{Pe_s}\hat{\nabla}^2\hat{s} - \hat{q_s}\frac{\hat{s}}{\hat{s}+\hat{k_s}}\frac{\hat{e}}{\hat{e}+\hat{k_e}}\hat{b} \tag{3.11}$$

$$\frac{\partial \hat{e}}{\partial \hat{t}} + \hat{\vec{\nabla}} \cdot \hat{e}\hat{\vec{v}} = \frac{1}{Pe_e}\hat{\nabla}^2\hat{e} - \hat{q_e}\frac{\hat{e}}{\hat{e}+\hat{k_e}}\frac{\hat{s}}{\hat{s}+\hat{k_s}}\hat{b} \tag{3.12}$$

where $\hat{b} = b/b_0$, $\hat{s} = s/s_0$, $\hat{e} = e/e_0$, $\hat{t} = tv_0/\Delta l$, $\hat{\vec{\nabla}} = \Delta l\vec{\nabla}$, $\hat{\vec{v}} = \vec{v}/v_0$, $\hat{\vec{v}}_c = \vec{v}_c/v_0$, $\hat{Y} = Ys_0/b_0$, $\hat{k} = k\Delta l/v_0$, $\hat{k_s} = k_s/s_0$, $\hat{k_e} = k_e/e_0$, $\hat{q_s} = q_s b_0 \Delta l/s_0/v_0$, $\hat{q_e} = q_e b_0 \Delta l/e_0/v_0$, $Pe_b = v_0\Delta l/D_b$, $Pe_s = v_0\Delta l/D_s$, $Pe_e = v_0\Delta l/D_e$, v_0 is the same as the bacterial swimming speed, and Δl is the grid spacing.

The corresponding controlling equations in the lattice Boltzmann model are:

$$\beta_n(\hat{\vec{x}} + \vec{e}_n, \hat{t}+1) = \beta_n(\hat{\vec{x}}, \hat{t}) + \frac{1}{\tau_b}\left[\beta_n^{(0)}(\hat{\vec{x}}, \hat{t}) - \beta_n(\hat{\vec{x}}, \hat{t})\right] + \hat{Y}\frac{\beta_n(\hat{\vec{x}}, \hat{t})}{\hat{b}(\hat{\vec{x}}, \hat{t})}\hat{r_s}(\hat{\vec{x}}, \hat{t}) - \hat{k}\beta_n(\hat{\vec{x}}, \hat{t}) \tag{3.13}$$

$$\sigma_n(\hat{\vec{x}} + \vec{e}_n, \hat{t}+1) = \sigma_n(\hat{\vec{x}}, \hat{t}) + \frac{1}{\tau_s}\left[\sigma_n^{(0)}(\hat{\vec{x}}, \hat{t}) - \sigma_n(\hat{\vec{x}}, \hat{t})\right] - \frac{\sigma_n(\hat{\vec{x}}, \hat{t})}{\hat{s}(\hat{\vec{x}}, \hat{t})}\hat{r_s}(\hat{\vec{x}}, \hat{t}) \tag{3.14}$$

$$\alpha_n(\hat{\vec{x}} + \vec{e}_n, \hat{t}+1) = \alpha_n(\hat{\vec{x}}, \hat{t}) + \frac{1}{\tau_e}\left[\alpha_n^{(0)}(\hat{\vec{x}}, \hat{t}) - \alpha_n(\hat{\vec{x}}, \hat{t})\right] - \frac{\alpha_n(\hat{\vec{x}}, \hat{t})}{\hat{e}(\hat{\vec{x}}, \hat{t})}\hat{r_e}(\hat{\vec{x}}, \hat{t}) \tag{3.15}$$

where

$$\begin{gathered}\hat{Y}\frac{\beta_n}{\hat{b}}\hat{r_s} - \hat{k}\beta_n = Y\frac{q_s\Delta l}{v_0}\frac{s_0\hat{s}}{s_0\hat{s}+k_s}\frac{e_0\hat{e}}{e_0\hat{e}+k_e}\beta_n - \hat{k}\frac{\Delta l}{v_0}\beta_n, \\ \frac{\sigma_n}{\hat{s}}\hat{r_s} = \frac{q_s\Delta l b_0\hat{b}}{v_0(s_0\hat{s}+k_s)}\frac{e_0\hat{e}}{e_0\hat{e}+k_e}\sigma_n, \qquad \frac{\alpha_n}{\hat{e}}\hat{r_e} = \frac{q_e\Delta l b_0\hat{b}}{v_0(e_0\hat{e}+k_e)}\frac{s_0\hat{s}}{s_0\hat{s}+k_s}\alpha_n\end{gathered} \tag{3.16}$$

The relaxation times, τ_b, τ_s, τ_e, are related to the diffusion coefficient of bacteria, substrate, and electron acceptor:

$$\frac{1}{Pe_b} = \frac{1}{2}(\tau_b - \frac{1}{2}), \quad \frac{1}{Pe_s} = \frac{1}{2}(\tau_s - \frac{1}{2}), \quad \frac{1}{Pe_e} = \frac{1}{2}(\tau_e - \frac{1}{2}) \tag{3.17}$$

The Eqs. (3.13), (3.14) and (3.15) can attain solutions to Eqs. (4.26), (4.27) and

(3.12) in the limit of small convective velocity (see Hilpert [19], Long and Hilpert [32]).

Bibliography

[1] J.P. Adler. Chemotaxis in bacteria. *Science*, 153:708–716, 1966.

[2] US Environment Protection Agency. Cleaning up the nation's waste sites: markets and technology trends. 2004.

[3] I.S. Ahn, W.C. Ghiorse, L.W. Lion, and M.L. Shuler. Growth kinetics of Pseudomonas putida G7 on naphthalene and occurrence of naphthalene toxicity during nutrient deprivation. *Biotechnology and Bioengineering*, 59(5):587–594, September 1998.

[4] M. Alexander. *Biodegradation and bioremediation*. Academic Press, 1999.

[5] G. Alexandre, S. Greer-Phillips, and I. Zhulin. Ecological role of energy taxis in microorganisms. *FEMS Microbiology Reviews*, 28(1):113–126, feb 2004.

[6] H. Berestycki and F. Hamel. Generalized travelling waves for reaction-diffusion equations. *Contemporary Mathematics Series*, 446:101–123, 2007.

[7] P Bombach, H H Richnow, and M Kästner. Current approaches for the assessment of in situ biodegradation. *Applied Microbiology and Biotechnology*, 86(3):839–852, February 2010.

[8] J. Delgado. Longitudinal and transverse dispersion in porous media. *Chemical Engineering Research and Design*, 85:1245–1252, September 2007.

[9] C. Dombrowski, L. Cisneros, S. Chatkaew, R.E. Goldstein, and J.O. Kessler. Self-concentration and large-scale coherence in bacterial dynamics. *Physical Review Letters*, 93(9):098103, August 2004.

[10] J. Elmen, W. Pan, and S. Leung. Kinetics of toluene degradation by a nitrate-reducing bacterium isolated from a groundwater aquifer. *Biotechnology and Bioengineering*, 55(1):82–90, jul 1997.

[11] Z. Feng. Traveling waves to a reaction–diffusion equation. *Discrete and Continuous Dynamical Systems Supplement*, pages 382–390, 2007.

[12] M. Funaki, M. Mimura, and T. Tsujikawa. Travelling front solutions arising in the chemotaxis-growth model. *Interfaces and Free Boundaries*, 8(2):223–245, 2006.

[13] T.R. Ginn, B.D. Wood, K.E. Nelson, T.D. Scheibe, E.M. Murphy, and T.P. Clement. Processes in microbial transport in the natural subsurface. *Advances in Water Resources*, 25:1017–1042, 2002.

[14] A.C. Grimm and C.S. Harwood. Chemotaxis of $Pseudomonas$ spp.to the polyaromatic hydrocarbon naphthalene. *Applied and Environmental Microbiology*, 63(10): 4111–4115, 1997.

[15] P. Han and D.M. Bartels. Temperature dependence of oxygen diffusion in H2O and D2O. *The Journal of Physical Chemistry*, 100(13):5597–5602, January 1996.

[16] T. Hashitani and K. Tanaka. Measurements of self-diffusion coefficients of the nitrate ion in aqueous solutions of potassium nitrate and calcium nitrate. *J.Chem.Soc., Faraday Trans.1*, 79(8):1765–1768, 1983.

[17] A.C. Hawkins and C.S. Harwood. Chemotaxis of Ralstonia eutropha JMP134 (pJP4) to the herbicide 2, 4-dichlorophenoxyacetate. *Applied and Environmental Microbiology*, 68(2):968–972, February 2002.

[18] T. Hillen and K.J. Painter. A user's guide to PDE models for chemotaxis. *Journal of Mathematical Biology*, 58:183–217, 2009.

[19] M. Hilpert. Lattice-Boltzmann model for bacterial chemotaxis. *Journal of Mathematical Biology*, 51:302–332, 2005.

[20] D. Horstmann. From 1970 until present: the Keller-Segel model in chemotaxis and its consequences I. *Jahresbericht DMV*, 105(3):103–165, 2003.

[21] R. Jittawattanarat and K. Kostarelos. Immobilized cell augmented activated sludge process for enhanced nitrogen removal from wastewater. *Water Environment Research*, 79(11):2325–2335, May 2007.

[22] K.S. Jorgensen. In situ bioremediation. *Advances in Applied Microbiology*, 61:285–305, February 2007.

[23] E.F. Keller and L.A. Segel. Model for chemotaxis. *Journal of Theoretical Biology*, 30:225–234, 1971.

[24] C. Kennedy and R. Aris. Traveling waves in a simple population model involving growth and death. *Bulletin of Mathematical Biology*, 42(3):397–429, 1980.

[25] T. Krell, J. Lacal, J.A. Reyes-Darias, C. Jimenez-Sanchez, R. Sungthong, and J.J. Ortega-Calvo. Bioavailability of pollutants and chemotaxis. *Current Opinion in Biotechnology*, 24(3):451–456, June 2013.

[26] S. Labana, G. Pandey, D. Paul, and N.K. Sharma. Pot and field studies on bioremediation of p-nitrophenol contaminated soil using Arthrobacter protophormiae RKJ100. *Environmental Science and Technology*, 39(9):3330–3337, May 2005.

[27] S. Labana, O.V. Singh, A. Basu, and G. Pandey. A microcosm study on bioremediation of p-nitrophenol-contaminated soil using Arthrobacter protophormiae RKJ100. *Applied Microbiology and and Biotechnology*, 68(3):417–424, August 2005.

[28] D. Lauffenburger, C.R. Kennedy, and R. Aris. Traveling bands of chemotactic bacteria in the context of population growth. *Bulletin of Mathematical Biology*, 46(1):19–40, 1984.

[29] A. Law. The effect of oxygen on chemotaxis to naphthalene by Pseudomonas putida G7. *Biotechnology and Bioengineering*, 93(3):457–464, February 2006.

[30] A. Law and M. Aitken. Bacterial chemotaxis to naphthalene desorbing from a non-aqueous liquid. *Applied and Environmental Microbiology*, 69(10):5968–5973, October 2003.

[31] W. Long and M. Hilpert. Analytical solutions for bacterial energy taxis (chemotaxis): traveling bacterial bands. *Advances in Water Resources*, 30:2262–2270, 2007.

[32] W. Long and M. Hilpert. Lattice-Boltzmann modeling of contaminant degradation by chemotactic bacteria: Exploring the formation and movement of bacterial bands. *Water Resources Research*, 44:W09415, 2008.

[33] M. Mansour. On traveling wave fronts in a bacterial growth model with density-dependent diffusion and chemotaxis. *Journal of Statistical Physics*, 143(1):197–204, 2011.

[34] R.B. Marx and M.D. Aitken. Bacterial chemotaxis enhances naphthalene degradation in a heterogeneous aqueous system. *Environmental Science and Technology*, 34: 3379–3383, 2000.

[35] R.B. Marx and M.D. Aitken. Quantification of chemotaxis to naphthalene by *Pseudomonas putida* G7. *Applied and Environmental Microbiology*, 65:2847–2852, 1999.

[36] M.S. Olson, R.M. Ford, J.A. Smith, and E.J. Fernandez. Quantification of bacterial chemotaxis in porous media using magnetic resonance imaging. *Environmental Science and Technology*, 38(14):3864–3870, July 2004.

[37] G. Pandey and R.K. Jain. Bacterial chemotaxis toward environmental pollutants: role in bioremediation. *Applied and Environmental Microbiology*, 68(12):5789–5795, December 2002.

[38] J. Pandey, A. Chauhan, and R.K. Jain. Integrative approaches for assessing the ecological sustainability of in situ bioremediation. *FEMS Microbiology Reviews*, 33 (2):324–375, March 2009.

[39] R.E. Parales, J.L. Ditty, and C.S. Harwood. Toluene-degrading bacteria are chemotactic towards the environmental pollutants benzene, toluene, and trichloroethylene. *Applied and Environmental Microbiology*, 66(9):4098–4104, September 2000.

[40] D.L. Pardieck, E.J. Bouwer, and A.T. Stone. Hydrogen peroxide use to increase oxidant capacity for in situ bioremediation of contaminated soils and aquifers: A review. *Journal of Contaminant Hydrology*, 9(3):221–242, March 1992.

[41] J.A. Pedit, R.B. Marx, C.T. Miller, and M.D. Aitken. Quantitative analysis of experiments on bacterial chemotaxis to naphthalene. *Biotechnology and Bioengineering*, 78(6):626–634, June 2002.

[42] K. Reardon and D. Mosteller. Biodegradation kinetics of benzene, toluene, and phenol as single and mixed substrates for Pseudomonas putida F 1. *Biotechnology and Bioengineering*, 69(4):385–400, August 2000.

[43] J.A. Redman, S.L. Walker, and M. Elimelech. Bacterial adhesion and transport in

porous media: Role of the secondary energy minimum. *Environmental Science and Technology*, 38:1777–1785, 2004.

[44] B.E. Rittmann and P.L. McCarty. *Environmental biotechnology*. principles and applications. McGraw-Hill Science/Engineering/Math, 2001.

[45] M.A. Rivero, R.T. Tranquillo, H.M. Buettner, and D. Lauffenburger. Transport models for chemotactic cell populations based on individual cell behaviour. *Chemical Engineering Science*, 44(12):2881–2897, 1989.

[46] S.K. Samanta, B. Bhushan, and A. Chauhan. Chemotaxis of a Ralstonia sp.SJ98 toward different nitroaromatic compounds and their degradation. *Biochemical and Biophysical Research Communications*, 269(1):117–123, May 2000.

[47] R.P. Schwarzenbach, P.M. Gschwend, and D.M. Imboden. *Environmental organic chemistry*. Schwarzenbach/Environmental. John Wiley and Sons, Inc., Hoboken, NJ, USA, June 2005.

[48] R. Singh and M.S. Olson. Kinetics of trichloroethylene and toluene toxicity to Pseudomonas putida F1. *Environmental Toxicology and Chemistry / SETAC*, 29(1): 56–63, January 2010.

[49] B.L. Taylor, I.B. Zhulin, and M.S. Johnson. Aerotaxis and other energy-sensing behavior in bacteria. *Annual Review of Microbiology*, 53:103–128, 1999.

[50] I. Vasiliadou. Cotransport of Pseudomonas putida and kaolinite particles through

water-saturated columns packed with glass beads. *Water Resources Research*, 47 (2), February 2011.

[51] M. Wang, R.M. Ford, and R.W. Harvey. Coupled effect of chemotaxis and growth on microbial distributions in organic-amended aquifer sediments: observations from laboratory and field studies. *Environmental Science and Technology*, 42(10):3556–3562, May 2008.

[52] X. Wang and T. Long. Bacterial chemotaxis toward a NAPL source within a pore-scale microfluidic chamber. *Biotechnology and Bioengineering*, 109(7):1622–1628, July 2012.

Chapter 4. A Pedestrian's Guide to a Numerical-Diffusion-Free Two-Relaxation-Time Lattice Boltzmann Model for Reactive-Diffusive Transport

4.1 Abstract

In the last decade, theoretical physicists have developed Lattice Boltzmann (LB) models based on two-relaxation-time (TRT) collision operators. These methods are very powerful, because they are computationally efficient and because numerical diffusion can be eliminated. Inspired by Edward G. Harris's "Pedestrian Approach to Quantum Field Theory," we synthesized results from several papers to allow for an easy implementation of this method without background in theoretical physics. We present a pseudo-code for a three-dimensional TRT-LB method for advective-diffusive-reactive transport for the popular D3Q15 lattice structure. Solute transport with initial Gaussian and top hat distributions were investigated to evaluate the accuracy and stability of the TRT models

This paper will be submitted to *Water Resources Research*.

with and without the velocity correction, which eliminates numerical diffusion. When advection is present, the TRT model without the velocity correction generated negative numerical diffusion, while the TRT model with the velocity correction could eliminate this numerical diffusion. The TRT model with the correction also exhibited a better numerical stability than the TRT model without the correction when advection exists, although the numerical diffusion can be neglected when the advective velocity is small. Therefore, it is advisable to include the velocity correction in the TRT model when the advective velocity is large. Finally, we applied the TRT models to examine Taylor dispersion and bacterial chemotaxis. The TRT model with the correction showed good accuracy and stability even if the advective velocity is large.

4.2 Introduction

Reactive transport modeling is an essential tool to estimate the risk of groundwater contamination. Both large-scale and pore-scale models have been developed to study transport and fate of contaminants in the subsurface [6, 21]. In large-scale simulations, contaminant concentrations are averaged over a representative elementary volume. The characteristics of pore geometry are represented by macroscopic parameters such as porosity and permeability. The simulations predict contaminant fate and transport at the field scale, but it is not always clear whether pore-scale processes are accounted for appropriately. By contrast, pore-scale simulations examine concentration distribution in pore areas, where biogeochemical reactions and interactions between the aqueous solution and solid surfaces are directly calculated [25]. Therefore, studies of pore-scale reactive transport can deepen our understanding of large-scale natural processes [3]. With the rapidly growing availability of high performance computational resources, pore-scale simulations have become a powerful tool for investigating a broad range of porous medium transport phenomena [27, 31].

The Lattice Boltzmann (LB) method is a widely used method for simulating a broad range of flow and transport phenomena. This method has become particularly popular when analyzing porous medium processes at the pore scale, because voxel images of porous media can be used directly as an input to the simulations [28, 22, 34, 26, 4]. In the LB method, fluids, solutes, or microorganisms are represented by particles that move on a typically regular lattice with a discrete set of velocities, which correspond to

lattice vectors $\mathbf{c}_q$. Evolution in time is achieved by repeatedly performing a travel and a collision step. During the travel step, particles move from one lattice node to another. Then particles that are present at a node and that have different velocities collide with each other. During this collision step, the particle velocity distribution approaches an equilibrium distribution, and the rate of approach is controlled by one or more relaxation times. The definition of this equilibrium distribution and how it is approached critically determines the accuracy, stability, and computational efficiency of a LB method. Optimal formulation of the collision step is still an area of active research.

One LB model that is particularly promising in terms of accuracy and stability is the two-relaxation-time (TRT) LB method [10, 11, 15]. In this model, the particle distribution function, which quantifies the number of particles that have a velocity $\mathbf{c}_q$, is decomposed into symmetric and antisymmetric components. In case of advective-diffusive transport, the relaxation parameter acting on the antisymmetric components is related to the diffusion coefficient of the investigated chemical, while the relaxation parameter acting on symmetric components is free to choose. If the two relaxation parameters are chosen to be equal, the TRT model degrades to a single-relaxation-time (SRT) model, which is easy to implement but suffers from numerical instability. Moreover, the viscosity in SRT models for fluid flow is affected by pore boundaries [17]. This causes the permeability to become viscosity dependent, while it should be a characteristic of a porous medium alone [29]. Similarly, one can expect the diffusion coefficient in SRT models for advective-diffusive transport to be affected by pore boundaries. Even though this effect

might occur in real systems at distances from the boundary much smaller than a typical voxel size in a LB simulation, it is undesirable since our TRT model does not account for the physics that is relevant in this region. Although multiple-relaxation-time (MRT) LB models can improve the stability and reduce the aforementioned viscosity dependence [29], they are more complicated to implement than the TRT method, and the selection of optimal relaxation parameters that are crucial for numerical accuracy and stability is a challenge [8, 12]. In contrast, the TRT model can reduce the viscosity and diffusivity dependence on the boundary locations and is easy to implement [14, 15]. Ginzburg et al. [16] studied the optimal stability of TRT models for the advection-diffusion equation (ADE) and presented analytical stability conditions for a wide range of TRT models that differ in lattice structure and the exact formulation of the TRT method. Ginzburg [13] also developed a symmetrized framework for analyzing LB schemes for anisotropic advective-diffusive transport. This framework allowed deriving the general diffusion and numerical diffusion terms, which in turn allowed introducing "velocity correction terms" to eliminate the velocity-dependent numerical diffusion.

This paper studied the application of the TRT-LB method to the modeling of isotropic advective-diffusive and potentially reactive transport, where the numerical diffusion-eliminating correction term is accounted for or not. Our objectives are:

1. To present the TRT method for the widely used D3Q15 lattice structure in a comprehensive manner, that is, in a single paper. To do so, we synthesize original theoretical developments from Ginzburg's papers [10, 11, 15], and we present a

pseudo-code that allows for a straightforward implementation of the TRT method;

2. To evaluate the accuracy and stability of the TRT models with and without velocity correction term which eliminates numerical diffusion; and

3. To apply the TRT models to transport scenarios that are relevant to geophysical applications: (a) three-dimensional (3D) Taylor dispersion, and (b) one-dimensional (1D) chemotactic transport.

4.3 Two-relaxation-time lattice Boltzmann method

In the LB method, the state of a chemical is defined by a N-dimensional particle distribution $\mathbf{f}(\mathbf{r},t) = \{f_q(\mathbf{r},t),\ q = 0,\ldots,N-1\}$ which are set at each lattice node $\mathbf{r}$ and for each discrete time t. The particles move along with discrete velocities $\mathbf{c}_q \neq 0$ (where $q = 1,\ldots,N-1$) or stay at the node, $\mathbf{c}_0 = 0$. Summing the particle distribution over all possible particle velocities yields the dimensionless concentration C of the chemical:

$$C = \sum_{q=0}^{N-1} f_q \tag{4.1}$$

At each node, the particle distribution can be decomposed into symmetric and antisymmetric components:

$$f_q = f_q^+ + f_q^- \tag{4.2}$$

where $f_q^+ = (f_q + f_{\overline{q}})/2$, $f_q^- = (f_q - f_{\overline{q}})/2$ and $\mathbf{c}_q = -\mathbf{c}_{\overline{q}}$. The last equation states that $\overline{q}$ is the index of the lattice vector $\mathbf{c}_{\overline{q}}$ that points in the opposite direction of $\mathbf{c}_q$. For the rest particles, $f_0^+ = f_0 = C - \sum_{q=1}^{N-1} f_q$ and $f_0^- = 0$.

The particle distribution after a collision and travel step is given by

$$f_q(\mathbf{r} + \mathbf{c}_q, t+1) = \underbrace{f_q(\mathbf{r},t) - s^+(f_q^+ - e_q^+) - s^-(f_q^- - e_q^-)}_{\tilde{f}_q(\mathbf{r},t)} \tag{4.3}$$

where s^+ and s^- are eigenvalues of the linear collision operators, and e_q^+ and e_q^- are the symmetric and antisymmetric components, respectively, of the equilibrium particle distribution $e_q = e_q^+ + e_q^-$. The entire right hand side of Eq. (4.3) is called the post-collision particle distribution $\tilde{f}_q(\mathbf{r},t)$. Linear stability restricts the eigenvalues to the interval $(0,2)$. The TRT model degrades to a SRT model if $s^+ = s^- = 1/\tau$, where τ is the sole relaxation time.

The present study deals with advective-diffusive transport where diffusion is assumed to be isotropic, i.e., described by a scalar diffusion coefficient. The equilibrium particle distribution of the particles with a non-zero velocity ($\mathbf{c}_q \neq 0$) is then given by the following expressions [13]:

$$\begin{aligned} e_q^+ &= C(t_q^{(m)} c_e + g^{(u)} E_q^{(u)}) \\ E_q^{(u)} &= t_q^{(u)} \overline{V}^2 + w_q^{(u)} \|\mathbf{c}_q\|^2 \sum_{\alpha=1}^{d} (V_\alpha^2 - \overline{V}^2) c_{q\alpha}^2 + \sum_{\alpha \neq \beta} \frac{V_\alpha V_\beta c_{q\alpha} c_{q\beta}}{\sum_{j=1}^{N-1} c_{j\alpha}^2 c_{j\beta}^2} \end{aligned} \tag{4.4}$$

and

$$e_q^- = t_q^{(a)}(\mathbf{V}\cdot\mathbf{c}_q) \tag{4.5}$$

where $q = 1,\ldots,(N-1)/2$, $\mathbf{V}$ is the dimensionless advective velocity, $\overline{V}^2 = \sum_{\alpha=1}^{d} V_\alpha^2/d$, d is the dimensionality, and $g^{(u)}$ is a flag to exclude or include the velocity correction term $E_q^{(u)}$. If $g^{(u)} = 1$, the velocity correction is applied, if $g^{(u)} = 0$ it is not. The other half of the above equilibrium particle distribution (for $q = (N-1)/2+1,\ldots,N-1$) can be calculated by the symmetric and antisymmetric relations

$$e_{\overline{q}}^+ = e_q^+ \quad \text{and} \quad e_{\overline{q}}^- = -e_q^- \tag{4.6}$$

For the rest particles, $e_0^+ = C - 2\sum_{q=1}^{(N-1)/2} e_q^+$ and $e_0^- = 0$. To ensure numerical stability, c_e in Eq. (4.4) is required to be within the interval $[0\ 1]$. The actual interval depends on the selected lattice model and can be even smaller [16]. All weights $t_q^{(\cdot)}$ and $w_q^{(\cdot)}$ are non-negative, isotropic, and satisfy the following isotropy conditions:

$$\sum_q w_q^{(\cdot)} c_{q\alpha} c_{q\beta} = \delta_{\alpha\beta}, \quad \sum_q t_q^{(\cdot)} c_{q\alpha} c_{q\beta} = \delta_{\alpha\beta} \tag{4.7}$$

where $\alpha,\beta = 1,\ldots,d$. Different selections of the weights result in different stability bounds [16].

To make the TRT model as simple as possible, we apply the widely used standard bounce-back (SBB) boundary condition, which mimics the phenomenon that a particle is

reflected back into the pore domain when colliding with a solid surface [20, 17]. The SBB has the form

$$f_{\overline{q}}(\mathbf{r}, t+1) = \tilde{f}_q(\mathbf{r}, t) \tag{4.8}$$

If there exists a nondimensional mass source M, the post-collision particle distribution is updated as the follows:

$$\tilde{f}_q(\mathbf{r}, t) = \tilde{f}_q(\mathbf{r}, t) + t_q^{(m)} c_e M \tag{4.9}$$

With the Chapman-Enskog expansion, it can be shown that the solutions of the TRT equation (4.3) are also solutions to the following dimensionless isotropic reactive ADE [15]:

$$\frac{\partial C}{\partial T} + \nabla \cdot (\mathbf{V} C) = \hat{D} \nabla^2 C + M \tag{4.10}$$

where $\hat{D} = \wedge^- c_e$ is the nondimensional diffusion coefficient, and $\wedge^- = 1/s^- - 1/2$. Although the relaxation function of the antisymmetric component, $\wedge^-$, is dependent on the diffusion coefficient of the investigated chemical, the relaxation function of the symmetric component, $\wedge^+ = 1/s^+ - 1/2$ $(\wedge^+ > 0)$, is free to choose. The product of this two relaxation functions, $\wedge = \wedge^+ \wedge^-$, critically determines numerical accuracy and stability [16].

The TRT model can also be related to the dimensional reactive ADE:

$$\frac{\partial c}{\partial t} + \nabla \cdot (\mathbf{u} c) = D \nabla^2 c + I \tag{4.11}$$

where c is the concentration, $\mathbf{u}$ is the advective flow velocity, D is the diffusion coefficient, and I is the reaction term. With an appropriate characteristic length Δl and velocity u_0, the ADE can be normalized as follows:

$$\frac{\partial C}{\partial T} + \nabla \cdot (\mathbf{V}C) = \frac{1}{Pe_L}\nabla^2 C + \frac{\Delta l}{c_0 u_0} I, \tag{4.12}$$

where $C = c/c_0$, $T = tu_0/\Delta l$, $\mathbf{V} = \mathbf{u}/u_0$, and the lattice Peclet number

$$Pe_L = \frac{\Delta l u_0}{D} \tag{4.13}$$

Note that this $\mathbf{V}$ is the same as in Eqs. (4.4) and (4.5), because we set the characteristic velocity in lattice units equal to one. A comparison between Eqs. (4.10) and (4.12) illustrates that the TRT model gives solution to the reactive ADE if we set $\wedge^-$ and M such that $c_e \wedge^- = 1/Pe_L$ and $M = I\Delta l/(c_0 u_0)$.

The implementation of the TRT models that simulate reactive transport involves the following steps:

1. Governing equations for the reactive transport phenomenon are specified. The flow velocity field $\mathbf{u}$ and diffusion coefficient D are known inputs.

2. Characteristic parameters c_0, u_0, and Δl are selected to nondimensionalize the reactive ADE.

3. A specific lattice with discrete velocities $\mathbf{c_q}$ $(q = 1, \ldots, N-1)$ is chosen. The

associated parameters c_e, $t_q^{(u)}$, $t_q^{(m)}$, and $w_q^{(u)}$ are prescribed.

4. The relation $c_e \wedge^- = 1/Pe_L$ is used to calculate $\wedge^-$. Once we select $\wedge$, $\wedge^+$ can be determined according to $\wedge = \wedge^+ \wedge^-$.

5. The flag $g^{(u)}$ is assigned a value of either 0 or 1 to exclude or include the velocity correction.

6. The particle distribution $\mathbf{f}$ is initialized.

7. Finally, the TRT model is ready for simulating reactive transport.

During each time step of a simulation, the particle distribution is updated following sequential collision and travel steps. The nondimensional concentration C is calculated by the latest particle distribution through Eq. (4.1), and the dimensional concentration field as a function of time is given by $c = c_0 C$. A pseudo-code for simulating the advective-diffusive-reactive transport is presented in Figure 4.1.

4.4 Model analysis

We evaluated the numerical accuracy and stability of TRT models with and without the velocity correction by testing advective and diffusive transport with an initial Gaussian and top hat concentration distributions [7]. We applied the models to Taylor dispersion [33] and chemotactic transport [1]. A 3D TRT model with fifteen discrete velocities (D3Q15) was used in our simulations. According to Ginzburg et al. [16], we chose $c_e = 1/3$,

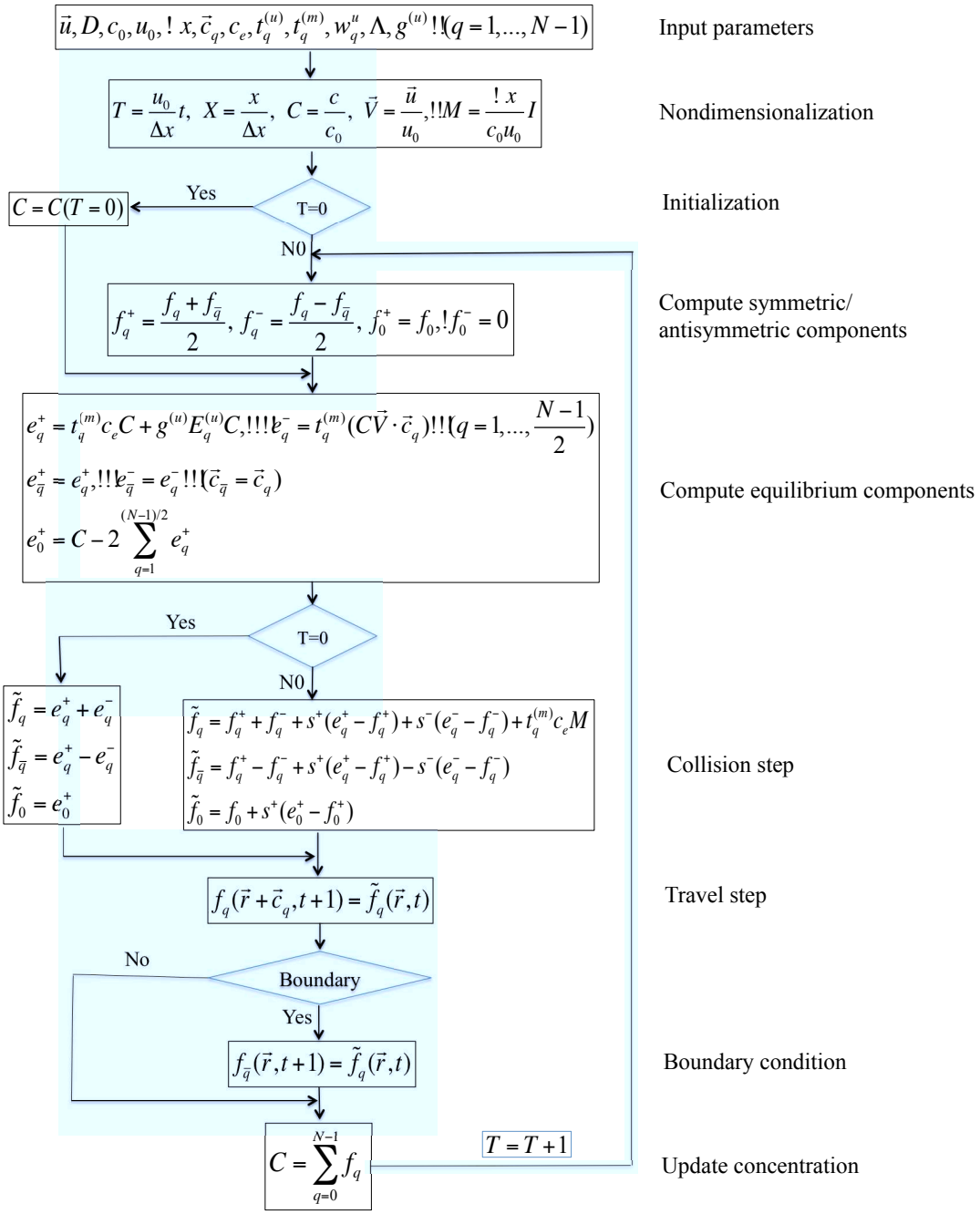

Figure 4.1: Pseudocode for applying TRT models to reactive transport.

$t_I^{(a)} = t_I^{(m)} = 1/4$, $t_{III}^{(a)} = t_{III}^{(m)} = 1/16$, $w_I^{(u)} = 1/2$, and $w_{III}^{(u)} = 0$ for $|\mathbf{c}_I|^2 = 1$ and $|\mathbf{c}_{III}|^2 = 3$. Ginzburg et al. [16] also introduced an optimal TRT subclass which was

defined by $\wedge = 1/4$. This choice enables the TRT model to simulate solutions to the ADE for any Peclet number. However, a smaller $\wedge$ value reduces higher-order truncation errors; therefore we selected $\wedge = 3/16$. The SRT model developed in [19] was compared to evaluate the accuracy and stability of the TRT models with and without the velocity correction.

4.4.1 1D transport with initial Gaussian concentration distribution

We first simulated 1D advective diffusive transport for an initial Gaussian concentration distribution:

$$C(x, t = 0) = \frac{1}{\sqrt{10\pi}} e^{-\frac{(x-10)^2}{10}} \tag{4.14}$$

Simulation results from the TRT models with and without the correction were compared against the analytical solution [7] given by

$$C(x, t) = \frac{1}{\sqrt{\pi(4Dt + 10)}} e^{-\frac{(x-10-ut)^2}{4Dt+10}} \tag{4.15}$$

where u is the advective velocity of flow, and D is the diffusion coefficient of the dissolved chemical. We chose $D = 3.36 \times 10^{-6}$ m^2/s such that $1/s^- = 0.6$, which usually yields a good balance between computational efficiency and numerical stability [18]. The simulation domain was $L = 20$ m long. Periodic boundary condition was applied. The lattice spacing, which is also the characteristic length, is $\Delta l = 0.01$ m. To normalize the

ADE, we selected $u_0 = 0.01$ m/s and $c_0 = 0.178$ kg/m.

Both pure and advective diffusion were studied. Figure 4.2a shows that for pure diffusion the LB models with and without the velocity correction yield nearly the same results, which agree well with the analytical solution. The discrepancy nearby both domain boundaries is caused by the finite simulation domain used in our simulations, because the analytical solution is derived for an infinite domain. However, once advection occurs, the TRT model without the correction yields less spreading than predicted by the analytical solution, while the TRT model with the correction yields almost the exact solution regardless of the effect of boundaries (see Figure 4.2b). The results illustrate that the velocity correction term is able to eliminate the numerical diffusion caused by advection.

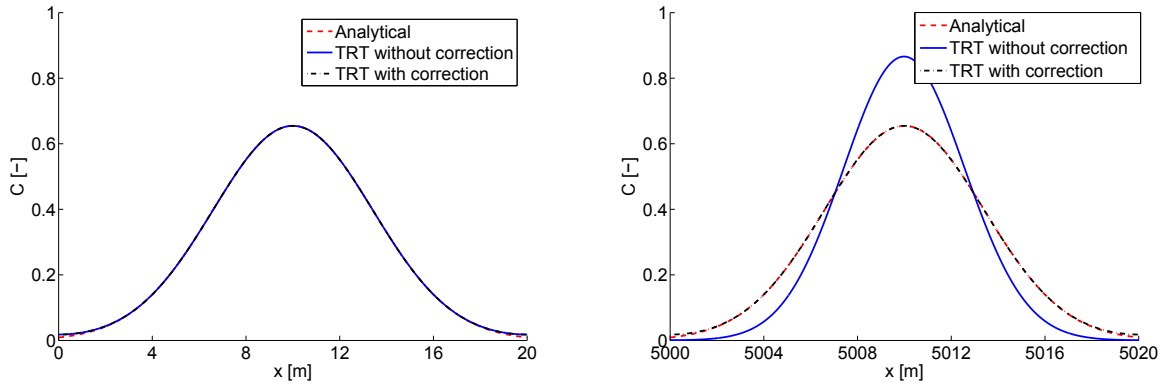

(a) $u = 0$ (b) $u = 0.005$ m/s

Figure 4.2: Comparison of simulation results from the TRT models with and without the velocity correction against analytical solution 277.8 hours after the initial Gaussian concentration distribution was introduced into the simulation domain. (a) Pure diffusion and (b) advective diffusion.

4.4.2 1D transport with initial top hat concentration distribution

The TRT model with the velocity correction has proven to yield good accuracy for transport with an initial Gaussian concentration distribution. Here we examine the stability of the TRT models by studying the concentration evolution with an initial top hat distribution, which is more challenging because of the discontinuity of the initial concentration profile. A numerical method is defined to be stable when the error, as indicated by the oscillation amplitude in this case, does not grow during the simulation [9]. We selected $L = 20$ m, $\Delta l = 0.01$ m, $u_0 = 0.01$ m/s, and $D = 3.36 \times 10^{-6}$ m^2/s. Periodic boundary condition was used. The top hat distribution with initial concentration, $c_0 =$ 1.0 kg/m, is introduced into the region ranging from 8 to 12 m.

When no advection occurs ($u = 0$), the TRT models with and without the correction as well as the SRT model generated almost the same simulation results (results not shown). When the velocity is non-zero, the three models exhibited different stabilities that depend on the magnitude of u. Figure 4.3 shows the simulated concentration distributions for the three models 100 seconds after the initial top hat concentration distribution was introduced into the domain for different advective velocities. When u is small ($u = 0.005$ and 0.006 m/s), only the TRT model without the correction shows obvious oscillations near the region with a high concentration gradient. When $u = 0.008$ or 0.0082 m/s, both the SRT model and the TRT model without the correction generate divergent solutions with dramatic oscillation amplitudes (results not shown). Only the TRT model with the correction is stable, although small oscillations are observed around the region where the

concentration gradient is high. Therefore, the TRT model with the correction has the best numerical stability among the three models.

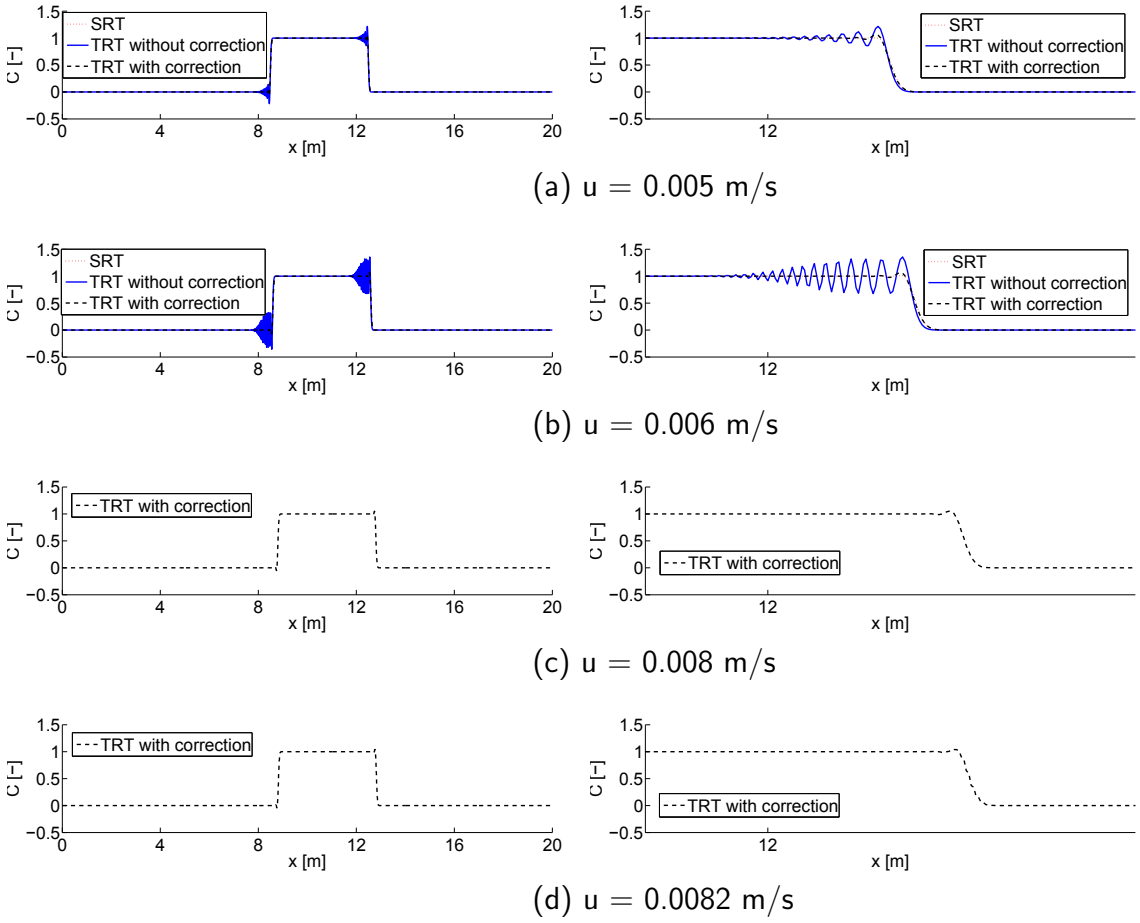

Figure 4.3: Normalized concentration profiles 100 seconds after an initial top hat concentration distribution was introduced into the domain for different advective velocities. Both full distribution (left) and local distribution nearby the frontal region (right) are presented.

Figure 4.4 shows the simulation results for the three models 800 seconds after the initial top hat concentration distribution was introduced into the domain. In contrast to the results shown in Figure 4.3, the TRT model without the correction is found to be stable only when $u = 0.005$ m/s, although oscillations occur in the beginning. When $u = 0.006$ m/s, the oscillations of the TRT model without the correction grow unboundedly

with time. When u = 0.008 m/s, both the SRT model and the TRT model with the correction oscillate in the beginning. However, the SRT model diverges quickly, while the unphysical oscillations in the TRT model with the correction vanish eventually. When u = 0.0082 m/s, the oscillations of the TRT model with the correction increase with time and eventually get out of control. To sum up, the TRT model with the correction exhibits the best stability, while the TRT model without the correction performs the worst.

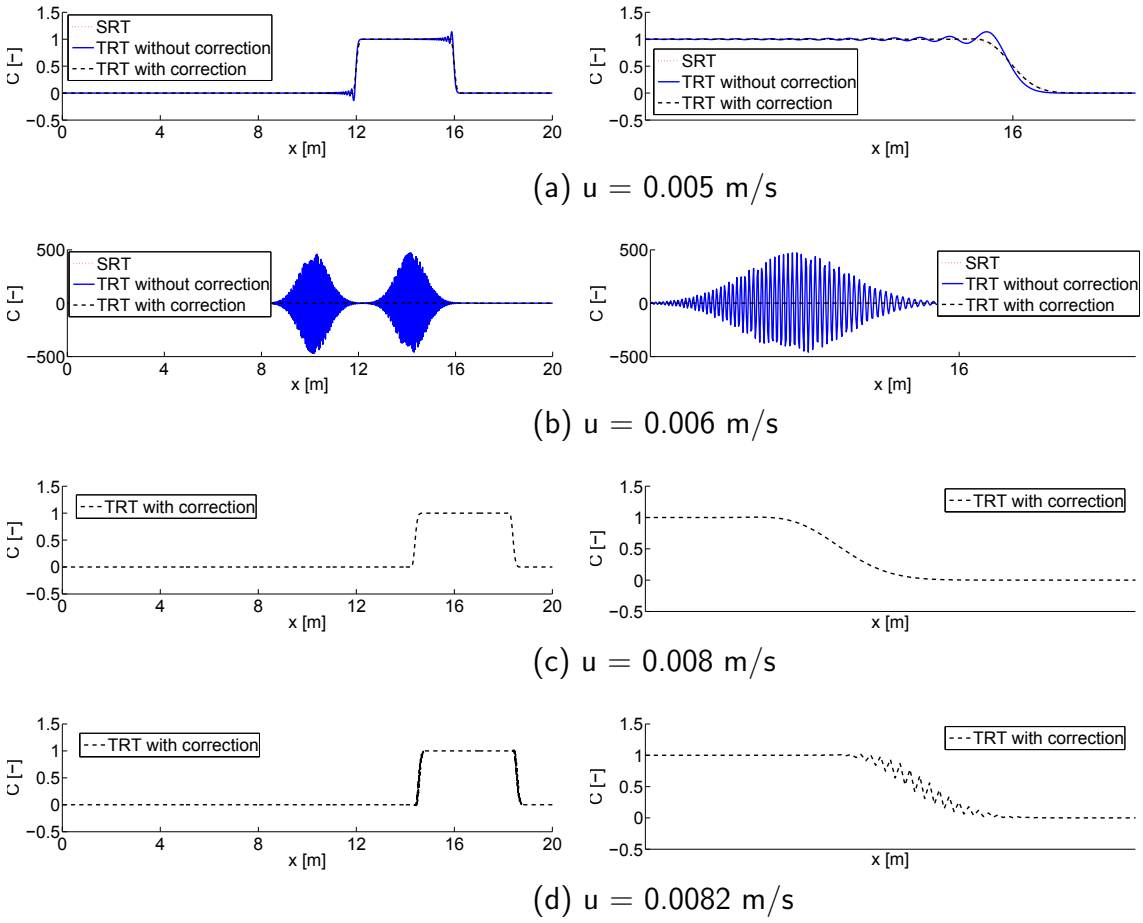

Figure 4.4: Normalized concentration profiles 800 seconds after an initial top hat concentration distribution was introduced into the domain for different advective velocities. Both full distribution (left) and local distribution nearby the frontal region (right) are presented.

In 1D simulations, the D3Q15 model reduces to a 1D model with three discrete

velocities (D1Q3). Ginzburg et al. [16] derived the necessary stability conditions for the D1Q3 TRT model,

$$\begin{aligned} V^2 &\leq c_e \qquad \text{when} \quad g^{(u)} = 0 \\ V^2 &\leq 1 - c_e \quad \text{when} \quad g^{(u)} = 1 \end{aligned} \tag{4.16}$$

where $V = u/u_0$ is the dimensionless advective velocity. Our simulation results are consistent with this criterion. Actually, these necessary stability conditions are also sufficient conditions for the 1D transport with an initial top hat concentration distribution when $\wedge$ $= 1/4$ or $3/16$ [16].

4.4.3 Taylor dispersion

In this section, we investigate 3D Taylor dispersion in a circular tube by using the TRT models with and without the correction as well as the SRT model, and compare the simulation results with an analytical solution. The velocity profile in the tube is given by

$$u(r) = u_{max}(1 - r^2/R^2) \tag{4.17}$$

where u_{max} is the maximum velocity in the tube, R is the radius of the tube, and r is the radial coordinate. Taylor [33] derived the effective longitudinal diffusion coefficient of a chemical, D_e, which is dispersed by the tube flow:

$$D_e = D\left(1 + \frac{\mathrm{Pe}^2}{192}\right) \tag{4.18}$$

where D is the molecular diffusion coefficient of the chemical, $Pe = \overline{u}\ 2R/D$ is the Peclet number, and $\overline{u}$ is the average flow velocity in the tube. We selected $D = 3.2\times 10^{-5}$ mm^2/s, $L = 100$ mm, $R = 0.5$ mm, $\Delta l = 0.1$ mm, and $u_0 = 0.1$ mm/s. Periodic boundary condition was used in the longitudinal direction. A slug of the chemical was initially injected into the region ranging from 20 to 30 mm. The dispersion of the chemical was simulated for different Peclet numbers (see Table 4.1). The velocities calculated by Eq. (4.17) were used as input to the TRT model. In order to compare the simulation results with the analytical solution given by Eq. (4.18), we calculated the first and second moments from the simulated concentration field via

$$\langle \vec{r}(t) \rangle = \frac{\iiint \vec{r} c(x,y,z,t) dxdydz}{\iiint c(x,y,z,t) dxdydz} \tag{4.19}$$

and

$$\langle \sigma^2(t) \rangle = \frac{\iiint (\vec{r} - \langle \vec{r}(t) \rangle)^2 c(x,y,z,t) dxdydz}{\iiint c(x,y,z,t) dxdydz} \tag{4.20}$$

where $\vec{r} = (x, y, z)$. The simulated centers of the mass, $\langle \vec{r}(t) \rangle$, agree well with the analytical solution $(\overline{u}t, 0, 0)$. The variance $\langle \sigma^2(t) \rangle = 2D_e t$ is used to estimate the simulated D_e. However, this linear relation is valid only after the slug of chemical was introduced into the flow for a sufficiently long period of time such that the chemical has enough time for transversal mixing. Then we can calculate the simulated D_e by

$$D_e = \frac{1}{2}\frac{d\langle \sigma^2 \rangle}{dt} = \frac{1}{2}\frac{\langle \sigma_{t_2}^2 \rangle - \langle \sigma_{t_1}^2 \rangle}{t_2 - t_1} \tag{4.21}$$

The results for different Peclet numbers (due to the different flow velocities) are shown in Table 4.1. Although the SRT model shows the best accuracy among the three models, it presents the worst stability. The TRT models with and without the correction yield almost the same effective diffusion coefficient, because the numerical diffusion can be ignored compared to the effective diffusion in these simulations. The TRT model with the velocity correction exhibits the best stability. The maximum velocity in the tube follows the necessary stability conditions for the D3Q15 TRT model [16]:

$$\begin{aligned} V^2 &\leq c_e \quad \text{when} \quad g^{(u)} = 0 \\ V^2 &\leq \tfrac{3}{2} c_e \quad \text{when} \quad g^{(u)} = 1 \end{aligned} \tag{4.22}$$

where $V = u_{max}/u_0$. However, the criterion is not a sufficient condition anymore due to the numerical error caused by the pore boundaries. When refining the grid, we found that the stable simulations were achieved for a larger Peclet number, and the allowable maximum velocity for numerical stability approached the upper limit given by Eq. (4.22). The SRT model is less stable than the TRT model without correction, which is inconsistent with the previous results shown by the transport with initial top hat distribution. A possible explanation is that the relaxation rate $1/s^- = 0.5096$ is very small in this Taylor dispersion scenario, which limits the application of the SRT model to only small velocities due to numerical instability [5].

Table 4.1: Comparison of simulated effective diffusion coefficient D_e (mm^2/s) from the TRT models with and without the velocity correction against the analytical solution and the SRT model simulations for different Peclet numbers (NaN denotes numerically unstable).

Pe	D_e (analytical)	D_e (SRT)	D_e (TRT without correction)	D_e (TRT with correction)
0	3.2×10^{-5}	3.16×10^{-5}	3.023×10^{-5}	3.023×10^{-5}
10	4.867×10^{-5}	4.852×10^{-5}	4.833×10^{-5}	4.833×10^{-5}
100	1.699×10^{-3}	1.723×10^{-3}	1.840×10^{-3}	1.840×10^{-3}
500	4.170×10^{-2}	4.215×10^{-2}	4.527×10^{-2}	4.523×10^{-2}
1000	1.667×10^{-1}	NaN	1.809×10^{-1}	1.803×10^{-1}
1400	3.267×10^{-1}	NaN	NaN	3.527×10^{-1}
1500	3.750×10^{-1}	NaN	NaN	NaN

4.4.4 Bacterial chemotaxis

Certain motile bacteria are able to move in response to gradients in chemical concentration in their surrounding environment, a phenomenon termed chemotaxis [24, 2]. Bacterial chemotaxis can improve bioavailability of contaminants in aqueous environments [23, 21]. We assume that the bacteria can be described like a soluble chemical and that the substrate is the only rate-limiting chemical. Then the transport and fate of the bacteria and the substrate can be described by the following two coupled partial differential equations [19, 21]:

$$\frac{\partial b}{\partial t} + \nabla \cdot [b(\mathbf{u} + \mathbf{u}_c) - \mu \nabla b] = Yq\frac{s}{s + k_s}b - kb \tag{4.23}$$

$$\frac{\partial s}{\partial t} + \nabla \cdot (s\mathbf{u} - D\nabla s) = -q\frac{s}{s + k_s}b \tag{4.24}$$

where b is the bacterial concentration, s is the substrate concentration, $\mathbf{u}$ is the pore-water velocity, μ is the random motility coefficient of the bacteria, D is the diffusion coefficient of the substrate, q is the maximum reaction rate, k_s is the half-saturation coefficient, Y is the yield coefficient, and k is the decay rate. The chemotactic velocity $\mathbf{u}_c$ is assumed to depend on the substrate concentration and its gradient, and it is estimated by the model derived by Rivero et al. [32]:

$$\mathbf{u}_c = \frac{2v_s}{3} \tanh\left(\frac{\chi_0}{2v_s}\frac{K_d}{(K_d+s)^2}|\nabla s|\right)\frac{\nabla s}{|\nabla s|} \tag{4.25}$$

where v_s is the swimming speed of the bacteria, K_d is a dissociation constant, and χ_0 is the chemotactic sensitivity coefficient.

The corresponding dimensionless equations are

$$\frac{\partial B}{\partial T} + \nabla \cdot B(\mathbf{V} + \mathbf{V_c}) = \frac{1}{\mathsf{Pe}_b}\nabla^2 B + \hat{Y}Q\frac{S}{S+K_s}B - KB \tag{4.26}$$

$$\frac{\partial S}{\partial T} + \nabla \cdot S\mathbf{V} = \frac{1}{\mathsf{Pe}_s}\nabla^2 S - Q\frac{S}{S+K_s}B \tag{4.27}$$

where $B = b/b_0$, $S = s/s_0$, $T = tu_0/\Delta l$, $\mathbf{V} = \mathbf{u}/u_0$, $\mathbf{V}_c = \mathbf{u}_c/u_0$, $\hat{Y} = Ys_0/b_0$, $K = k\Delta l/u_0$, $K_s = k_s/s_0$, $Pe_b = \Delta l u_0/\mu$, and $Pe_s = \Delta l u_0/D$.

In the simulations, all parameters characterizing the bacteria and substrate system are from Pedit et al. [30] (see Table 4.2). The TRT models with and without the correction are used to simulate the reactive transport of the bacteria and substrate in a 1D domain

with 100 mm length. We selected $\Delta l = 0.04$ mm and $u_0 = 0.048$ mm/s. Periodic boundary condition was used. At the beginning of the simulations, the substrate was distributed uniformly, and a 10 mm long slug of bacteria was injected into the region ranging from 20 to 30 mm. The initial normalized concentration distribution is shown in Figure 4.5. We examined the reactive transport of the bacteria and substrate for different advective velocities.

Table 4.2: Parameters for the bacteria and substrate system.

Parameter	Symbol	Value
Initial bacterial concentration	b_0	4×10^3 cfu/mm^3
Initial substrate concentration	s_0	2.83×10^{-8} g/mm^3
Random motility coefficient of bacteria	μ	3.2×10^{-5} mm^2/s
Diffusion coefficient of substrate	D	7.5×10^{-4} mm^2/s
Maximum rate of naphthalene consumption	q	7.9×10^{-16} g/cfu/s
Yield coefficient	Y	0
Bacterial decay rate	k	0
Dissociation constant of the substrate/receptor reaction	K_d	2.1×10^{-9} g/mm^3
Half-saturation coefficient	k_s	1.3×10^{-10} g/mm^3
Chemotactic sensitivity coefficient	χ_0	1.8×10^{-3} mm^2/s
Swimming speed	v_s	4.8×10^{-2} mm/s

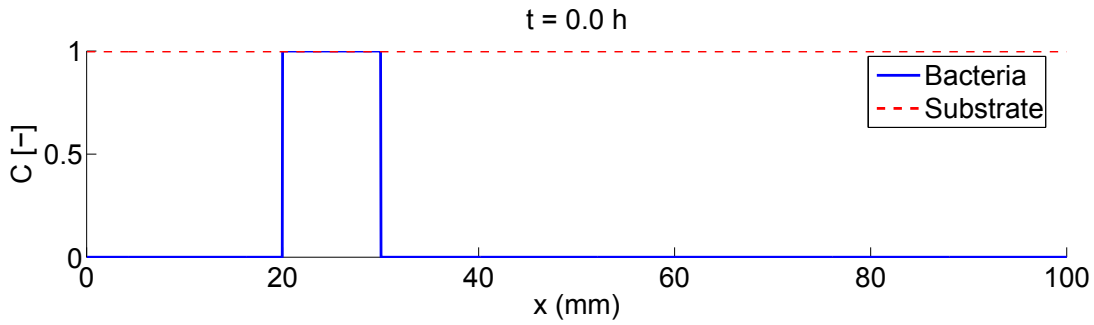

Figure 4.5: Initial normalized concentration profiles of the bacteria and substrate.

For the case where the flow is stagnant, the concentration profiles of the bacteria at different time moments are shown in Figure 4.6. Two bacterial bands form and move

downstream and upstream, respectively. There is no difference between the TRT models with and without the velocity correction. In the case of a small advective velocity, $u = 1.0\times10^{-3}$ mm/s, the TRT models with and without the correction yield almost the same concentration profiles (see Figure 4.7). However, as the velocity further increases, $u = 1.0\times10^{-2}$ mm/s, the bacterial bands from the TRT model without the correction move faster and have a higher peak concentration than predicted by the TRT model with the correction. A comparison between Figures 4.6 and 4.7 shows that the TRT model with the correction yields almost the same shapes of the bacterial concentration profiles for the two velocities. Although there is no analytical solution for this chemotactic transport, the same bacterial shapes can be expected due to a Galilean transformation $x' = x - ut$, via which we can transform the bacterial and substrate concentration profiles for the nonzero advective velocity into the system without advective velocity. Therefore, the bacterial concentration profiles should be the same (except for a time lag) no matter how large the advective velocity is. This means that the TRT model with the velocity correction predicts the bacterial transport best.

4.5 Summary and conclusions

In this study, we have given a detailed description of a TRT-LB method for 3D advective-diffusive-reactive transport. This method is very powerful, because the optional velocity correction term allows for the elimination of numerical diffusion. We also provide a pseudocode for easy implementation of the methods and applied them to vari-

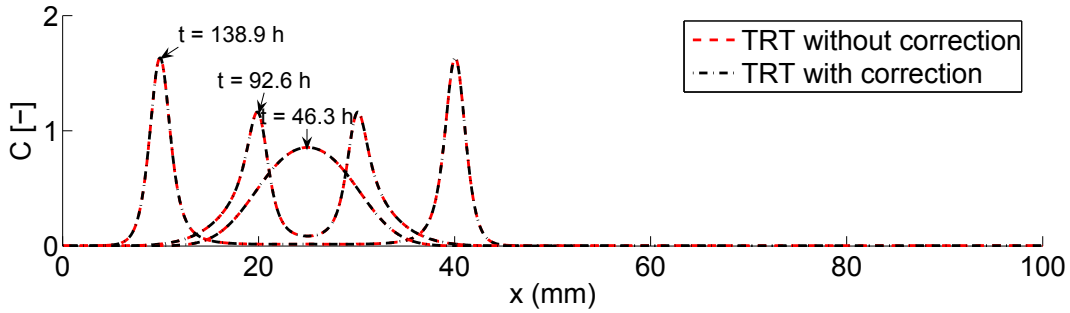

Figure 4.6: Normalized concentration profiles of the bacteria from the TRT models with and without the velocity correction at different time moments. The flow is stagnant, $u = 0$.

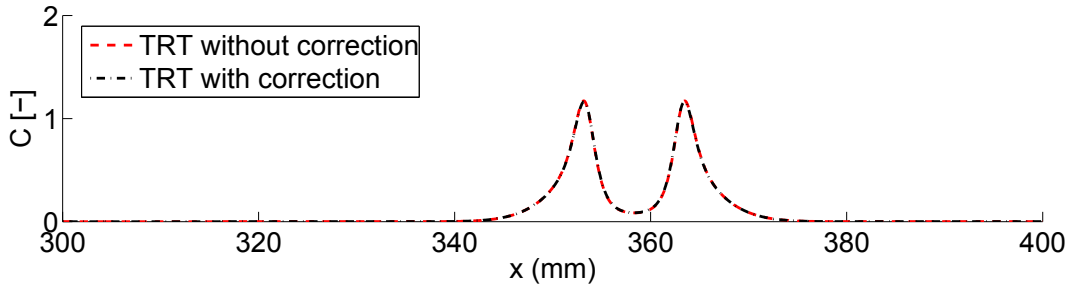

(a) $u = 1.0{\times}10^{-3}$ mm/s

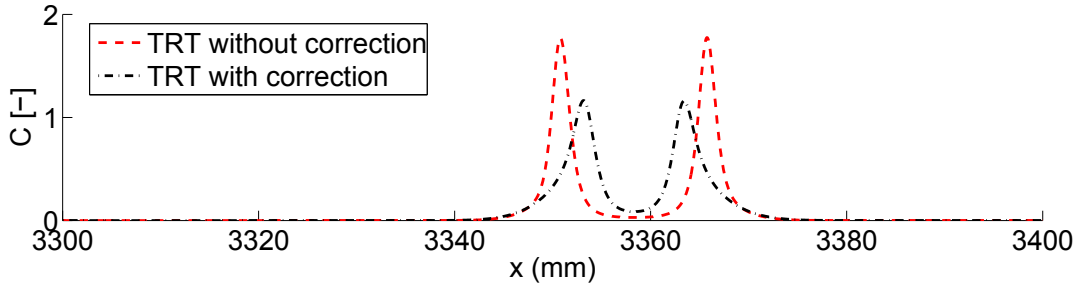

(b) $u = 1.0{\times}10^{-2}$ mm/s

Figure 4.7: Normalized concentration profiles of the bacteria from the TRT models with and without the correction 92.6 hours after the bacterial slug was introduced into the domain for different advective velocities.

ous advective-diffusive-reactive transport phenomena. When advection is not present, the TRT models with and without the velocity correction have almost the same accuracy and stability. When advection occurs, the TRT model without the correction introduces neg-

ative numerical diffusion, which scales quadratically with the advective velocity. However, the TRT model with the correction can eliminate this numerical diffusion and generate a more accurate solution. The TRT model with the correction also demonstrates a better stability than the TRT model without correction when advection occurs. Therefore, it is advisable to include the velocity correction in the TRT model when the advective velocity is high. Finally we have shown that the TRT method with the velocity correction predicts accurately the transport of chemotactic bacteria in case of advective flow assuming that the numerical solution obtained for stagnant flow can be used as a benchmark (when combined with a Galilean transformation).

Bibliography

[1] J.P. Adler. Chemotaxis in bacteria. *Science*, 153:708–716, 1966.

[2] G. Alexandre, S. Greer-Phillips, and I. Zhulin. Ecological role of energy taxis in microorganisms. *FEMS Microbiology Reviews*, 28(1):113–126, feb 2004.

[3] I. Battiato, D.M. Tartakovsky, A.M. Tartakovsky, and T.D. Scheibe. Hybrid models of reactive transport in porous and fractured media. *Advances in Water Resources*, 34:1140–1150, 2011.

[4] M.J. Blunt, B. Bijeljic, H. Dong, O. Gharbi, S. Iglauer, P. Mostaghimi, A. Paluszny, and C. Pentland. Pore-scale imaging and modelling. *Advances in Water Resources*, 51:197–216, January 2013.

[5] S. Chen and G. Doolen. Lattice Boltzmann method for fluid flows. *Annual Review of Fluid Mechanics*, 30:329–364, 1998.

[6] T.P. Clement, Y. Sun, B.S. Hooker, and J.N. Petersen. Modeling Multispecies Reactive Transport in Ground Water. *Ground Water Monitoring and Remediation*, 18(2):79–92, May 1998.

[7] B.H. Devkota and J. Imberger. Lagrangian modeling of advection-diffusion transport

in open channel flow - Devkota - 2009 - Water Resources Research - Wiley Online Library. *Water Resources Research*, 2009.

[8] D. d'Humières, I. Ginzburg, M. Krafczyk, P. Lallemand, and L.S. Luo. Multiple-relaxation-time lattice Boltzmann models in three dimensions. *Philosophical Transactions of The Royal Society of London Series A*, 360(1792):437–451, 2002.

[9] J.H. Ferziger and M. Perić. Computational methods for fluid dynamics. 1999.

[10] I. Ginzburg. Generic boundary conditions for lattice Boltzmann models and their application to advection and anisotropic dispersion equations. *Advances in Water Resources*, 28(11):1196–1216, November 2005.

[11] I. Ginzburg. Equilibrium-type and link-type lattice Boltzmann models for generic advection and anisotropic-dispersion equation. *Advances in Water Resources*, 28 (11):1171–1195, 2005.

[12] I. Ginzburg. Truncation Errors, Exact and Heuristic Stability Analysis of Two-Relaxation-Times Lattice Boltzmann Schemes for Anisotropic Advection-Diffusion Equation. *Communications in Computational Physics*, 11:1439–1502, December 2012.

[13] I. Ginzburg. Multiple anisotropic collisions for advection-diffusion Lattice Boltzmann schemes. *Advances in Water Resources*, 51:381–404, January 2013.

[14] I. Ginzburg and D. D'Humières. Multireflection boundary conditions for lattice Boltzmann models. *Physical Review E*, 68(6):066614, December 2003.

[15] I. Ginzburg and F. Verhaeghe. Two-relaxation-time lattice Boltzmann scheme: About parametrization, velocity, pressure and mixed boundary conditions. *Communications in Computational Physics*, 3(2):427–478, February 2008.

[16] I. Ginzburg, D. d'Humieres, and A. Kuzmin. Optimal stability of advection-diffusion lattice Boltzmann models with two relaxation times for positive/negative equilibrium. *Journal of Statistical Physics*, 139(6):1090–1143, 2010.

[17] X. He, Q. Zou, L Luo, and M. Dembo. Analytic solutions of simple flows and analysis of nonslip boundary conditions for the lattice Boltzmann BGK model. *Journal of Statistical Physics*, 1997.

[18] M. Hilpert. Determination of dimensional flow fields in hydrogeological settings via the MRT lattice-Boltzmann method. *Water Resources Research*, 47(9), September 2011.

[19] M. Hilpert. Lattice-Boltzmann model for bacterial chemotaxis. *Journal of Mathematical Biology*, 51:302–332, 2005.

[20] P. Lavallée, J.P. Boon, and A. Noullez. Boundaries in lattice gas flows. *Physica D: Nonlinear Phenomena*, 47(1-2):233–240, January 1991.

[21] W. Long and M. Hilpert. Lattice-Boltzmann modeling of contaminant degradation

by chemotactic bacteria: Exploring the formation and movement of bacterial bands. *Water Resources Research*, 44:W09415, 2008.

[22] W. Long, H. Huang, J. Serlemitsos, E.B. Liu, A.H. Reed, , and M. Hilpert. A correlation for the collector efficiency of nanoparticles for clean-bed filtration in packings of nonspherical collectors. *Colloids and Surfaces A: Physicochemical and Engineering Aspects*, 358:163–171, 2010.

[23] R.B. Marx and M.D. Aitken. Bacterial chemotaxis enhances naphthalene degradation in a heterogeneous aqueous system. *Environmental Science and Technology*, 34: 3379–3383, 2000.

[24] R.B. Marx and M.D. Aitken. Quantification of chemotaxis to naphthalene by *Pseudomonas putida* G7. *Applied and Environmental Microbiology*, 65:2847–2852, 1999.

[25] P. Meakin and A. Tartakovsky. Modeling and simulation of porescale multiphase fluid flow and reactive transport in fractured and porous media. *Reviews of Geophysics*, July 2009.

[26] R. Moreno-Atanasio, R.A. Williams, and X. Jia. Combining X-ray microtomography with computer simulation for analysis of granular and porous materials. *Particuology*, 8(2):81–99, April 2010.

[27] P.P. Mukherjee, Q. Kang, and C. Wang. Pore-scale modeling of two-phase transport

in polymer electrolyte fuel cells—progress and perspective. *Energy and Environmental Science*, 4(2):346, 2011.

[28] H. Okabe and M.J. Blunt. Prediction of permeability for porous media reconstructed using multiple-point statistics. *Physical Review E, Statistical, Nonlinear, and Soft Matter Physics*, 70(6 Pt 2):066135, December 2004.

[29] C. Pan, L. Luo, and C.T. Miller. An evaluation of lattice Boltzmann schemes for porous medium flow simulation. *Computers and Fluids*, 35(8-9):898–909, 2006.

[30] J.A. Pedit, R.B. Marx, C.T. Miller, and M.D. Aitken. Quantitative analysis of experiments on bacterial chemotaxis to naphthalene. *Biotechnology and Bioengineering*, 78(6):626–634, June 2002.

[31] A. Raoof, H.M. Nick, T.K.T. Wolterbeek, and C.J. Spiers. Pore-scale modeling of reactive transport in wellbore cement under CO2 storage conditions. *International Journal of Greenhouse Gas Control*, 11:S67–S77, November 2012.

[32] M.A. Rivero, R.T. Tranquillo, H.M. Buettner, and D. Lauffenburger. Transport models for chemotactic cell populations based on individual cell behaviour. *Chemical Engineering Science*, 44(12):2881–2897, 1989.

[33] G.I. Taylor. Dispersion of soluble matter in solvent flowing slowly through a tube. *Proceedings of the Royal Society of London Series A*, 219:186–203, 1953.

[34] C.J. Werth, C. Zhang, M.L. Brusseau, M. Oostrom, and T. Baumann. A review

of non-invasive imaging methods and applications in contaminant hydrogeology research. *Journal of Contaminant Hydrology*, 113(1-4):1–24, April 2010.

Chapter 5. Summary, Engineering Application, and Future Work

5.1 Summary

This dissertation studied the effects of bacterial chemotaxis on the formation and migration of traveling bacterial waves as well as on contaminant bioremediation in the presence and absence of bacterial growth and decay. Such waves are capable of enhancing contaminant removal by improving bioavailability of contaminants in the subsurface. Both MRT and TRT LB models were developed to investigate the bacterial chemotaxis and other reactive transport phenomena. A comprehensive mathematical model that accounts for bacterial chemotaxis, growth and decay, and electron acceptor concentration, was applied to study the bacterial movement and contaminant degradation. Various factors that affect the survival and migration of chemotactic bacteria were evaluated. Suggestions that take advantage of chemotaxis in *in situ* bioremediation were proposed.

A MRT LB model was first developed to study the formation and migration of traveling bacterial waves caused by chemotaxis (chemotactic waves). This model focused on chemotaxis regardless of bacterial growth and decay, which is the case of many chemotaxis-related experimental research in laboratories. Different factors that affect the formation,

shape, and propagation of such chemotactic waves were evaluated. Numerical simulations were conducted and led to the following findings: (1) in order to generate a chemotactic wave, a small substrate diffusion coefficient and a sufficiently high initial number of bacteria are required; (2) it is easier for chemotactic bacteria to form a chemotactic wave in a 1D domain than in a 3D one, because the bacteria are diluted and the substrate is replenished more quickly in a 3D geometry; (3) a uniform flow velocity has no impact on the formation and shape of bacterial waves while shear flow tends to eliminate the waves; (4) when the flow velocity is small, chemotactic bacteria might form two waves moving upstream and downstream, respectively. As the velocity increases, such waves were eliminated by strong hydrodynamic dispersion.

A TRT LB model was also introduced to study advective-diffusive-reactive transport. This model is very powerful, because the optional velocity correction term allows for the elimination of numerical diffusion. We provided a pseudocode for easy implementation of the method and applied it to various advective-diffusive-reactive transport phenomena. The numerical simulations led to the following conclusions: (1) when advection is not present, the TRT models with and without the velocity correction exhibited almost the same accuracy and stability. When advection occurs, the TRT model without the correction introduced negative numerical diffusion, which scales quadratically with the advective velocity, while the TRT model with the correction eliminated this numerical diffusion; (2) the TRT model with the correction demonstrated a better numerical stability than the TRT model without the correction when advection occurs. Therefore, it is advisable to

include the velocity correction in the TRT model when the advective velocity is large.

Since bacterial survival is a significant factor for *in situ* bioremediation, the coupled effects of chemotaxis and growth on the formation and propagation of bacterial waves were studied. In an effort to represent arranged conditions for real systems in the subsurface, three bacteria/substrate systems for different electron acceptor concentrations were examined. Findings from numerical simulations include the followings: (1) even when the electron acceptor concentrations are excessive, not all systems can utilize chemotaxis to improve contaminant remediation; (2) bacteria can form a growth/decay/motility wave due to the balance between bacterial growth, decay and random motility, even if no chemotaxis occurs. A conceptual model was developed to estimate the speed of this growth/decay/motility wave. Results showed that this wave speed scales with the square root of the bacterial yield coefficient, the random motility coefficient, and the maximum reaction rate of the substrate. Bacterial decay decreased this wave speed, but this decrease is minor when the decay rate is relatively small compared to the growth rate; (3) the effect of chemotaxis on bacterial propagation depends on the strength of chemotaxis. If the chemotaxis is too weak to form a wave or the speed of the chemotactic wave is less than half of the speed of the growth/decay/motility wave, chemotaxis hardly improves bacterial propagation. However, once the former speed exceeds the latter one, chemotaxis substantially enhances the bacterial propagation.

5.2 Engineering Application

Although a large number of experiments have shown that bacterial chemotaxis can improve contaminant remediation [3, 10, 4, 5], no obvious evidence has been reported at contaminated sites that chemotaxis improves bioremediation [1]. Our study provides possible explanations for this discrepancy. First, not all bacteria and substrate systems that perform chemotaxis are able to improve contaminant degradation. The chemotaxis hardly accelerates the removal of pollutants unless the speed of the chemotactic wave is larger than half of the speed of the growth/decay/motility wave. Bacterial chemotaxis toward contaminants at many contaminated sites may never reach such a chemotactic strength. Second, in order to form a fast moving chemotactic wave, the total amount of chemotactic bacteria has to be large and the elector acceptor concentration should be high enough for bacteria to consume all chemoattractants. However, the environment for bacterial survival in the field is complicated and the electron acceptors are usually limited. Lastly, a large chemotactic wave speed also requires that the substrate diffusion and the Darcy velocity are small. It may be difficult for a contaminated site to satisfy all of these conditions, each of which is required for forming a fast-moving chemotactic wave. This may explain why chemotaxis is rarely found to enhance contaminant remediation in field observations.

In order to improve pollutant removal through chemotaxis at contaminated sites, we need to create a favorable subsurface environment for this process. For example, chemotaxis enhancement should focus on sites with contaminants that have a small diffusion

coefficient and generate a large gradient of contaminant concentration such that the bacteria perform a strong chemotactic response. If the wild bacterial strains in the field have no or weak chemotaxis, augmented bacteria endowing strong chemotaxis should be injected. Additional electron acceptors must be pumped into the system if they are not present in sufficiently high concentration for bacteria consuming the contaminants. Also, because strong hydrodynamic dispersion decreases the retention time of bacteria and weakens chemotaxis, it is necessary to block the flow in the contaminated area if the Darcy velocity is large. To sum up, although bacterial chemotaxis may offer a valuable approach to enhance contaminant remediation under some circumstances, we may often need to change the natural conditions in the subsurface to take advantage of this mechanism.

This study used the saturated solubility of naphthalene in water under room temperature as the initial concentration [8]. Consequently, pure oxygen needed to be added to the aqueous solution to ensure that chemotaxis can enhance bacterial movement. This operation may be unpractical in engineering applications due to the high cost. Actually, concentrations of naphthalene at contaminated sites are usually below this saturated value. The on-site oxygen concentration sometimes can be expected to be sufficiently high such that bacteria can consume all substrate; then chemotaxis can enhance contaminant removal without injecting additional oxygen. However, if the concentration of substrate is too low, chemotaxis is unable to enhance bacterial migration, even though the electron acceptor is in excess, since the chemotactic intensity is reduced as the substrate

concentration decreases. For example, our simulations showed that chemotaxis did not enhance bacterial movement when the initial naphthalene concentration was reduced to 2.83 mg/mL, no mater how large the initial oxygen concentration was. Therefore, the concentration of contaminant is a crucial factor determining if chemotaxis can be used to enhance contaminant removal at field sites.

5.3 Future Work

In this work, we used simple bacteria and substrate systems compared to the real subsurface systems. For example, we neglected the effects of many environmental factors, such as pH value, temperature, toxicity of contaminants, and competition of different bacterial strains. These factors are significant for bacterial survival and growth [6, 11, 6]. Additionally, we did not consider the adsorption and desorption of bacteria on soil surface, through which chemotactic bacteria may form biofilms. These biofilms are widely observed in the subsurface environment and make it difficult to generate a traveling wave with suspended bacterial populations [2, 9]. Therefore, these factors are in need of investigation in future modeling studies.

The study of bacterial chemotaxis is usually separated from bacterial survival in laboratory experiments such that one can focus on chemotaxis [8]. However, our simulation results showed that chemotaxis and growth affect each other and their coupled effects can significantly enhance bacterial movement. Therefore, it is necessary to study bacterial chemotaxis along with growth and decay in future laboratory experiments to evaluate the

effect of chemotaxis on contaminant removal.

Until now only a few contaminated sites reported that chemotaxis enhanced the bacterial migration [12], while most field work did not find the bioremediation enhancement with the mechanism of chemotaxis [7]. Our modeling findings provide possible explanations for these observations. Additionally, operable measurements to create favorable subsurface environments for bacterial chemotactic responses are proposed, and these approaches are in need of evaluation. Therefore, more field observations are required if we seek to better apply bacterial chemotaxis to *in situ* bioremediation.

Bibliography

[1] R.M. Ford and R.W. Harvey. Role of chemotaxis in the transport of bacteria through saturated porous media. *Advances in Water Resources*, 30(6-7):1608–1617, June 2007.

[2] T.R. Ginn, B.D. Wood, K.E. Nelson, T.D. Scheibe, E.M. Murphy, and T.P. Clement. Processes in microbial transport in the natural subsurface. *Advances in Water Resources*, 25:1017–1042, 2002.

[3] A.C. Grimm and C.S. Harwood. Chemotaxis of $Pseudomonas$ spp.to the polyaromatic hydrocarbon naphthalene. *Applied and Environmental Microbiology*, 63(10): 4111–4115, 1997.

[4] A.C. Hawkins and C.S. Harwood. Chemotaxis of Ralstonia eutropha JMP134 (pJP4) to the herbicide 2, 4-dichlorophenoxyacetate. *Applied and Environmental Microbiology*, 68(2):968–972, February 2002.

[5] R.B. Marx and M.D. Aitken. Bacterial chemotaxis enhances naphthalene degradation in a heterogeneous aqueous system. *Environmental Science and Technology*, 34: 3379–3383, 2000.

[6] N. Nirmalakhandan, S. Xu, C. Trevizo, R. Brennan, and J. Peace. Additivity in microbial toxicity of nonuniform mixtures of organic chemicals. *Ecotoxicology and Environmental Safety*, 37(1):97–102, June 1997.

[7] C.J. O'Lenick, P.R. Bienkowski, P.D. Frymier, and R.N. Weinstein. Effect of Bacterial Chemotaxis on Biodegradation in a Porous Medium. *Bioremediation Journal*, 12(3): 131–144, August 2008.

[8] J.A. Pedit, R.B. Marx, C.T. Miller, and M.D. Aitken. Quantitative analysis of experiments on bacterial chemotaxis to naphthalene. *Biotechnology and Bioengineering*, 78(6):626–634, June 2002.

[9] J.A. Redman, S.L. Walker, and M. Elimelech. Bacterial adhesion and transport in porous media: Role of the secondary energy minimum. *Environmental Science and Technology*, 38:1777–1785, 2004.

[10] S.K. Samanta, B. Bhushan, and A. Chauhan. Chemotaxis of a Ralstonia sp.SJ98 toward different nitroaromatic compounds and their degradation. *Biochemical and Biophysical Research Communications*, 269(1):117–123, May 2000.

[11] S. Tso and G. Taghon. Factors Affecting Predation by Cyclidium sp. and Euplotes sp.on PAH-Degrading and Nondegrading Bacteria. *Microbial Ecology*, 37(1):3–12, January 1999.

[12] M. Wang, R.M. Ford, and R.W. Harvey. Coupled effect of chemotaxis and growth

on microbial distributions in organic-amended aquifer sediments: observations from laboratory and field studies. *Environmental Science and Technology*, 42(10):3556–3562, May 2008.

Chapter 6. Vita

Education

- 2010-present PhD in Geography and Environmental Engineering, *Johns Hopkins University*, Baltimore, MD
- 2007-2010 MS in Hydraulic Engineering, *Tsinghua University*, Beijing, China
- 2003-2007 BS in Hydraulic Engineering, *Wuhan University*, Wuhan, China

Research Experience

- Research assistant (2010-present) Department of Geography and Environmental Engineering, *Johns Hopkins University*, Baltimore, MD
- Research assistant (2007-2010) Department of Hydraulic Engineering, *Tsinghua University*, Beijing, China

Honors and Awards

- Departmental Fellowship, Department of Geography and Environmental Engineering, *Johns Hopkins University*, September 2010
- Lee and Albert H. Halff Doctoral Student Award, *Johns Hopkins University*, September 2010

- Nanhang Scholarship (MS), *Tsinghua University*, 2008
- Third-class scholarship for all-around excellence (BS), *Wuhan University*, 2005
- Second-class scholarship for all-around excellence (BS),*Wuhan University*, 2004

Publications

- **Yan Z.** and M. Hilpert. A Multiple-relaxation-time Lattice-Boltzmann Model for Bacterial Chemotaxis: Effects of Initial Concentration, Diffusion, and Hydrodynamic Dispersion on Traveling Bacterial Bands. *Bulletin of Mathematical Biology*, 76(10):2449-75, 2014
- **Yan Z.**, E.J. Bouwer and M. Hilpert. Coupled Effects of Chemotaxis and Growth on Traveling Bacterial Waves. *Journal of Contaminant Hydrology*. 164:138-152, 2014
- Li L., **Z. Yan** and Z. Liu. Numerical Model for Shallow Wake behind Cylinder. *Applied Mechanics and Materials*. 212-213:1205-1212, 2012
- Li L., C. Qin, Q. Peng, **Z. Yan** and Q. Gao. Numerical Simulation on Dissolved Oxygen Supersaturation Flow over Spillway of the Three Gorges Reservoir. *Journal of Tsinghua University (Science and Technology)*. 15:574-579, 2010
- Li L., **Z. Yan**, W. Wang and Z. Zhu. Application of Experimental Research of Drag Reduction in Hydraulics Experiment Teaching (Chinese). *Experimental Technology and Management*. 27:32-34, 2008

- **Yan Z.**, I. Ginzburg and M. Hilpert. A Pedestrians Guide to a Numerical-Diffusion-FREE Two-relaxation-time Lattice Boltzmann Model for Brownian Particle and Chemotactic Transport (To be submitted).

- Hilpert M., **Z. Yan**, E.F. Pazmino and W.P. Johnson. Dual Network Model for Colloid Filtration under Environmental Conditions (To be submitted).

Presentations

- **Yan Z.** and M. Hilpert: Traveling Waves of Chemotactic Bacteria in the Presence of Growth and Decay. School of Environment, *Nanjing University*, Nanjing, China. February 16-17, 2014.

- **Yan Z.**, E.J. Bouwer and M. Hilpert: Enhancement of Contaminant Biodegradation through Traveling Bacterial Waves. *American Geophysical Union Fall Meeting*, San Francisco, CA. December 8-12, 2013.

- Hilpert M., **Z. Yan**, E.F. Pazmino and W.P. Johnson: Dual network Model for Colloid Filtration under Environmental Conditions". *American Geophysical Union Fall Meeting*, San Francisco, CA. December 8-12, 2013.

- **Yan Z.**, E.J. Bouwer, M. Hilpert and I. Ginzburg: Lattice Boltzmann Modeling of Bacterial Chemotaxis in Porous Media (poster). *American Geophysical Union Fall Meeting*, San Francisco, CA. December 3-7, 2012.

- Hilpert M., **Z. Yan** and W. Long: Lattice-Boltzmann Modeling of Pore-scale Flow

and Transport Processes in Porous Media" (Invited). Workshop "Pore-scale Modeling" at the *Pacific Northwest National Laboratory*, Richland, WA. August 9-10, 2011.